UNIVERSITY OF CALIFORNIA SAN DIEGO

Electrode and electrolyte engineering for high energy density Li metal batteries

A Dissertation submitted in partial satisfaction of the requirements
for the degree Doctor of Philosophy

in

Chemical Engineering

by

Zhaohui Wu

Committee in charge:

Professor Ping Liu, Chair
Professor Shengqiang Cai
Professor Renkun Chen
Professor Zheng Chen
Professor Kesong Yang

2022

The Dissertation of Zhaohui Wu is approved, and it is acceptable in quality and form for publication on microfilm and electronically.

University of California San Diego

2022

DEDICATION

To my parents, Gendang Wu and Xiaoling Huang

EPIGRAPH

“Why is there something rather than nothing?”
-Gottfried Wilhelm Leibniz

TABLE OF CONTENTS

LIST OF FIGURES

LIST OF TABLES

ACKNOWLEDGEMENTS

First of all, I would like to thank my PhD advisor, Dr. Ping Liu. His advises and scientific insights are invaluable in guiding my study and shaping my research methodology. Without his continuous support and patience, this thesis would have never been accomplished.

I would also like to express my gratitude to my committee, including Dr. Zheng Chen, Dr. Renkun Chen, Dr. Kesong Yang, Dr. Shengqiang Cai. Their insightful suggestion and critiques improved the quality of this thesis.

I would like to acknowledge my collaborators at UC San Diego: Dr. Haodong Liu, Dr. Byoung-Sun Lee, Dr. Xing Xing, Dr. Matthew Gonzalez, Dr. Hongyao Zhou, Dr. Shen Wang, Dr. Xiujun Yue, Dr. Jianbin Zhou, Mr. Sicen Yu, Mr. John Holoubek for all their help and discussion on experiments. I am also grateful to all the lab members and group alumnus at Electrochemical Material Science Laboratory.

Additionally, I would like to thank my external collaborators and co-authors: Mr. Zhuo Li and Dr. Peter Khalifah from State University of New York at Stony Brook; Dr. Seong-Min Bak, Dr. Zulipiya Shadike, Dr. Enyuan Hu, Dr. Yonghua Du, Dr. Xiao-Qing Yang from Brookhaven National Laboratory; Dr. Chunyang Wang and Dr. Huolin Xin from University of California, Irvine.

I would like to acknowledge the financial support from Office of Vehicle Technologies of the U.S. Department of Energy through the Advanced Battery Materials Research (BMR) Program (Battery500 Consortium) under Contract DE-EE0007764.

I would also like to thank myself for deciding to pursue my PhD at University of California, San Diego. It was a wonderful journey I would never regret.

Last but not least, I would like to thank my parents for their continuous support and everlasting love. They are always my backbone when facing difficulties.

Chapter 2, in full is currently being prepared for submission for publication of the material, **Zhaohui Wu**, Zhuo Li, Haodong Liu, Peter Khalifah, Ping Liu. The dissertation author was the primary researcher and author of this material.

Chapter 3, in full, is a reprint of the material as it appears in ACS Applied Materials & Interfaces, **Zhaohui Wu**, Seong-Min Bak, Zulipiya Shadike, Sicen Yu, Enyuan Hu, Xing Xing, Yonghua Du, Xiao-Qing Yang, Haodong Liu, Ping Liu. The dissertation author was the primary investigator and author of this paper.

Chapter 4, in full, is a reprint of the material as it appears in Journal of the Electrochemical Society, **Zhaohui Wu**, Haodong Liu, Sicen Yu, Ping Liu. The dissertation author was the primary investigator and author of this paper.

Chapter 5, in full, is currently being prepared for submission for publication of the material, **Zhaohui Wu,** Chunyang Wang, Haodong Liu, Shen Wang, Sicen Yu, Xing Xing, John Holoubek, Huolin Xin, Ping Liu. The dissertation author was the primary researcher and author of this paper.

VITA

2016 Bachelor of Engineering in Chemical Engineering, Beijing University of Chemical Technology

2022 Doctor of Philosophy in Chemical Engineering, University of California San Diego

PUBLICATIONS

1. Holoubek, John, Qizhang Yan, Haodong Liu, Emma J. Hopkins, **Zhaohui Wu**, Sicen Yu, Jian Luo, Tod A. Pascal, Zheng Chen, and Ping Liu. "Oxidative Stabilization of Dilute Ether Electrolytes via Anion Modification." ACS Energy Letters 7 (2022): 675-682.
2. Yu, Sicen, **Zhaohui Wu**, John Holoubek, Haodong Liu, Emma Hopkins, Yuxuan Xiao, Xing Xing, Myeong Hwan Lee, and Ping Liu. "A Fiber‐Based 3D Lithium Host for Lean Electrolyte Lithium Metal Batteries." Advanced Science (2021): 2104829.
3. **Wu, Zhaohui**, Haodong Liu, Sicen Yu, and Ping Liu. "Communication—Binder Effects on Cycling Performance of High Areal Capacity SPAN Electrodes." Journal of The Electrochemical Society (2021).
4. Gonzalez, Matthew S., **Zhaohui Wu**, John Holoubek, Qizhang Yan, Haodong Liu, and Ping Liu. "Mitigating internal shorting to enhance battery safety with gradient-conductivity cathodes." Journal of Power Sources 511 (2021): 230412.
5. Holoubek, John, Qizhang Yan, Haodong Liu, **Zhaohui Wu**, Xing Xing, Hongyao Zhou, Jian Luo, Zheng Chen, and Ping Liu. "Low-Cost Li|| SPAN Batteries Enabled by

Sustained Additive Release." ACS Applied Energy Materials 4, no. 7 (2021): 6422-6429.

6. **Wu, Zhaohui**, Seong-Min Bak, Zulipiya Shadike, Sicen Yu, Enyuan Hu, Xing Xing, Yonghua Du, Xiao-Qing Yang, Haodong Liu, and Ping Liu. "Understanding the Roles of the Electrode/Electrolyte Interface for Enabling Stable Li // Sulfurized Polyacrylonitrile Batteries." ACS Applied Materials & Interfaces 13, no. 27 (2021): 31733-31740.
7. Gonzalez, Matthew S., Qizhang Yan, John Holoubek, Mingqian Li, **Zhaohui Wu**, Hongyao Zhou, Sean Kim et al. "Reversible Switching of Battery Internal Resistance Using Iongate Separators." Advanced Functional Materials (2021): 2102198.
8. Xing, Xing, Yejing Li, Shen Wang, Haodong Liu, **Zhaohui Wu**, Sicen Yu, John Holoubek, Hongyao Zhou, and Ping Liu. "Graphite-Based Lithium-Free 3D Hybrid Anodes for High Energy Density All-Solid-State Batteries." ACS Energy Letters 6, no. 5 (2021): 1831-1838.
9. Holoubek, John, Haodong Liu, **Zhaohui Wu**, Yijie Yin, Xing Xing, Guorui Cai, Sicen Yu et al. "Tailoring electrolyte solvation for Li metal batteries cycled at ultra-low temperature." Nature Energy 6, no. 3 (2021): 303-313.
10. Liu, Haodong, John Holoubek, Hongyao Zhou, **Zhaohui Wu**, Xing Xing, Sicen Yu, Gabriel M. Veith et al. "An anode-free Li metal cell with replenishable Li designed for long cycle life." Energy Storage Materials 36 (2021): 251-256.
11. Liu, Haodong, John Holoubek, Hongyao Zhou, Amanda Chen, Naijen Chang, **Zhaohui Wu**, Sicen Yu et al. "Ultrahigh coulombic efficiency electrolyte enables Li|| SPAN batteries with superior cycling performance." Materials Today 42 (2021): 17-28.

12. Li, Zhuo, Liang Yin, Gerard S. Mattei, Monty R. Cosby, Byoung-Sun Lee, **Zhaohui Wu**, Seong-Min Bak et al. "Synchrotron Operando Depth Profiling Studies of State-of-Charge Gradients in Thick Li (Ni0. 8Mn0. 1Co0. 1) O2 Cathode Films." Chemistry of Materials 32, no. 15 (2020): 6358-6364.
13. Holoubek, John, Mingyu Yu, Sicen Yu, Minqian Li, **Zhaohui Wu**, Dawei Xia, Pranjal Bhaladhare et al. "An all-fluorinated ester electrolyte for stable high-voltage Li metal batteries capable of ultra-low-temperature operation." ACS Energy Letters 5, no. 5 (2020): 1438-1447.
14. Gonzalez, Matthew S., Qizhang Yan, John Holoubek, **Zhaohui Wu**, Hongyao Zhou, Nicholas Patterson, Victoria Petrova, Haodong Liu, and Ping Liu. "Draining Over Blocking: Nano‐Composite Janus Separators for Mitigating Internal Shorting of Lithium Batteries." Advanced Materials 32, no. 12 (2020): 1906836.
15. Lee, Byoung-Sun, **Zhaohui Wu**, Victoria Petrova, Xing Xing, Hee-Dae Lim, Haodong Liu, and Ping Liu. "Analysis of rate-limiting factors in thick electrodes for electric vehicle applications." Journal of the Electrochemical Society 165, no. 3 (2018): A525.

ABSTRACT OF THE DISSERTATION

Electrode and electrolyte engineering for high energy density Li metal batteries

by

Zhaohui Wu

Doctor of Philosophy in Chemical Engineering

University of California San Diego, 2022

Professor Ping Liu, Chair

The rechargeable Li ion batteries are approaching their energy density limitation, while the prosperous growth of electric vehicle market is demanding cheaper and more sustainable batteries with higher energy density.

To meet this goal, new battery material is needed to replace the current battery cathode, namely the $LiCoO_2$ and $LiNi_xMn_yCo_{1-x-y}O_2$ (NMC), which both contains the increasingly expensive transition metal, cobalt.

One way to limit the cobalt usage is to increase the nickel substitution, as Ni is cheaper and more abundant compared to Co. Additionally, high Ni NMC delivers more capacity than their low Ni counterparts. However, transition metal substituent introduced an unexpected problem, i.e., the 1st cycle capacity loss. With electrochemical characterization and synchrotron

X-ray diffraction, we have identified the sluggish Li intercalation at the end of discharge is the root-cause of this problem, which provided guidance for future improvement on these materials.

In addition to optimizing the NMC cathode material, designing new cathode chemistry is another promising approach. Sulfur is a good cathode candidate for next generation energy storage system, due to its high capacity (~1675 mAh cm^{-2}, 8 times as high as NMC), low price, and abundance in earth's crust. However, elemental sulfur cathode suffers from its insulating nature and polysulfide dissolution problem. Sulfurized polyacrylonitrile (SPAN) is a sulfur based conductive polymer, which prevents sulfur dissolution by forming covalent bonding with sulfur and provides electron pathway by the chemical backbone. Although SPAN typically shows extraordinary stable cycling performance due to its unique structure and high specific capacity (~700 mAh cm^{-2}), the Li-SPAN batteries reported in literature are yet to satisfy the industry demand due to its low areal capacity and incompatibility with ether electrolyte, which is commonly used in Li metal batteries. We discovered that $LiNO_3$ as an electrolyte additive, enables SPAN to stably cycle in ether electrolyte, by forming a LiF-rich CEI layer. Its reaction mechanism in different electrolytes was investigated by X-ray absorption spectroscopy, where Li_2S_x dissolution was observed in ether electrolyte without additive. Besides the electrolyte optimization, we replaced the traditionally used PVdF binder with mechanically robust CMC binder, which prevents the mechanical disintegration of the high areal loading cathode (> 6 mAh cm^{-2}) and enables its stable cycling with reduced porosity (30%).

When it comes to the anode, Li metal is the ultimate choice of rechargeable battery anode material due to its highest gravimetric capacity (3862 mAh cm^{-2}) and lowest electrochemical potential (-3.04 V vs SHE.). However, the irregular morphology of electrochemically deposited Li leads to lots of problems, such as parasitic reactions,

electrochemically isolated “dead” Li formation, and dendrite shorting. Many approaches have been developed to suppress the dendritic lithium formation and increase the lithium metal stripping/plating efficiency to > 99.0%. However, the porosity of lithium anode increases upon long cycling is a real challenge, which causes electrolyte depletion, increases cell impedance, and ultimately dictates the end of cell life. We demonstrated a bottom-up approach that an Fe/LiF nanocomposite substrate promotes the nucleation and growth of hexagonal single crystal Li at the initial stage of Li deposition, inducing dense Li deposition on top of the nuclei. Leveraging the low porosity Li, we have shown >1000 (Coulombic efficiency (CE) = 99.17%) and >600 (CE=99.06%) cycle in half cells under exceptionally high current density, 3 and 5 mA cm^{-2}. Further, the full cell tests using NMC811 cathode with practical areal capacity of > 3 mAh cm^{-2}, 1-fold excess of Li, lean electrolyte (3 g Ah^{-1}), and cycled at high current density of 3 mA cm^{-2} retains > 80% cell capacity for more than 130 cycles, which is a 550% improvement over the baseline cells.

We believe that through proper design and optimization of cathode and anode materials, the commercialization route for rechargeable Li metal battery with high energy density will be realized in the coming years.

CHAPTER 1 INTRODUCTION: HIGH ENERGY DENSITY LI|| NMC AND LI||SULFUR BATTERY

1.1 High energy density Li metal batteries for electric vehicles

To limit the rising global temperature and other climate change related problems, many countries have devoted to realizing decarbonization. Electric vehicles are viewed as one of the main decarbonatization pathway. As a result, the market for electric vehicles has been growing fast in the past and is projected to keep growing in the foreseeable future. (Figure 1.1)

The great trend of electrification in the last decade demands for Li batteries with higher energy density. The current Li-ion batteries (LIB) are gradually approaching its limitation. When the Li-ion battery was first commercialized by Sony, its energy density was only 90 Wh/kg.[1] Although the specific energy density was steadily increasing during the past 30 years, reaching 250-300 Wh/kg at cell level, it is still not enough for the electric vehicle application. One of the major drawbacks of battery powered electric vehicle (BEV) is the shorter driving range compared to gasoline cars, which is highly related to the energy density of battery packs.

In addition to the need for higher energy density batteries, cost is another aspect attracting great attention. Currently, the commercial LIB costs ~ 130 $/kWh.[2] However, global EV sales exceeding 15% will require battery cost to fall below 100 $/kWh.[3] To achieve this goal, the currently widely used graphite||NMC battery must be improved, since the primary component of the cathode, Cobalt and Nickel, are getting increasingly expensive due to the high demand and short supply. Additionally, the total reserve of these two transition metals is far less compared to other abundant elements, such as Fe and S. Besides switching to new chemistry, boosting the

energy density of batteries will also reduce the cost per kWh, aiding in achieving < 100 $/kWh goal.

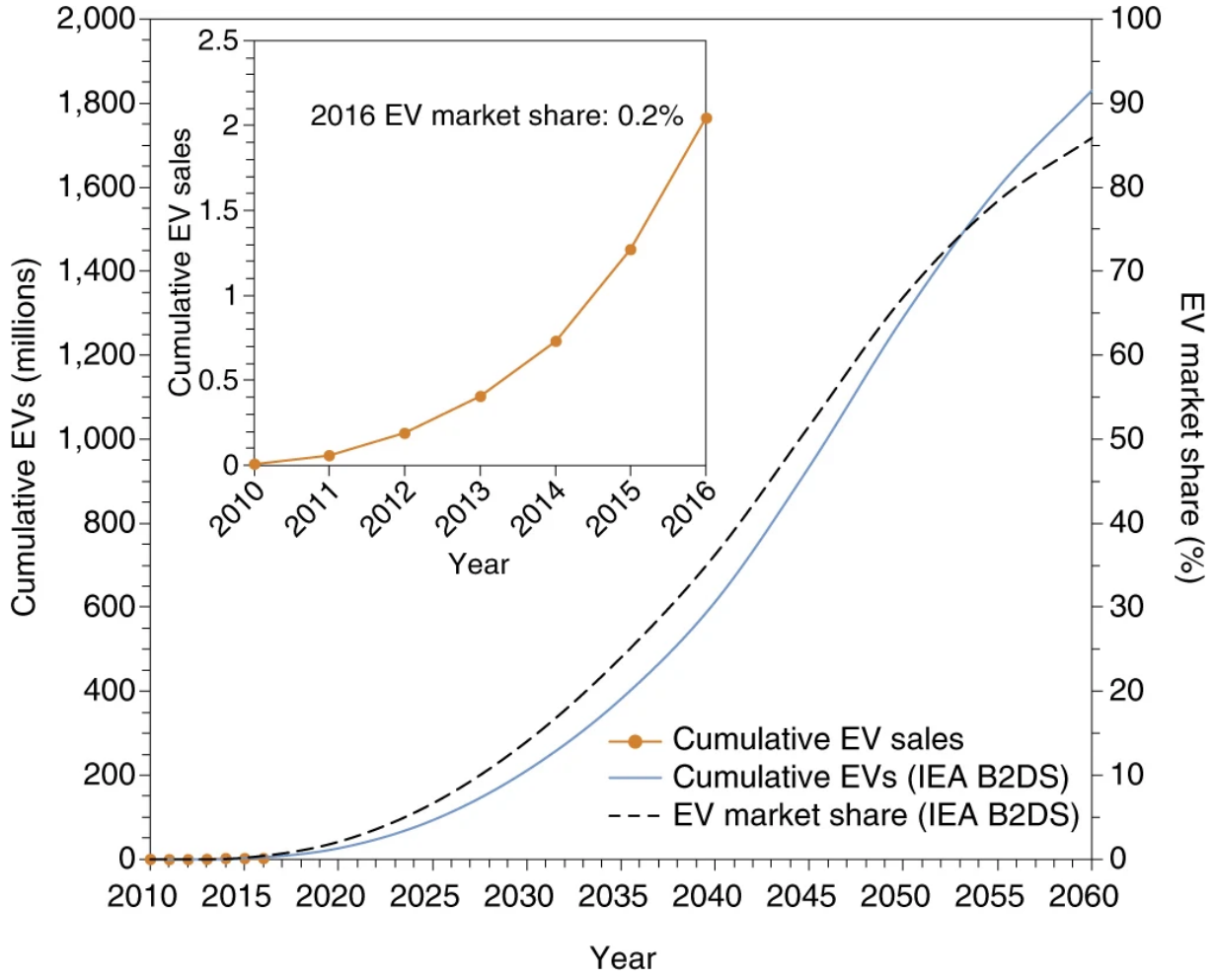

Figure 1.1 Evolution of cumulative EV sales and EV market prescribed in the IEA's 'beyond 2 Degree Scenario'. Inset is the cumulative EV sales up to 2016.[4]

A conventional LIB, as illustrated in Figure 1.2, is comprised of graphite as the anode, separator, $LiCoO_2$ (Alternatively, $LiMO_2$ (M: transition metal), $LiFePO_4$) as the cathode, and liquid electrolyte. To boost the cell level energy density, developing cathode and anode material with higher capacity is a promising approach.

For the anode part, Li metal is an ideal choice to replace graphite. It is regarded as the holy grail of the rechargeable battery anodes, due to its high theoretical specific capacity (3862 mAh g^{-}

[1], 2062 Ah L^{-1}) and lowest electrochemical potential (-3.04 V versus standard hydrogen electrode). Actually, when Li battery was first invented, it was using Li metal as the anode. Later, researchers switched to graphite due to safety concerns caused by Li dendrite growth. Recently, due to the high energy density nature of metallic Li anode and progress in advanced electrolytes, Li metal battery (LMB) is getting popular again.

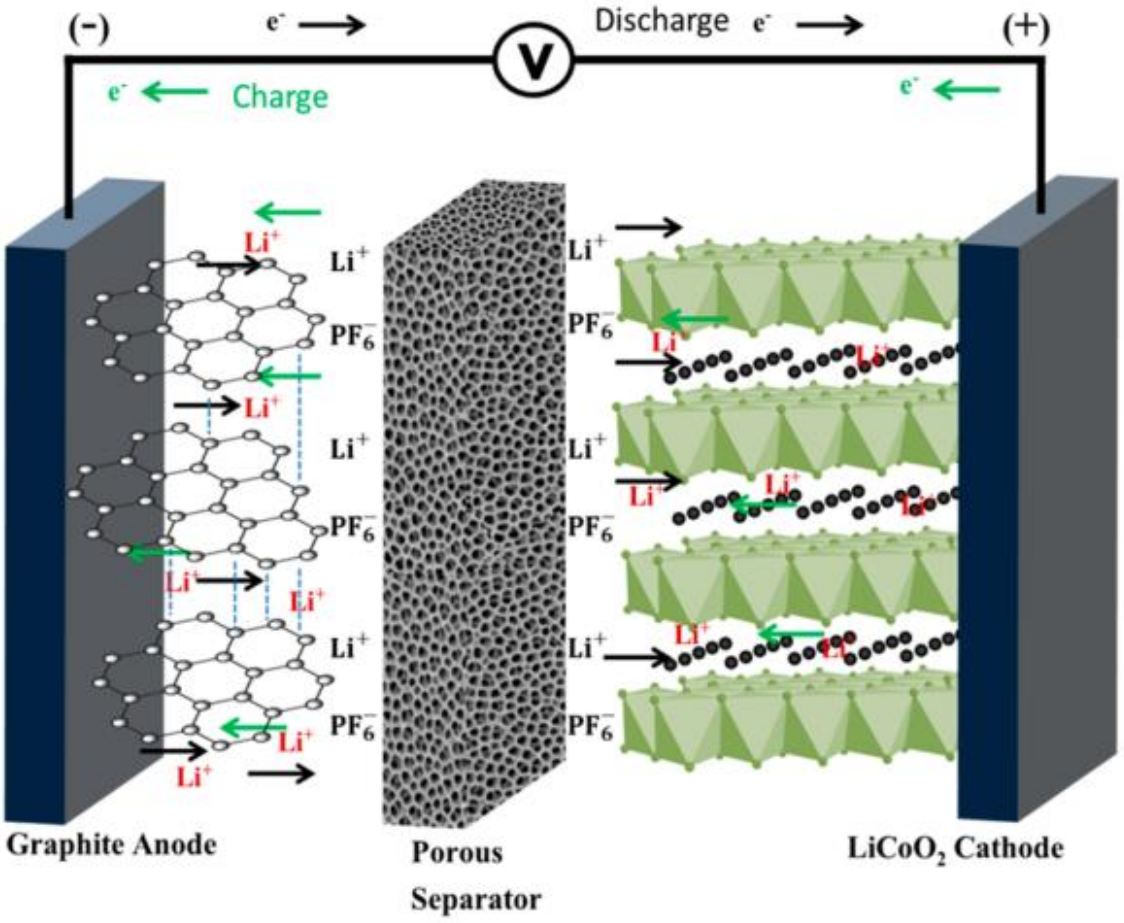

Figure 1.2 Schematic diagram of a conventional Li ion battery, with graphite as the anode, $LiCoO_2$ as the cathode.[5]

As proposed by Liu et al, the long-term goal of developing LMB, is to realize 500 Wh/kg at cell level, 100 $/KWh at pack level.[6] To meet this ambitious goal, many design of current laboratory LMB need to be optimized.

In 2019, Niu et al reported a 300 Wh kg^{-1} pouch cell using Li metal as anode, $LiNi_{0.6}Mn_{0.2}Co_{0.2}O_2$ (NMC622) as the cathode, as shown in Figure 1.3.

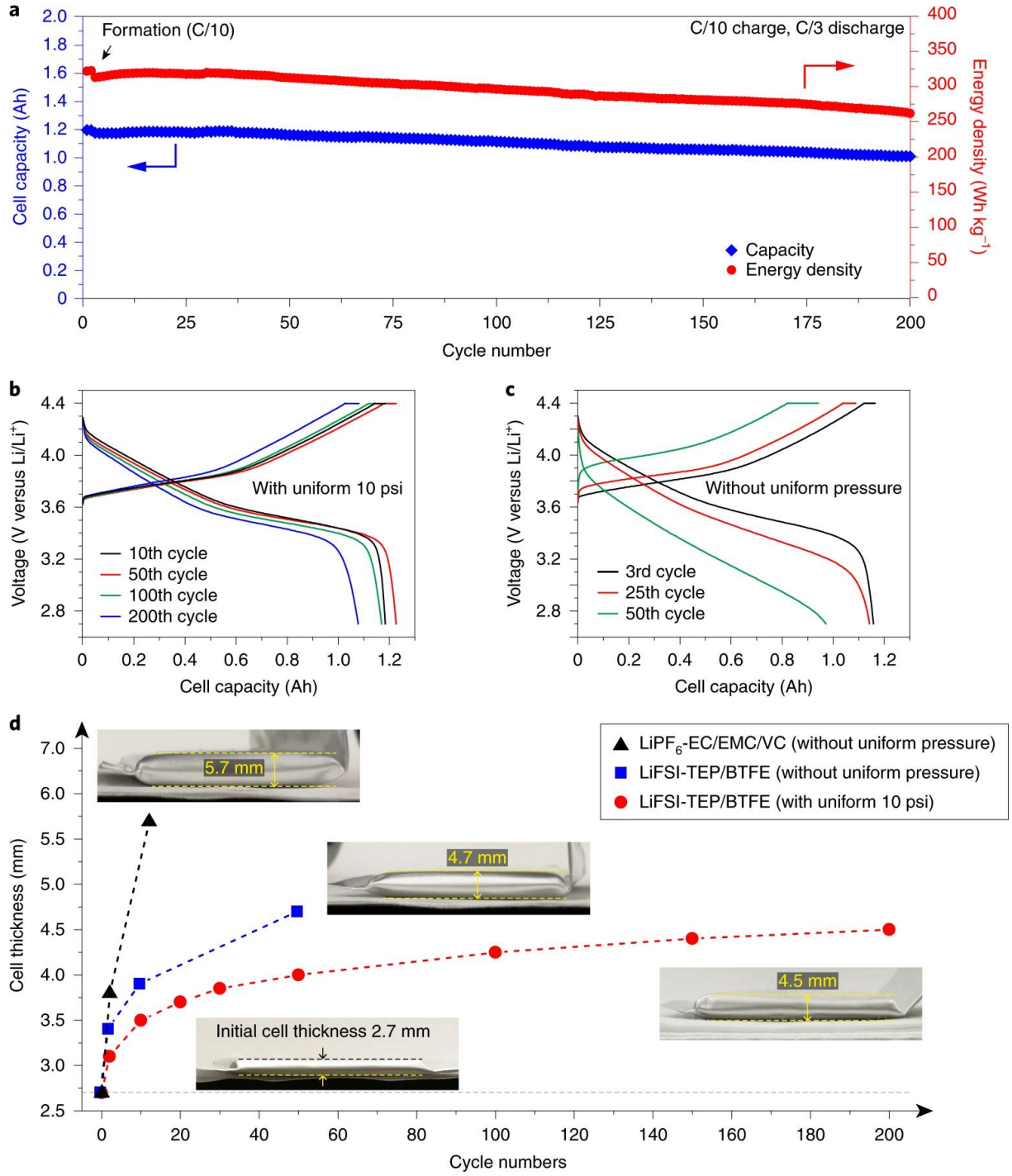

Figure 1.3 a, The cycling performance of a 300 Wh kg-1 pouch cell with a compatible electrolyte and uniform pressure. The energy density is calculated based on the weight of of whole cell. b,c, Corresponding voltage profiles at different cycles. D, The swelling comparison of the three cells made with different electrolyte and applied pressure.[7]

The high energy density of this cell is a result of the pouch cell format and the reduced electrolyte amount. Pouch cell, compared to coin cell, can be fabricated with multi-stacking configuration, which reduced the fraction of inactive components. On the other hand, using lean electrolyte also reduced the inactive weight and boosted the energy density, while the most of cells fabricated in laboratory comprised of flooded electrolyte.

Taking this as baseline, Liu et al proposed a pathway towards designing a cell with 500 Wh kg^{-1} energy density by optimizing cell parameters. As illustrated in Figure 1.4, On the cathode part, high areal loading electrode, combined with reduced porosity, less inactive materials, and higher reversible capacity, is a must to hit the target. Developing Li metal friendly electrolyte and being able to reduce the electrolyte amount to 2.4 g Ah^{-1} is necessary to enable high energy density LMB. On the anode side, reducing the N/P ratio is required, which demands an ultrahigh coulombic efficiency anode with long cycle life.

In summary, the approaches to developing 500 Wh kg-1 LMB lie in three categories: 1) Develop new cathode material or optimize current ones. 2) Develop new electrolytes that work better with Li metal under lean electrolyte condition. 3) Li metal anode optimization.

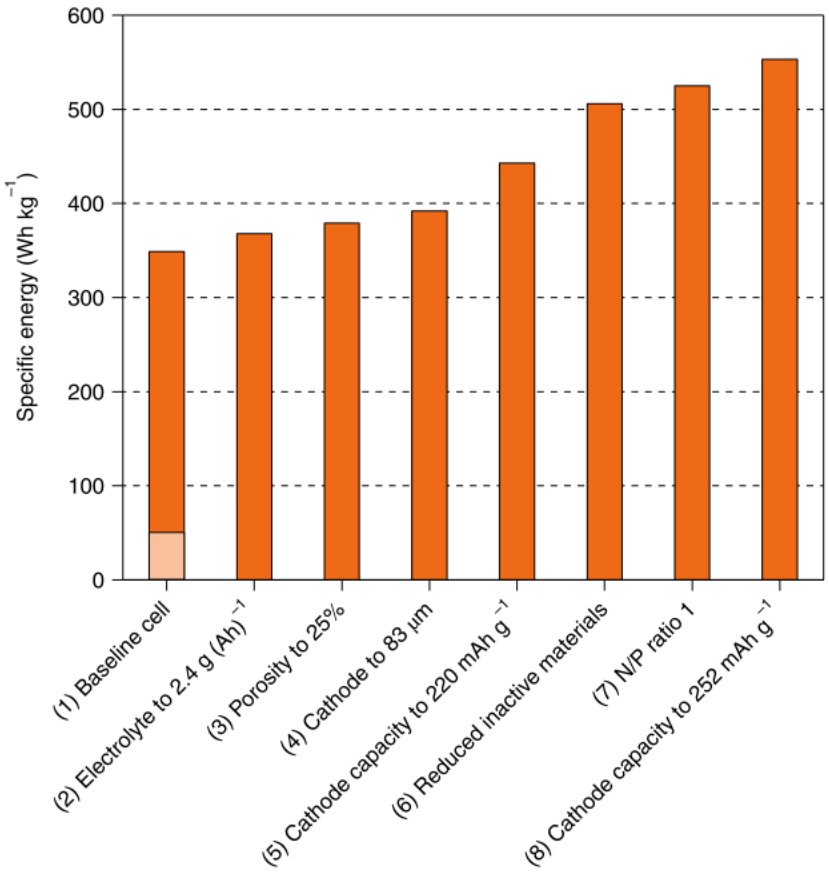

Figure 1.4 calculated cell-level specific energy as a function of cell parameters. (1) A baseline NMC622 material with 196 mAh g^{-1} specific capacity (charge cut-off at 4.6 V), 35% cathode porosity, 22.0 mg cm^{-2} cathode mass loading and 70 µm cathode thickness. The N/P ratio is 2.6 and the electrolyte to capacity ratio is 3.0 g $(Ah)^{-1}$. The lightly shaded area in the baseline cell represents a specific energy much less than 50 Wh kg^{-1} based on the amount of the cathode, anode and electrolyte and other inactive materials reported in most literature studies for rechargeable coin cells. (2) Reducing the amount of electrolyte (electrolyte to capacity ratio) to 2.4 g $(Ah)^{-1}$. (3) Reducing the cathode porosity to 25% so further reducing the electrolyte amount to 2.1 g $(Ah)^{-1}$. (4) Increasing the cathode thickness to 83 µm and mass loading to 26.0 mg cm^{-2} thus increasing the specific capacity of the whole cathode. (5) Increasing the cathode capacity to 220 mAh g^{-1}. (6) Reducing inactive materials (current collector, packaging) by more than 50%. (7) Reducing the Li to N/P ratio of 1. (8) Using hypothetical new cathode materials with a capacity much higher than 250 mAh g^{-1}.[6]

1.2 Nickel rich transition metal oxide cathode materials

Lithium cobalt oxide (LCO) was used as the cathode material when LIB was first commercialized, which is still widely used in consumer electronics today due to its high volumetric energy density. However, only half of Li in the LCO cathode can be reversibly cycled due to the concerns about crystal structure collapse, resulting in a limited capacity of around 160 mAh g^{-1}. The graphite anode, on the contrary, delivers more than 320 mAh g^{-1} capacity. The development of Si/C as the anode material further increased the anode capacity, making the cathode as the bottleneck.

Another driving force to develop new cathode material is the high price and limited reservoir of cobalt. As the Li ion battery market growing fast in the past twenty years, the cobalt price has surged, and its supply chain is under high risk. Over 50% of cobalt production occurred in the Democratic Republic of the Congo, which is politically unstable.[8] Therefore, a great need to reduce the usage of cobalt is rising.

One promising cathode material is the nickel rich transition metal oxide, which is of similar layered structure as LCO but replacing the cobalt by nickel and manganese. Its structure is shown in Figure 1.5 and is typically denoted as $LiNi_xMn_yCo_zO_2$ (NMC). The Li^+ and transition metal ions (TM^{n+}) are ordered on the alternate (111) planes of rock salt structure with cubic close-packed array of oxide ions. The layered structure provides Li ion diffusion channels. More specifically, the lithium ion hops from one octahedral site to another via a neighboring tetrahedral void in the lithium plane, as illustrated in Figure 1.6. The diffusion channels provide ionic conduction pathway, while the electronic conductivity of NMC material falls into the semiconductor range, ~ 10^{-6} to 10^{-2} S cm^{-1} depending on the state of charge (SoC).

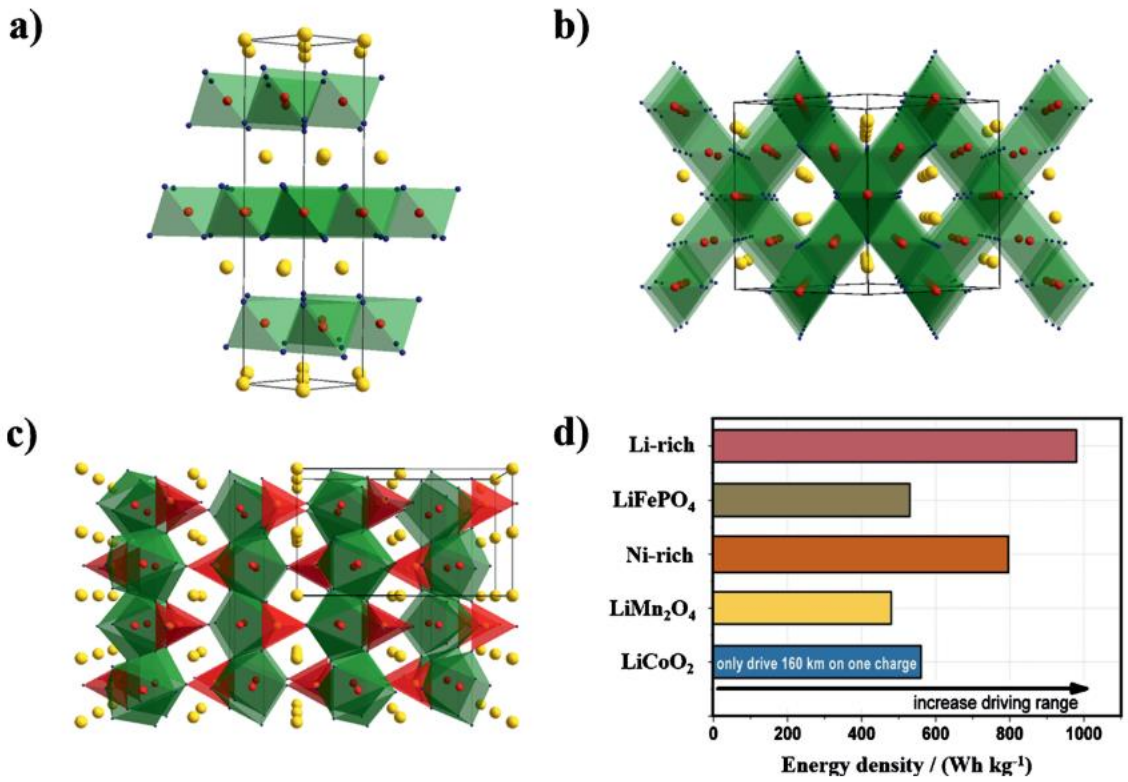

Figure 1.5 illustration of crystal structure of main cathode materials: a) $LiCoO_2$ with layered structure, b) $LiMn_2O_4$ with spinel structure, c) $LiFePO_4$ with olivine structure, d) energy density of typical cathode materials.[9]

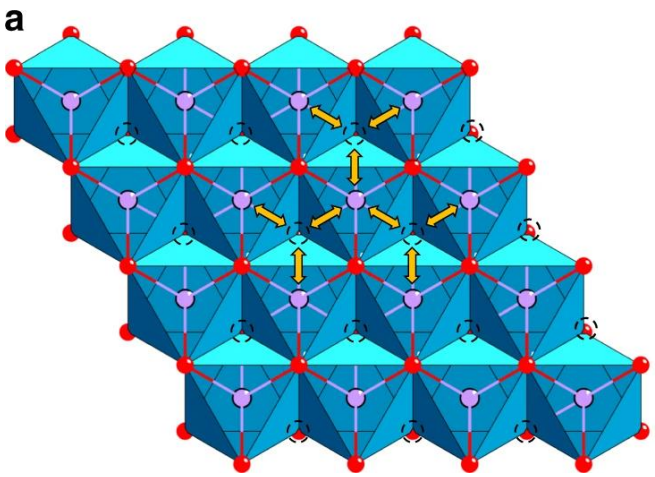

Figure 1.6 Lithium-ion conduction mechanism in layered oxide cathode material. a, Two-dimensional lithium diffusion from one octahedral site to another octahedral site in the lithium plane through a neighboring empty tetrahedral site in the O3 layered $LiMO_2$ cathodes.[10]

A series of NMC material, with various amount of transition metal substituents, have been studied. A general trend is that the higher the nickel content, the higher the specific capacity it delivers at the same voltage. NMC, especially nickel-rich NMC, practically delivers more than 210 mAh g^{-1} capacity with ~80% Li extraction at moderate voltage. The higher capacity it delivered is mainly associated with the lower redox energy of $Ni^{3+/4+}$ compared to $Co^{3+/4+}$, as shown in Figure 1.7.

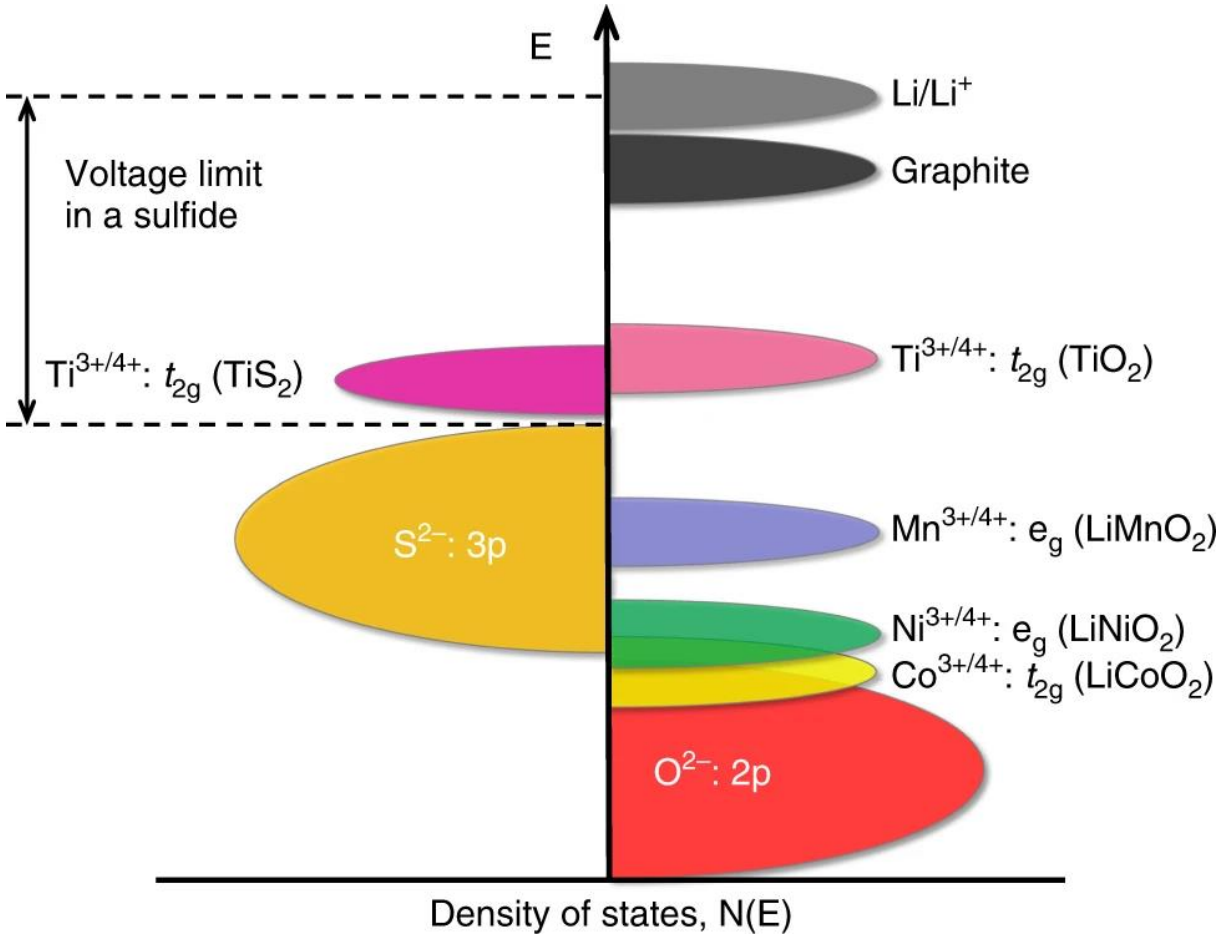

Figure 1.7 Positions of the redox energies relative to the top of the anion: p bands.[10]

Additionally, higher nickel content means less cobalt, which reduces the cost. However, substituting cobalt with nickel is a double-edge sword. On the one hand, it increases the capacity and reduces the material cost due to the cheaper price of nickel. On the other hand, antistites effect was often observed in nickel rich NMC due to the cation mixing caused by the similar radius of Li^+ (0.076 nm) and Ni^{2+} (0.069 nm). More importantly, recent reports have shown that there is an unavoidable lattice collapse for Ni-rich cathode material when charged to high state of charge (SoC).

In summary, Ni-rich NMC is a promising cathode material with high capacity, high energy density, and low cost, but suffers from interfacial side reactions, cation mixing, and lattice collapse problems, which requires further optimizations.

1.3 Sulfurized polyacrylonitrile

Sulfur is a promising cathode material for next generation energy storage system. The specific capacity of sulfur (1675 mAh g^{-1}) is six times as high as the state of art Li-ion battery cathode (~200 mAh g^{-1}). In addition to the high capacity, its natural abundance and environmental benign attributes also make it a good cathode candidate. However, the insulating nature of elemental sulfur and its discharge product is one of the hinderance of its practical application. The price of sulfur ($ 150 ton^{-1}) is almost two orders of magnitude lower than that of $LiCoO_2$ (($ 10000 ton^{-1}). Besides that, the notorious polysulfide dissolution and large volume expansion (80%) also impeded the industrial deployment of sulfur cathode.

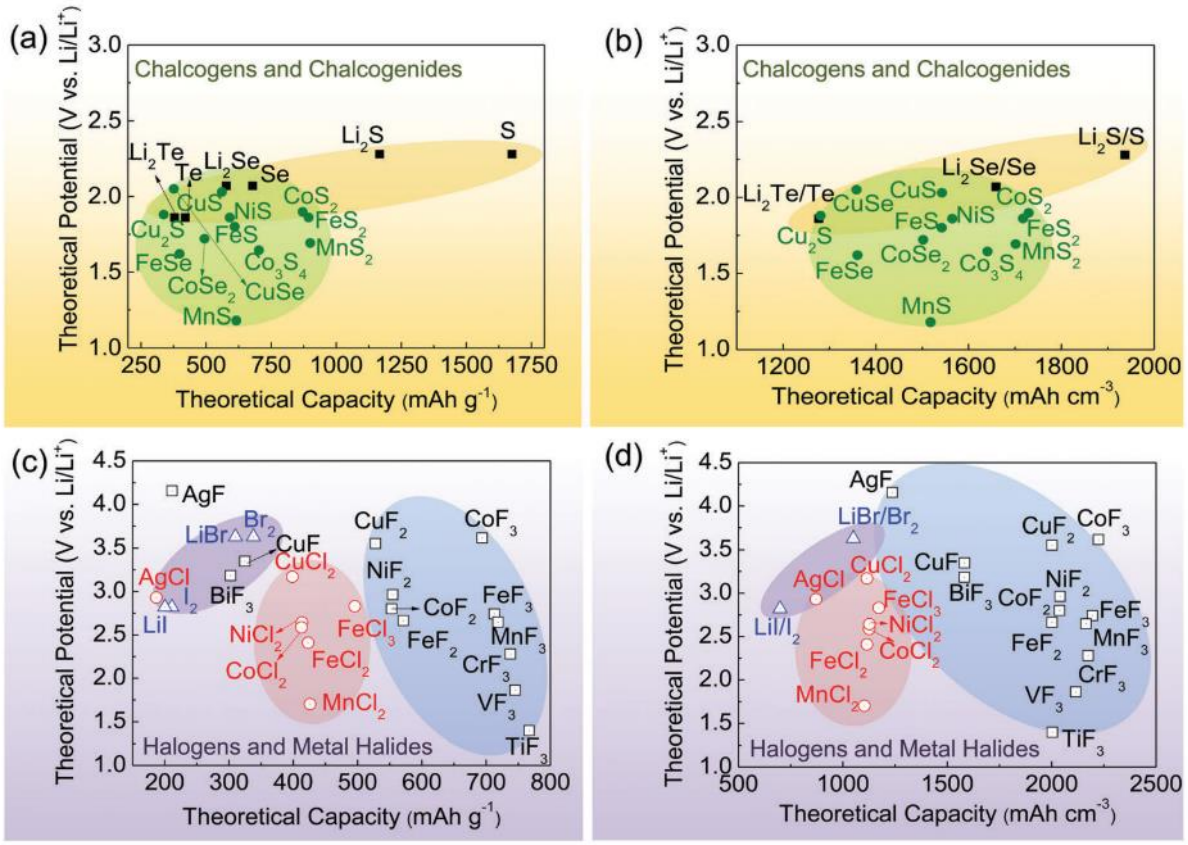

Figure 1.8 Theoretical gravimetric and volumetric capacities and theoretical potential of selected conversion cathode materials: (a and b) chalcogens and chalcogenides; (c and d) halogens and metal halides.[11]

To address the above-mentioned problems, many approaches have been tried. One of the most promising one is to covalently bond sulfur to conductive polymer, which not only restricts the sulfur dissolution but also provides electronic conductivity. Wang et al. reported a sulfurized/ pyrolyzed polyacrylonitrile (SPAN) composite material synthesized by reacting sulfur and polyacrylonitrile (PAN) at elevated temperature.[12]

At elevated temperature (300-450 °C), polyacrylonitrile become cyclic through dehydrogenation reaction with sulfur. Typically, the synthesis method starts with ball milling sulfur and PAN to get a uniform mixture. After that, the mixture will be transferred to a tube furnace with continuous Ar flow for heat treatment.

Figure 1.9 illustrated a possible reaction route for the SPAN synthesis. First, the sulfur transforms into linear polysulfane through ring-opening polymerization. Then it polymerizes into polymeric sulfur with the remaining diradical chain ends. Subsequently, the radical attacks the nitrile carbon to form C-S, which followed by cyclization. Another study indicates that during SPAN synthesis the PAN cyclize first, and then sulfurization and dehydrogenation take place.

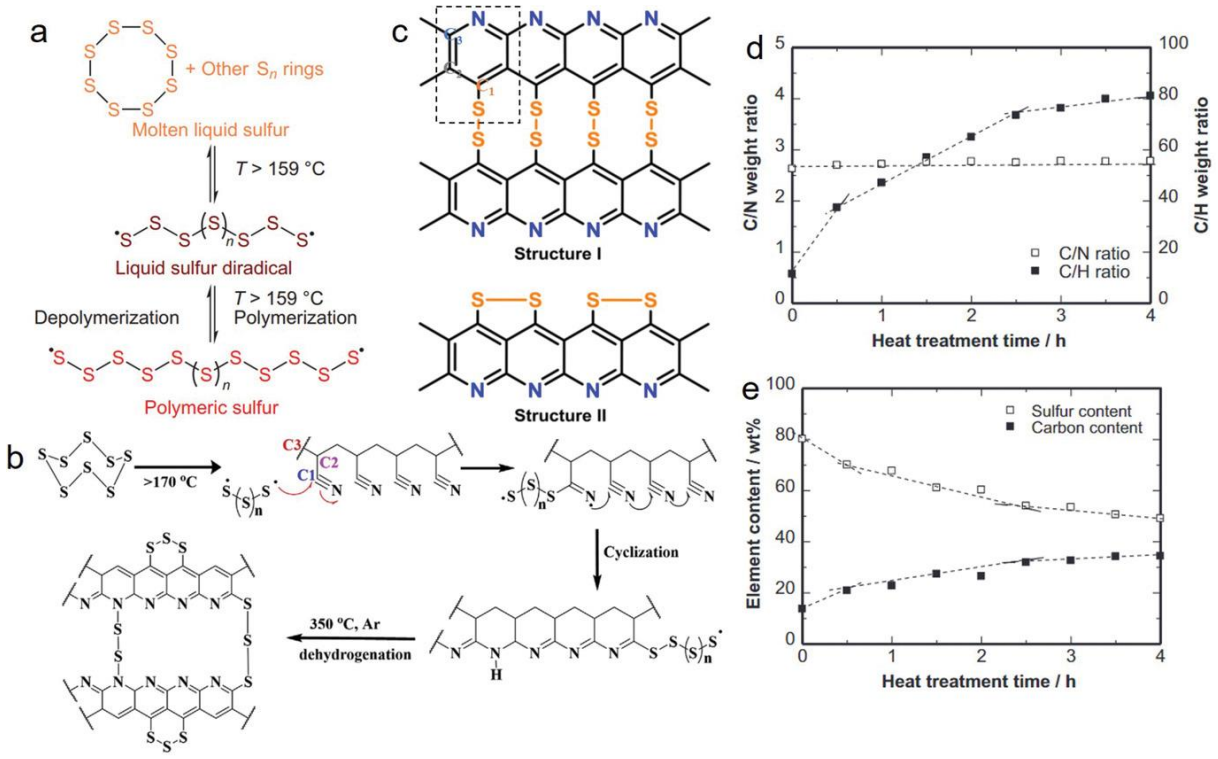

Figure 1.9 Schematic of reaction routes for SPAN materials.[13]

The exact chemical structure of SPAN is still under debate due to its complicated polymer nature. But it is generally agreed that short chain sulfur is covalently bonded to a fused pyridine ring, as illustrated in Figure 1.10 and 1.11.

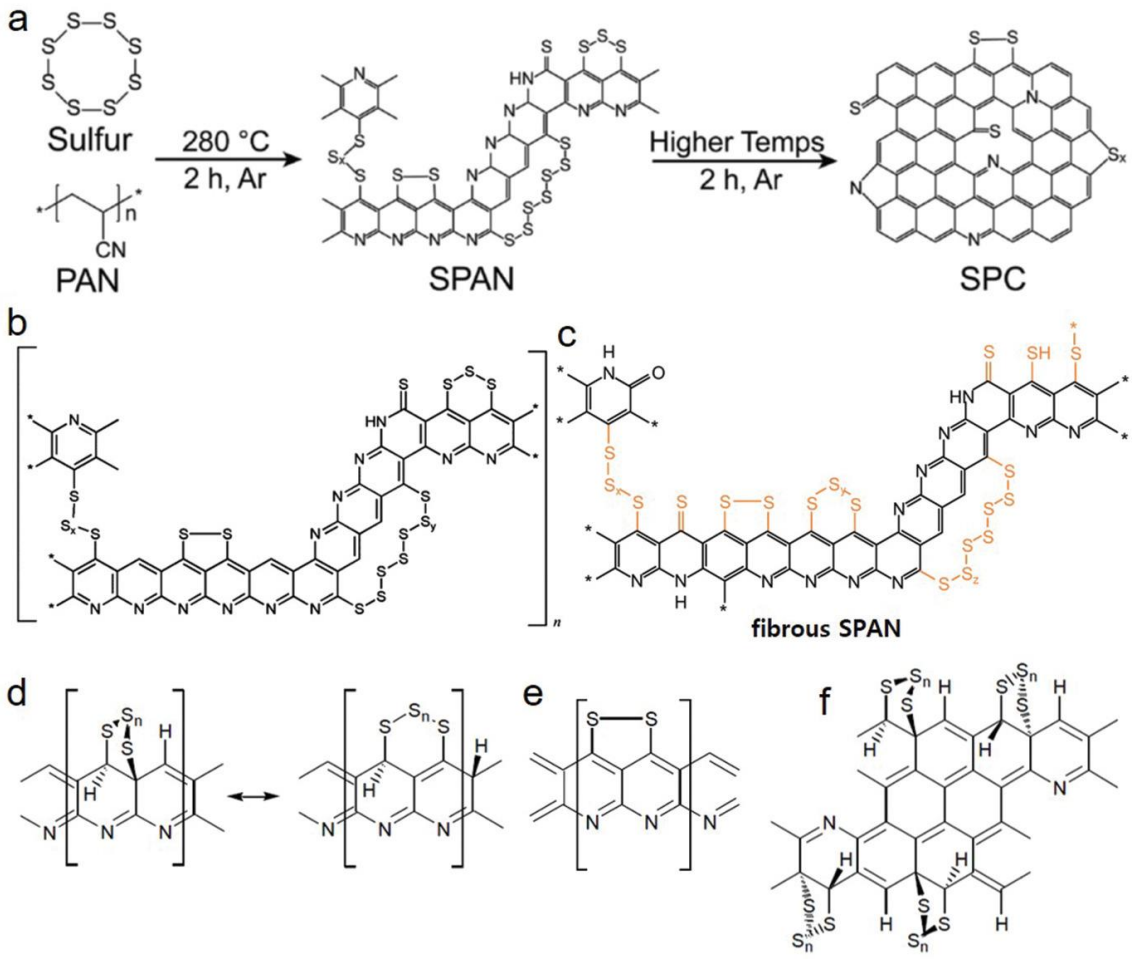

Figure 1.10 Schematic of covalent chemical structures for SPAN materials.[13]

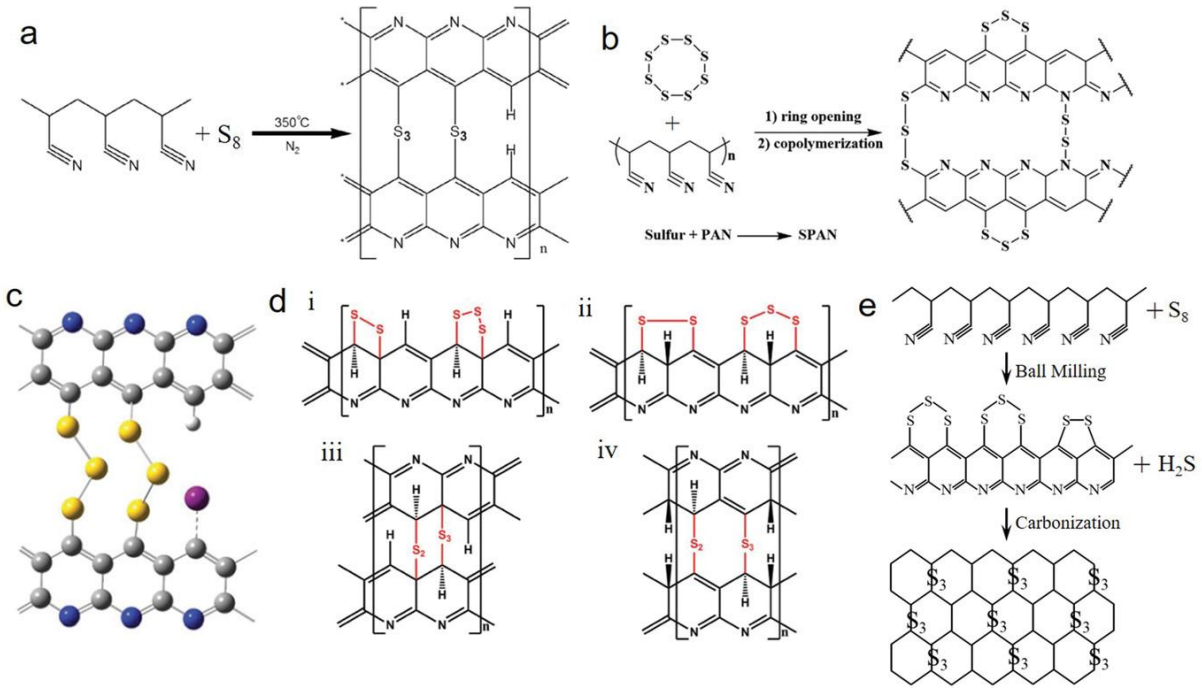

Figure 1.11 Schematic of covalent chemical structures for SPAN materials.[13]

SPAN shows significantly improved cyclability compared to elemental sulfur. Surprisingly, it is compatible with carbonate electrolyte, in contrast to the instability of elemental sulfur in carbonate esters. The polysulfide generated during sulfur lithiation process react with carbonate electrolyte, while the discharge mechanism of SPAN is solid-solid conversion, which does not involve polysulfide. As a result of the unique lithiation mechanism, SPAN does not show capacity fading in carbonate electrolytes.[14]

However, to deliver high energy density at cell level, high areal capacity cathode is needed as we previously discussed. Increasing the capacity will lead to high current density and deeper cycling of the Li metal anode, which is naturally unstable against carbonate electrolyte. The Li impedance increases fast due to the severe side reaction between electrolyte and Li metal. The morphology of Li gets increasingly dendritic after repeated cycling, which potentially leads to internal shorting.

To address the above-mentioned problem, advanced electrolyte systems have been developed, which is compatible with both SPAN cathode and Li metal anode. Fluorinated carbonate electrolyte was designed to improve the cyclability of Li-SPAN batteries, as shown in Figure 1.12. Stable and fast cycling of Li-SPAN battery was realized in a FEC-based electrolyte.

Ether electrolyte is known to have better compatibility with Li metal due to its higher LUMO level and better Li deposition morphology. However, SPAN dissolves in typical ether electrolyte leading to polysulfide shuttling. Through proper electrolyte design, this issue has been overcome by using concentrated ether electrolyte as shown in Figure 1.13, which demonstrated stable cycling of Li-SPAN battery for more than thousand cycles.

As discussed in previous section, realizing stable cycling of lean electrolyte battery is of critical importance to raise its energy density. In the Li-SPAN case, there are two bottle necks. One is the Li metal anode, which after cycling often shows porous and mossy morphology. The porous structure will absorb electrolyte from the other part of the cell, leading to electrolyte depletion and cell impedance rise. The other is the SPAN cathode, which is typically highly porous to accommodate its volume expansion. The electrolyte regulation often leads to denser Li deposit, which alleviate the electrolyte depletion problem on the anode side.

A report has shown that using a multifunctional flexible binder, the cathode porosity could deliver stable cycling performance at 13.3% porosity, leading to significantly improved lean electrolyte performance. (Figure 1.14) Although the cell only less than 30 cycles, it indicates a promising approach towards the lean electrolyte Li-SPAN battery.

In summary, SPAN is a promising cathode candidate for next generation energy storage system with low cost. Its non-negligible volume expansion and the Li metal issue are the two main problems associated with the Li-SPAN system.

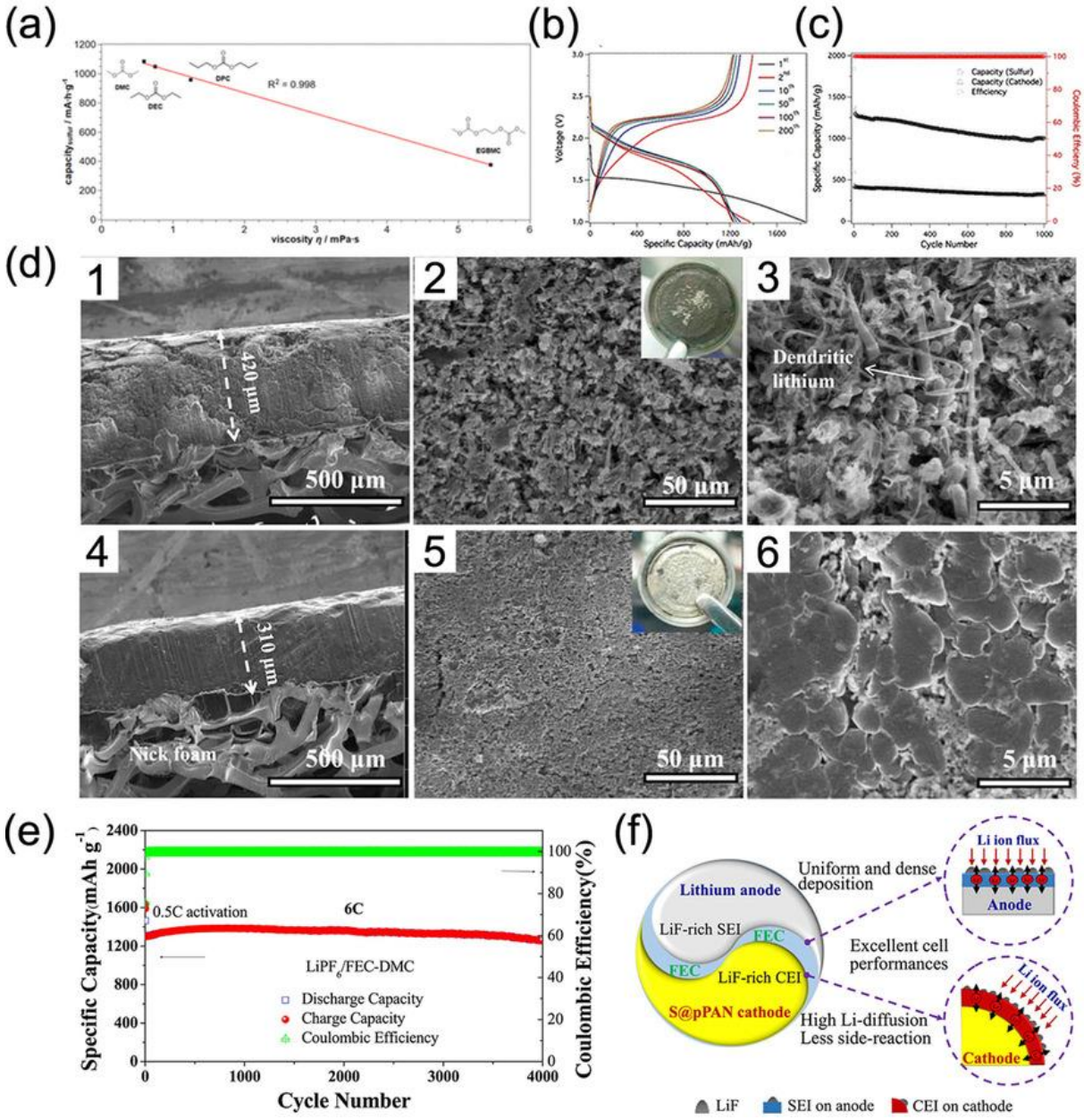

Figure 1.12 Electrolyte regulation in carbonate-based liquid electrolyte. (a) Linear correlation between the viscosity and the discharge capacity in the 2nd cycle using different carbonates. (b) Electrochemical discharge and charge curves of various cycles at 0.4 C and (c) cycling performances of of Li–SPAN cells. (d) Morphology of Li mental anode in different carbonate electrolytes. Cross-section views (d1, d4) and top views (d2, d3, d5, d6) of Li electrodes recovered from Li|Li cells cycled at 1.0 mA cm-2 after 100 cycles using conventional EC-based electrolyte (d1, d2, d3) and FEC-based electrolyte (d4, d5, d6). Inset images are optical picture of corresponding Li anodes. (e) Long-term cycling performances of Li–SPAN cells in FEC-based electrolyte at 6.0 C. (f) Schematic illustration of FEC-based electrolyte in a Li–SPAN battery.[15]

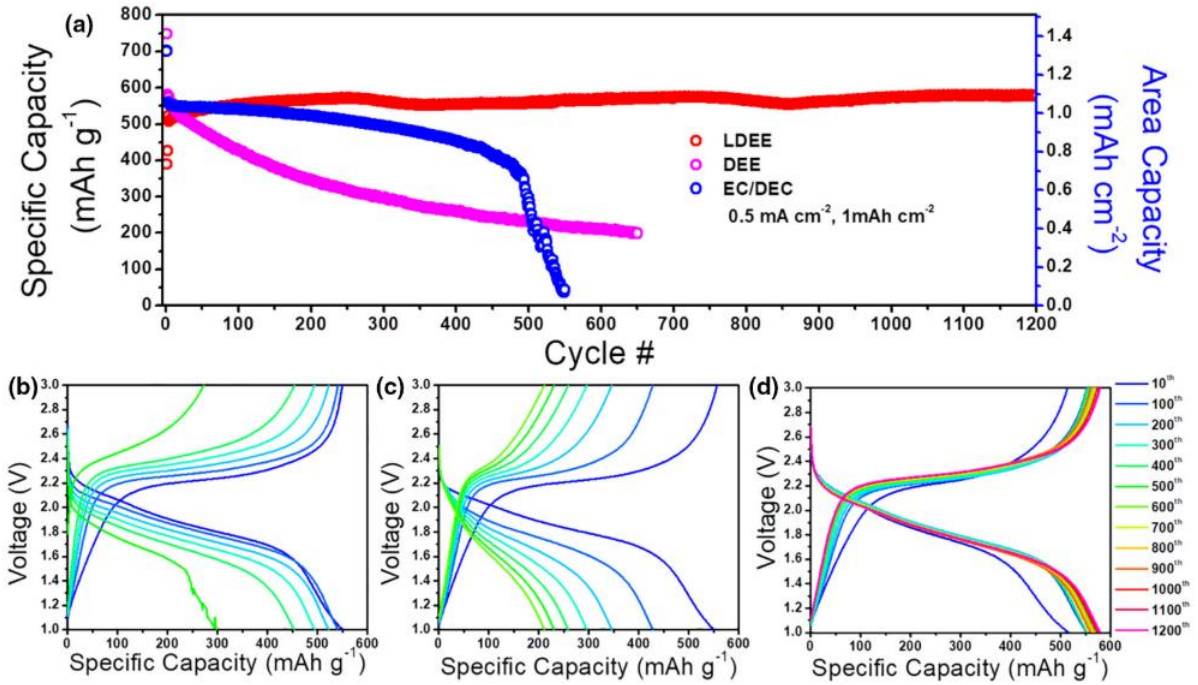

Figure 1.13 Cycling performance of Li||SPAN cells. (a) Comparison of capacities of SPAN in different electrolytes. Charge/discharge voltage profiles of SPAN: (b) in 1 M LiFSI/EC-DEC electrolyte. (c) In 1 M LiFSI/DEE electrolyte. (d) In 1.8 M LiFSI/DEE-BTFE electrolyte. At 0.5 mA cm?2, between 1 V and 3 V. The lithium chips are 250 mm. The N/P ratio is ?43.2. Flooded electrolyte is used.[16]

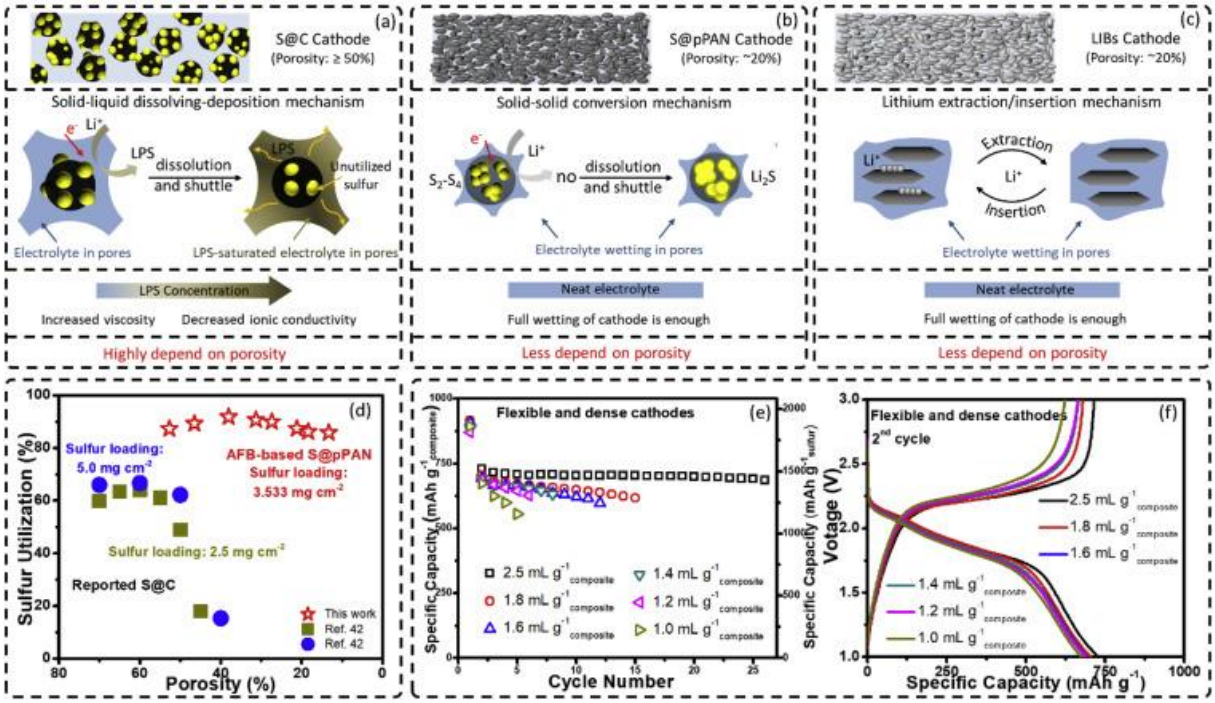

Figure 1.14 Electrochemical performance of lean electrolyte Li-SPAN batteries. a-c) Reaction mechanisms of different cathodes with low porosity: S@C cathode (a); S@pPAN cathode (b); LIBs cathode (c); d) Comparison of sulfur utilization-cathode porosity between reported S@C cathode and AFB-based S@pPAN cathode; e) Electrochemical performance under lean electrolyte; f) Charge/discharge profile.[17]

1.3 Li metal anode

Li metal is the most promising anode material for next generation energy storage system due to its high capacity and low electrochemical potential. However, it suffers from many problems, as shown in Figure 1.15. The most negative standard reduction potential is actually a double edge sword. It leads to inevitable chemical or electrochemical reactions between Li metal and electrolytes. This process not only consumes both electrolyte and Li inventory, but also generates an additional layer of material at the electrode-electrolyte interfaces. This layer of reaction product is called solid electrolyte interface (SEI), which is expected to prevent further reactions between the electrode and electrolyte. However, the SEI layer on Li metal experiences continuous breakage and reformation process due to the infinite volume expansion of the Li dissolution and deposition process.

In addition to the Li inventory loss and impedance growth through chemical reactions, unfortunately there is also a physical loss, as illustrated in Figure 1.16. Electrochemical deposition of Li often appears to be dendritic and porous, which resulted in non-uniform dissolution in the stripping process. The uneven dissolution usually leads to breakage of Li dendrites. The freshly exposed Li surface will immediately be covered by SEI layer due to its reactive nature, which will electronically separate that Li-island from the entire electrode. This is so-called the “dead” Li, which is chemically still active but electrochemically “dead”. Furthermore, the accumulation of “dead” Li adds up to the cell impedance as well.

Besides the degradation, internal short is another problem impeding the commercialization of LMB, which is highly related to the dendrite growth.

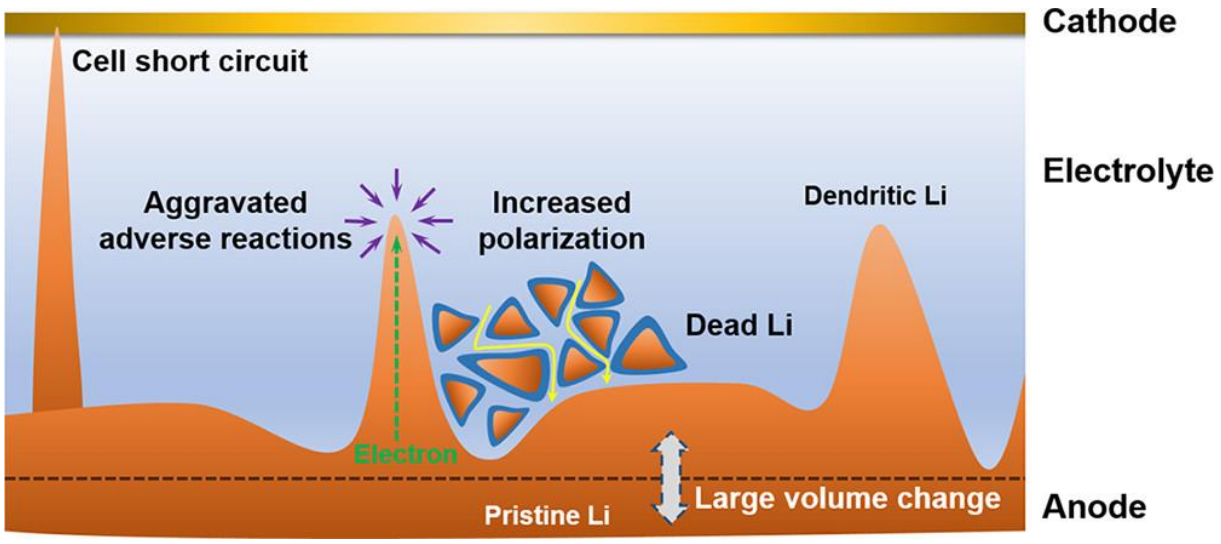

Figure 1.15 Schematic illustration of the challenges Li metal anode facing.[18]

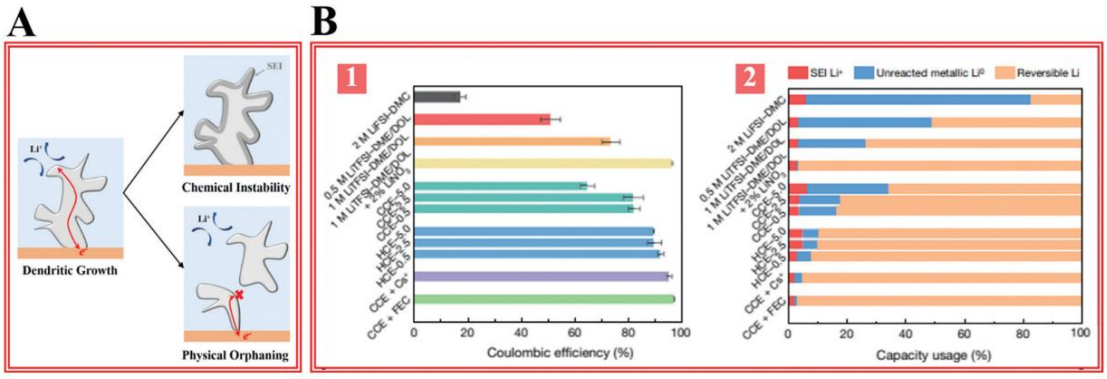

Figure 1.16 The origins of Li loss. (A) Irregular, noncompact growth of Li leads to chemical and physical instabilities. (B-1) Li plating/stripping coulombic efficiency in different electrolytes. (B-2) Quantification of Li loss via different mechanisms.[19]

To suppress the degradation and internal shorting, regulating the Li deposition morphology is an urgent task. A dendrite-free and dense Li deposition will significantly reduce the contact area between Li and electrolyte, leading to less chemical degradation. Dead Li formation will also suppressed if there is no dendritic Li.

Many approaches have been proposed to regulate Li deposition. Electrolyte optimization is one of the most intuitive ways to tune the deposition morphology. The conventional carbonate electrolyte is known to promote dendrite growth and reacts with Li metal rapidly. Although fluorinated carbonate can alleviate the dendrite growth and reduce the reactivity, the coulombic efficiency is typically around 97%, which is far less than the LIB with graphite as the anode (>99.9%). Ether electrolyte is inherently more stable against Li metal due to its higher LUMO level and generally produces denser Li deposition. However, the higher reductive stability comes with price of lower oxidative stability. Most of the ether electrolytes decompose at voltage higher than 4 V, which makes it incompatible with the LCO and NMC cathode. Its electrochemical stability window limits the cathode choices to lithium iron phosphate (LFP) and sulfur, where the former delivers lower energy, the latter is not commercially available yet. To enlarge the stability window, concentrated ether electrolyte was developed. Leveraging its higher oxidation potential, 4 V cathode was paired with Li anode to deliver high energy density. Nevertheless, the concentrated electrolyte suffers from high viscosity and lower ionic conductivity, which induce lots of problems. Poor wettability of the electrolyte as a result of the high viscosity adds additional difficulty to the cell assembly, especially when thick cathode is used. The low ionic conductivity limits the rate performance of the cells with concentrated electrolyte due to mass transport issue. Additionally, the massive usage of the expensive Li salts significantly increased the electrolyte prices.

To address the above-mentioned dilemma, localized high concentration electrolyte (LHCE) was proposed. (Figure 1.17) It has all the advantages that the concentrated electrolyte has but does not share its disadvantages. LHCE was made by diluting concentrated electrolyte with non-solvating electrolyte, typically a highly fluorinated solvent. Since the diluent is non-solvating

solvent, it does not interfere with the solvation structure of concentrated electrolyte, which keeps the contact-ion-pair (CIP) structure and the enlarged electrochemical stability window. On the other hand, benefited from the diluent the viscosity and ionic conductivity is exceptionally higher than the concentrated one.

Leveraging the benefits of LHCE, a recent report has built a 350 Wh kg^{-1} pouch cell with 600 cycles before the cell capacity degraded to 76% of its original capacity (Figure 1.18), which demonstrates the promising future of LHCE.

In addition to the electrolyte optimization, applying protective coating on Li metal is another approach to improve the performance of LMB. On the one hand, protective coating prevents the direct contact between Li and the electrolyte, reducing the electrolyte consumption by parasitic reactions. On the other hand, depending on the mechanical property of the coating, the dendrite growth can be suppressed by the physical confinement of the coating layer. An example is illustrated in Figure 1.19, a reactive polymer composite was applied on Li metal to produce artificial SEI and prevents electrolyte accessing the Li surface. A 99.1% coulombic efficiency was realized in carbonate electrolyte, which typically shows ~ 95% efficiency.

Substrate modifications have also been tried to improve the performance of LMB. Cu is typically used as the current collector for Li deposition due to its abundance and appropriate electrochemical stability window. However, Cu foil often comes with native oxide layer and other contaminations, which affects the reaction heterogeneity when plating Li. Therefore, modifying the substrate becomes an intuitive way to regulate Li deposition. Cu_3N was used as a current collector modification, as shown in Figure 1.20. Copper nitride was chosen because its lithiation product, in-situ generated Cu and Li_3N, provides uniform electronic and ionic conductivity.

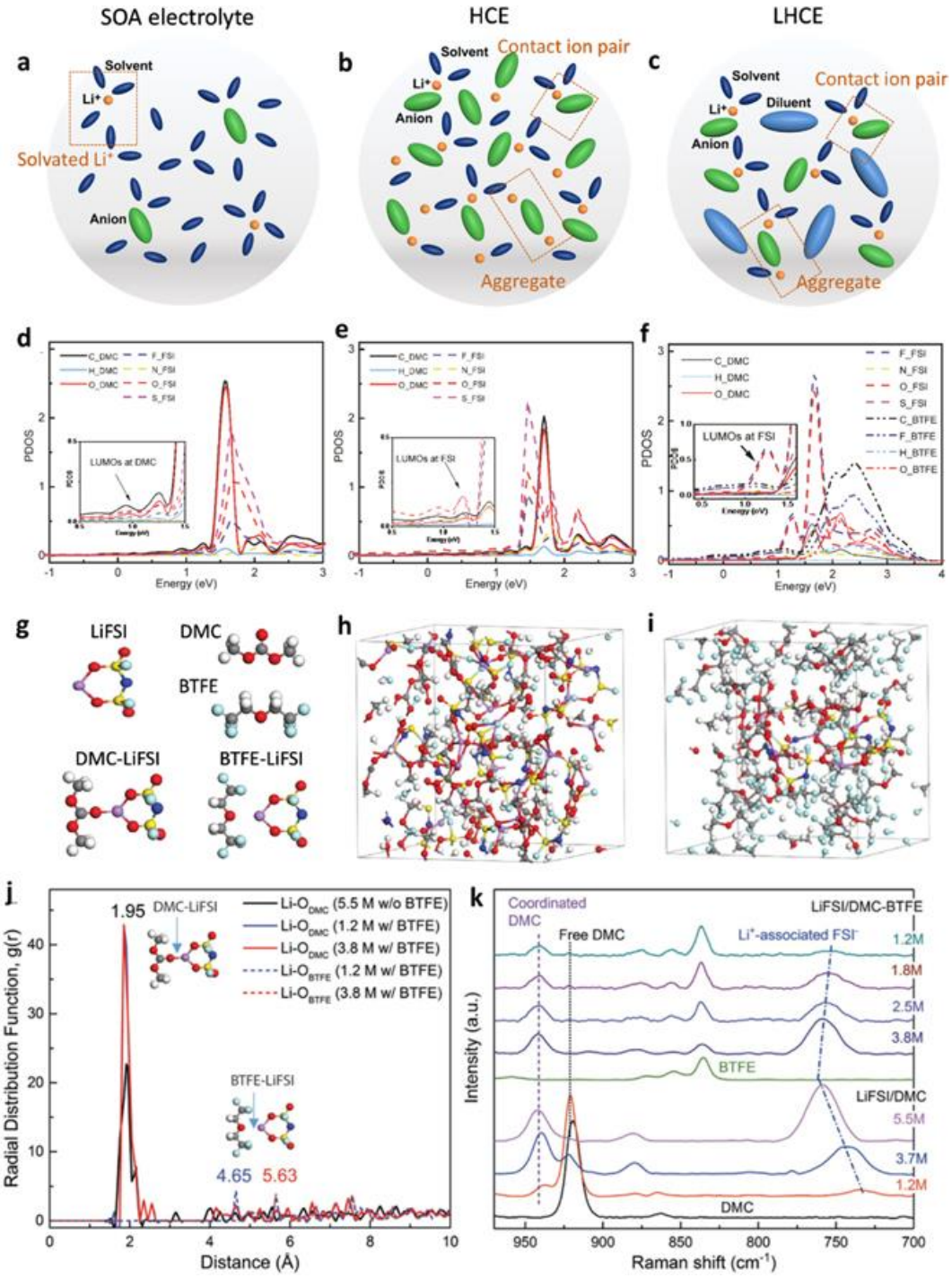

Figure 1.17 Structure of different electrolyte system. (a)–(c) Electrolyte structures of (a) conventional electrolyte, (b) HCE and (c) LHCE. (d)–(f) Projected density of states (PDOS) of each atom on the Li anode in three electrolytes. (g)–(k) Li ion coordination and component distribution in the LHCE of LiFSI/DMC-BTFE. (g) Optimized structures of electrolyte components, and the solvent-salt pairs of DMC-LiFSI and BTFE-LiFSI. Snapshots of (h) HCE, (i) LHCE and (j) radical distribution functions of Li-ODMC and Li-OBTFE from ab initio molecular dynamics (AIMD). (k) Raman spectra of the different electrolytes.[20]

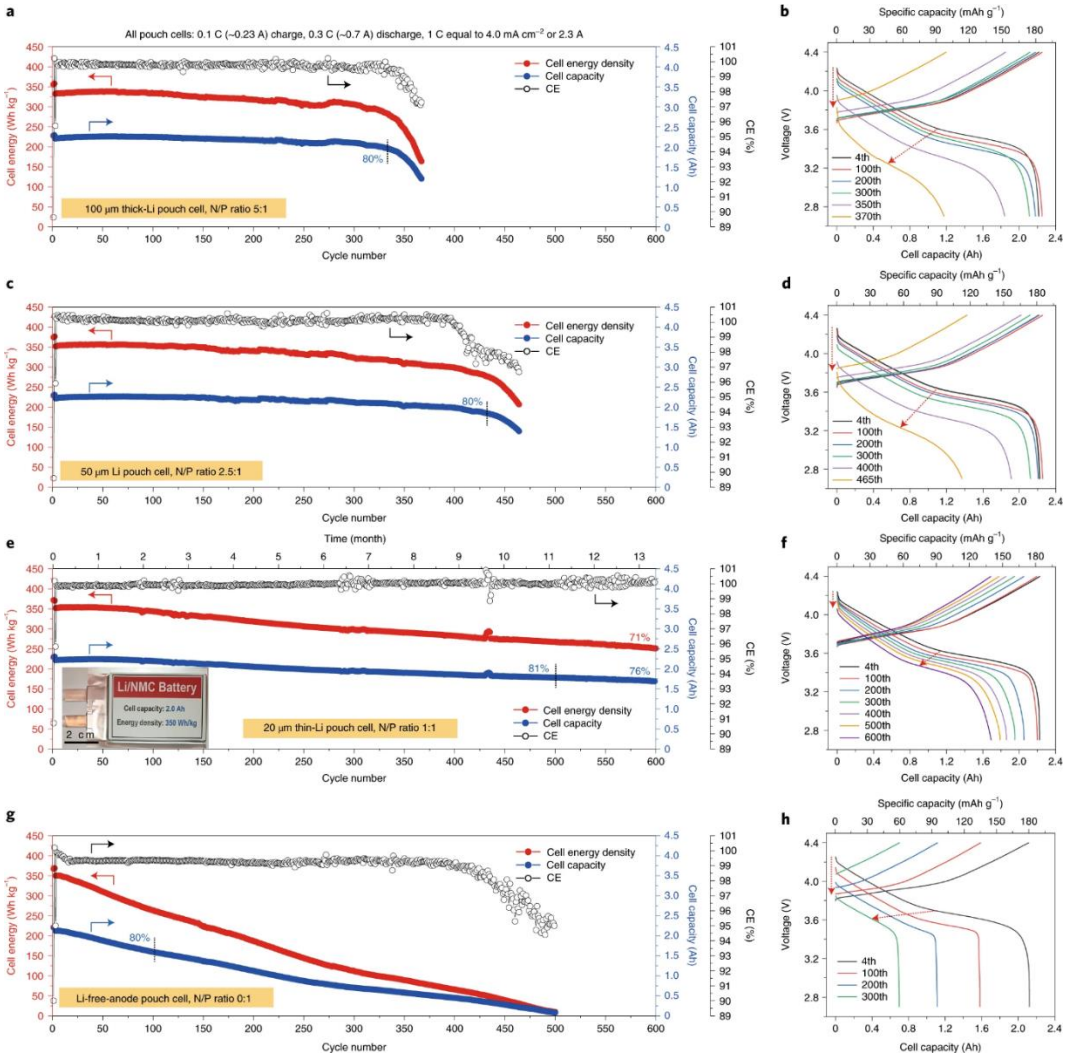

Figure 1.18 Electrochemical performance of Li metal pouch cell with different NP ratio. a,b, Cell-level energy density, cell capacity, CE and charge–discharge curves of the pouch cell with 100 μm thick-Li in the anode; the N/P ratio is 5:1. c,d, Cycling performance and charge–discharge curves of the 50 μm Li pouch cell; the N/P ratio is 2.5:1. e,f, Cycling performance and charge–discharge curves of the 20 μm thin-Li pouch cell; the N/P ratio is 1:1 and the E/C ratio is 2.4 g Ah^{-1}. g,h, Cycling performance and charge–discharge curves of the Li-free-anode pouch cell, Cu || NMC622; the N/P ratio is 0:1. All pouch cells were cycled at 0.1 C for two initial formation cycles, and then charged at 0.1 C (the electric current is ~0.23 A) and discharged at 0.3 C (the electric current is ~0.7 A) in subsequent cycles (1 C equals 4.0 mA cm^{-2} or corresponds to 2.3 A, from 2.7 V to 4.4 V, 25 °C). The arrows indicate the voltage changes during the charge–discharge processes. During the long testing of more than 13 months, these pouch cells suffered two power outages and one period of oven maintenance, so some cycling behaviors show fluctuations. Note that the cell energy density is calculated based on the total weight of the whole pouch cell, including all active and inactive parts in the pouch cell.[21]

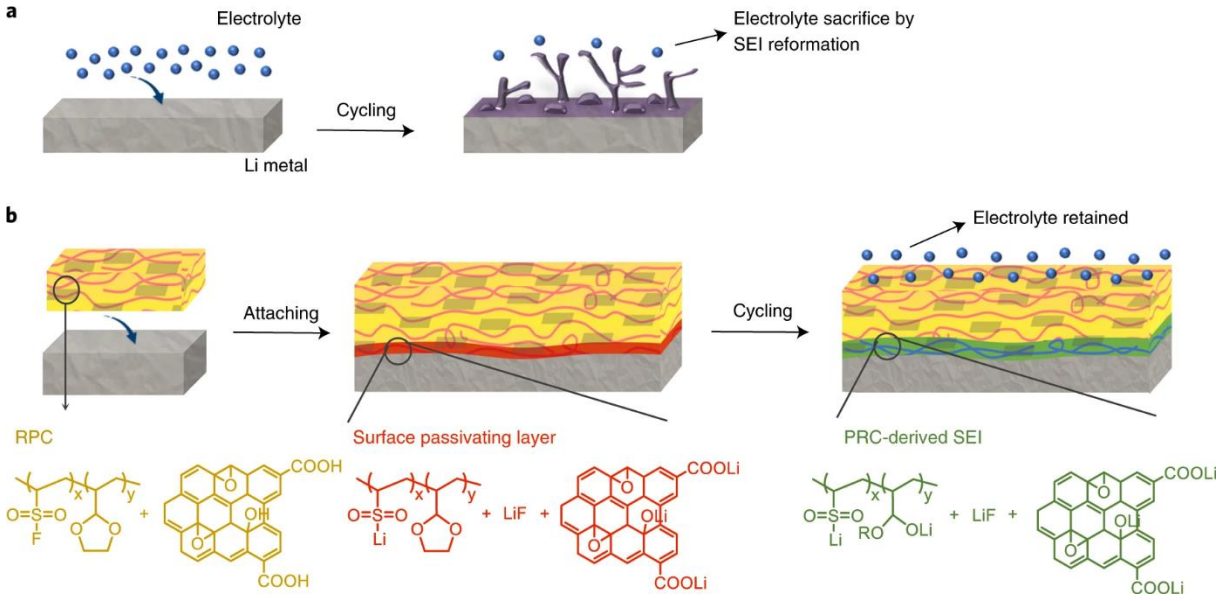

Figure 1.19 Schematic illustration of the comparison between interface formed with traditional liquid electrolyte and PRC layer. a, Formation of an electrolyte-derived SEI via electrolyte decomposition. The SEI layer (purple) is constantly breaking and consuming electrolyte on cycling. b, Design of a polymer–inorganic SEI using the RPC precursor rather than the electrolyte. The RPC layer first passivates the Li surface by a chemical reaction. The products form a dense layer (red) that blocks electrolyte access to the surface. The attached RPC subsequently generates polymeric salts and nanoparticles of Li salts on-site. GO nanosheets complete the SEI layer (green). The unreacted RPC (yellow) acts as a reservoir to maintain the SEI structure on cycling.[22]

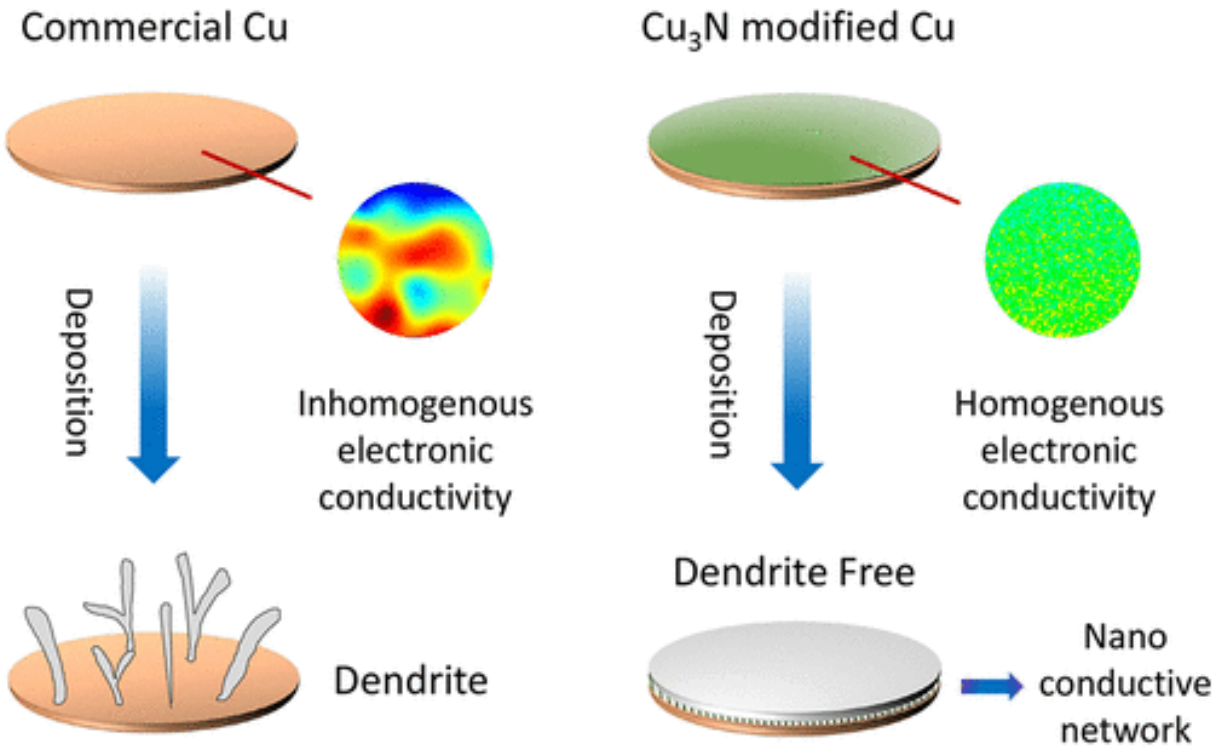

Figure 1.20 Schematic illustration of Li plated on commercial Cu foil and Cu3N modified Cu.[23]

In summary, Li metal is the holy grail of rechargeable battery anode, but it suffers from many problems, including parasitic reactions, irregular deposition, volume expansion, etc. Regulating the deposition morphology is one of promising solutions to these problems.

CHAPTER 2 FIRST CYCLE LOSS OF LAYERED OXIDE CATHODE MATERIALS: WHAT IS THE ROOT CAUSE OF POOR KINETICS?

2.1 Introduction

Layered transition metal oxide has been widely applied as cathode materials for both portable electronic devices and electric vehicles due to its high voltage, capacity, and density.[9,24] To meet the ever increasing demand for energy density, it is essential to maximize the utilization of the full capacity of layered oxide. One approach is to raise the upper cut-off voltage to realize deeper cycling. For example, Ni-rich lithium nickel manganese cobalt oxides was charged to 4.5 and 4.6 V to deliver >220 mAh g^{-1} capacity.[25,26] However, cycling in a wider voltage range raises instability issues due to electrolyte oxidation and lattice structural change.[27] On the electrode level, increasing the active material loading leads to higher cell level energy density but sacrifices the rate capabilities.[28,29]

Another approach to raise the energy density is to improve the first cycle reversibility. It is well known that the first cycle coulombic efficiency of NMC materials is typically around 85%-90%.[30–32] Several studies have been devoted to studying the low first cycle coulombic efficiency. Applying a 24-hour 3 V constant voltage hold at the end of discharge of a $LiNi_{1/3}Co_{1/3}Mn_{1/3}O_2$ (NMC333) cell has been found to recover a large fraction of its first cycle capacity loss, indicating it is likely a kinetic issue.[33] A similar study on the $LiNi_{0.8}Co_{0.1}Mn_{0.1}O_2$ (NMC811) further illustrated the factors influencing the 1st cycle capacity loss, and realized 94.8% initial coulombic efficiency by raising the battery operating temperature to 45 °C.[34] A later study used nuclear magnetic resonance (NMR) to reveal the correlation between the slow Li ion diffusion and the capacity loss.[35] A recent report proposed a reinvented diffusion measurement approach, to

carefully investigate the influence of substituents and particle size on the low-potential region of layered transition metal oxide.[36] Those results indicate that the kinetic barrier is likely the reason for the low initial coulombic efficiency.

Although previous reports have studied this issue from different perspectives, less attention has been paid to the evolution of the 1st cycle capacity loss as a function of depth of charge. By limiting the cycling depth, the formation of cathode electrolyte interface (CEI) can be avoided due to the lower end of charge potential, excluding any potential complications. On the other hand, determination of the onset depth of charge for irreversible capacity formation will help further elucidate the nature of the phenomenon. As far as the root-cause of the sluggish kinetics, there is apparently a correlation between slower Li ion diffusion and the 1st cycle capacity loss. However, the exact nature of this slow diffusion kinetics still requires further examination in order to inform strategies to overcome this loss mechanism.

This work adopts several electrochemical characterization methods coupled with operando synchrotron X-ray diffraction (XRD), to further examine the origin and the evolution of the irreversibility. Specifically, we show that the 1st cycle irreversibility is surprisingly fully developed when only 22.6% of Li has been deintercalated from the cathode. Redistribution of the vacancies with a relaxation process under open circuit, directly observed with in-situ synchrotron XRD, leads to a further increase in irreversible capacity. These new data conclusively establish that the sluggish lithium-ion diffusion near the end of discharge is the reason for most of the irreversibility and the distribution of vacancies in the lattice correlate with the diffusion kinetics. We believe that the in-depth analysis provided in this work will help researchers to develop new methods to reduce the cathode irreversibility.

2.2 Experimental section

Electrochemical test

Electrodes were prepared by mixing NMC811 (Targray), SuperP, and PVDF at weight ratio of 96: 2: 2 in N-methyl pyrrolidinone (NMP) solvent and cast on Al foil. After casting, the electrode was transferred to a vacuum oven, drying at 120 °C. The electrode was punched into 12 mm disks, and then calendered to 30% porosity. The cathode areal loading is around 5 mg cm-2. 2032 coin cell was assembled with a NMC811 cathode, a Celgard 2501 as the separator, a piece of lithium foil (MTI, 500 μm), and 75 μL electrolyte. The electrolyte is prepared by dissolving 1 M lithium hexafluorophosphate (LiPF6) in a 3:7 weight ratio mixture of ethylene carbonate (EC) and ethyl methyl carbonate (EMC). 2% vinyl carbonate (VC) was added as electrolyte additive. The electrochemical tests were carried out on an Arbin battery cycler. Galvanostatic charge/discharge was conducted with different upper cutoff conditions and 2.8 V as the lower cutoff. The current was set as C/10 (1C = 210 mAh g-1). GITT tests were performed by applying one-hour constant current pulse at C/100 rate, followed by 10 hours relaxation, using BioLogic VSP 300 potentiostat. The same processes repeated until the cutoff conditions (4.4 V or 2.8 V) reached. The diffusion coefficient was calculated by the following equation:

$$D = \frac{4r^2}{\pi\tau}\left(\frac{\Delta E_s}{\Delta E_t}\right)^2$$

Where r is the particle size of the cathode material, ΔEs is change of the steady state voltage of the cell before and after a current pulse, ΔEt is the voltage change during the pulse excluding the IR drop.

The electrochemical impedance spectroscopy (EIS) was performed using an AC signal with 10 mV amplitude, with the frequency ranging from 7 MHz to 10 mHz. The Nyquist plots

were fitted to obtain the Warburg impedance. Diffusion coefficient was calculated using the following equation:

$$D = \left(\frac{RT}{\sqrt{2}AF^2R_w}\right)^2$$

Where D is the diffusion coefficient, R is the gas constant, A is the electrode area, F is the faraday constant, Rw is the Warburg impedance.

Characterization

Scanning electron microscopy (SEM) was performed on the FEI Quanta 250 SEM.

Synchrotron X-ray diffraction

High resolution synchrotron powder diffraction data were collected using beamline 11-BM at the Advanced Photon Source (APS), Argonne National Laboratory using an average wavelength of 0.458170 Å. Discrete detectors covering an angular range from 0.5 to 50 degrees 2□ were scanned over a 50 degrees 2□ range, with data points collected every 0.001-degree 2□ and scan speed of 0.01 degree/s.

Operando powder diffraction data were collected using beamline 11-ID-B at the APS, Argonne National Laboratory using an average wavelength of 0.2113 Å on a Perkin Elmer amorphous silicon-based detector (2048 x 2048 pixel with 200 µm size) using a 250 µm x 250 µm beam size and a 0.1s subframe time with a total acquisition time of 1 s per data point. NMC 811 paired with lithium metal were used for the operando studies. The electrodes were assembled in the AMPIX cell in an argon-filled glove box at the APS, using the standard assembling procedure. A MACCOR 4300 cycler was used to control the current or potential across the cells. The powder diffraction data were collected every six minutes for each sample during cycling.

The collected 2D images were converted into 1D pattern using GSAS-II and the sample to detector distance was calibrated using CeO2 standard. Modeling of diffraction patterns was carried out using the TOPAS software (version 6, Bruker AXS). Rietveld refinements were used to determine parameters of interests, including lattice parameters, crystallite size and strain, scale factor, site occupancies, and anti-site defect concentrations for NMCs.

2.3 Results and discussions

To avoid the CEI formation and elucidate the evolution of the 1st cycle irreversibility, we studied the capacity loss with reduced charging depth. As shown in Figure 2.1a, five cells were charged with different cutoff capacities of 240, 105, 63, 31.5, and 10.5 mAh g^{-1}, respectively. In all five conditions, the constant current steps show irreversible capacity. Similar to previous work,[33] a 2.8 V constant voltage hold was applied at the end of the discharge, which recovered most of the initial irreversibility. For example, in the case of a charging capacity of 240 mAh g^{-1}, the total irreversible capacity at the end of constant current step is 28.4 mAh g^{-1}, while the CV step recovers 21.4 mAh g^{-1}, accounting for 75% of the irreversibility. This observation agrees with previous report, indicating the irreversibility is largely a kinetic issue. To visualize the irreversibility evolution, the capacity loss is plotted against the charge capacity in Figure 2.1b, where the first cycle loss is divided into reversible and irreversible loss based on whether it is recoverable by the constant voltage hold step. Surprisingly, we find that the two types of capacity loss are fully developed when the cell is cycled to only 63 mAh g^{-1} capacity or with 23% of Li removed. The reversible and irreversible loss stabilize at around 23 mAh g^{-1} and 7 mAh g^{-1}, respectively. We note that the voltage at the end of charging is only 3.7 V, when 0.23 Li is removed

from the cathode. This implies that the capacity loss mechanism does not involve any significant electrolyte decomposition, because 3.7 V is far away from the carbonate oxidation potential.[37] The irreversible loss, which was previously attributed to parasitic reactions[33], is likely still a kinetic issue as it appears in the low potential region. By excluding the parasitic reaction, we conclude that the sluggish kinetic when the Li occupancy approaching 100% is the reason for the 1st cycle capacity loss.

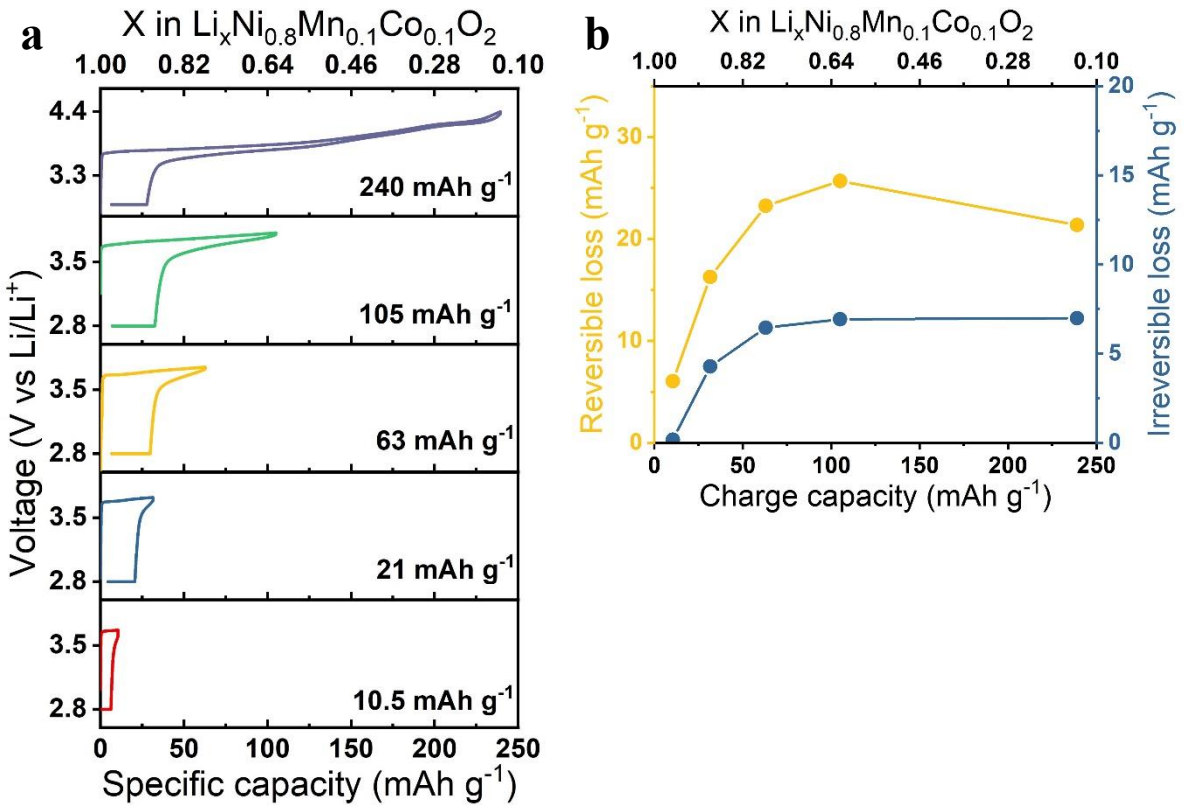

Figure 2.1 1st cycle irreversibility evolution as a function of charging depth. a) Voltage profiles of NMC 811 cycling with different upper cutoff (10.5, 21, 63, 105 and 240 mAh g^{-1}) and constant current discharge followed by a 24-hour constant voltage discharge at 2.8 V. b) Summarization of the reversible (capacity recovered from the constant voltage discharge) and irreversible loss (capacity difference between charge and discharge, including constant current and constant voltage discharge) versus charge capacity and lithium content.

Previous report has already shown correlations between the slow ion diffusion and the 1st cycle loss, by measuring the Li ion diffusivity using GITT.[34] Significantly slower ion diffusion was

observed, while improving the electronic conductivity did not improve the reversibility. These are confirmed by our own measurements. (Figure 2.2)

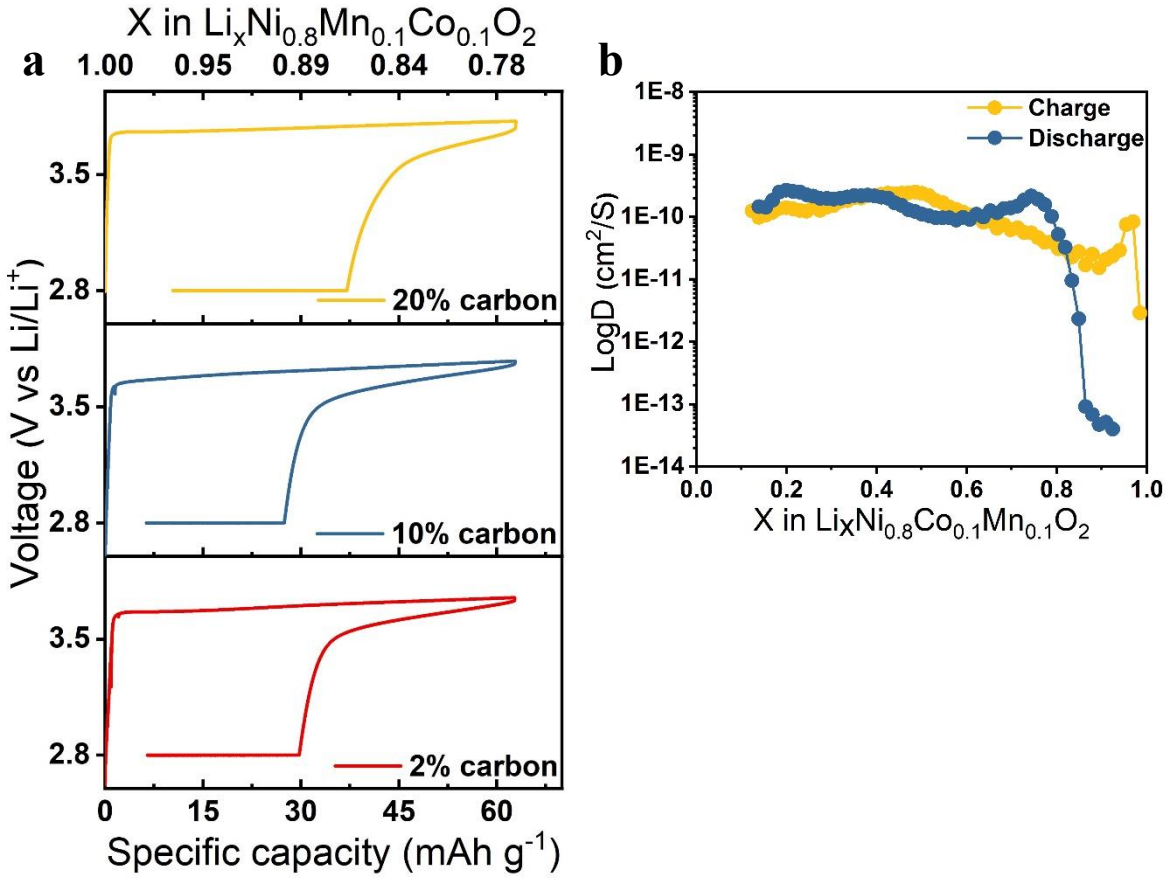

Figure 2.2 Correlation between electronic and ionic conductivity and 1st cycle irreversibility. a) 63 mAh g-1 limited capacity cycling voltage profiles of NMC811 electrode with different amount of carbon. b) Solid-state diffusion coefficient of NMC811 determined by 1st cycle GITT.

To examine other possible reasons, e. g. the charge transfer kinetics, cells with different electrolytes, i. e. 1 M $LiPF_6$ in dimethyl carbonate, $LiPF_6$/LiTFSI dual salts in dimethyl carbonate, and 1.8 M LiFSI in diethyl ether/ Bis(2,2,2-trifluoroethyl) ether (LDEE), were cycled to 63 mAh g^{-1} capacity, as shown in Figure 2.3. We chose a charge capacity of 63 mAh g^{-1} because it was shown that the capacity loss was fully developed at this stage. On the choice of electrolytes, a report has shown that the interfacial charge transfer in the dual-salt electrolyte is significantly faster than that in the single salt electrolyte.[38] The LDEE electrolyte has a contact ion pair (CIP)

solvation structure, which will result in a faster desolvation process and lower charge transfer resistance.[16] The similar electrochemical performance in different electrolytes implies that charge transfer is not a significant factor in the initial cycle capacity loss. In addition to the charge transfer effects, we also compared the performance of a single crystal and a polycrystal material (Figure 2.4). The polycrystal particles have a hierarchical meatball structure, i. e. submicron primary particles aggregate to form 10-20 μm secondary particles, while the single crystal NMC materials are composed of 2-3 μm individual particles. Despite the size difference between primary particles, there is no significant reversibility difference. This implies that the diffusion is not only limited by the primary particle size but also the grain boundaries, if the solid-state ion diffusion limitation hypothesis is true.

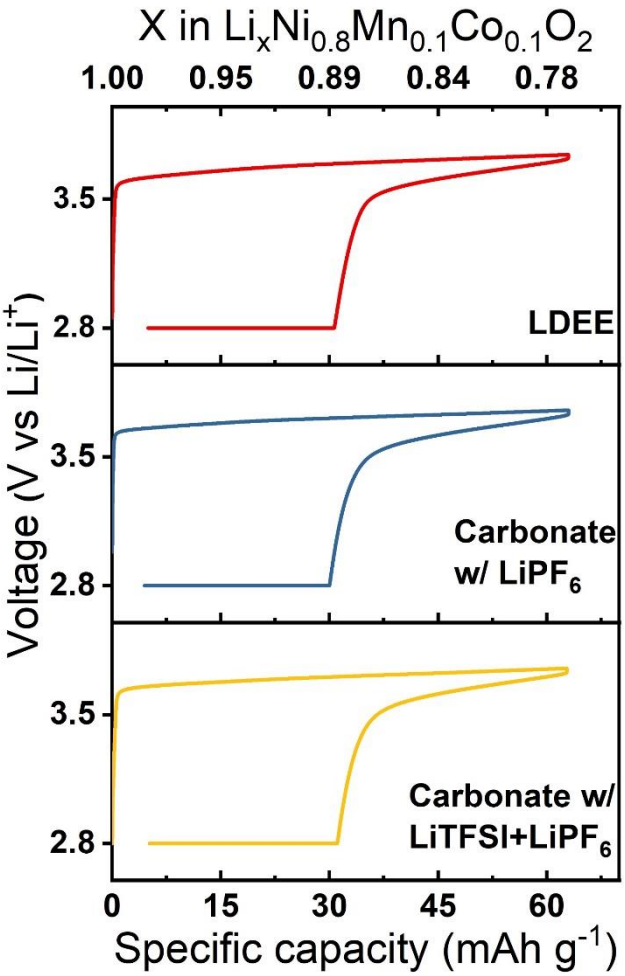

Figure 2.3. Effects of electrolyte composition on the 1st cycle irreversibility. 63 mAh g^{-1} limited capacity cycling voltage profiles of NMC811 electrode with different electrolytes.

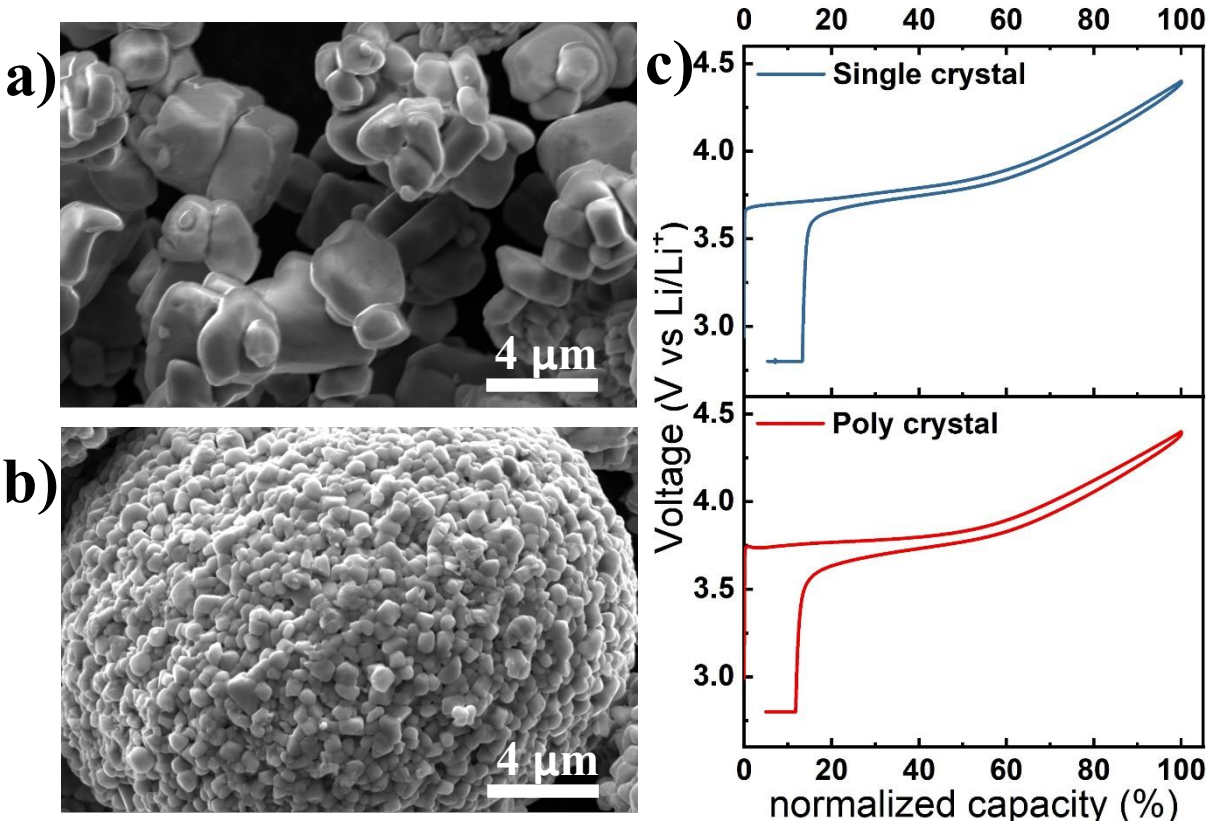

Figure 2.4 The 1st cycle irreversibility of single crystal and polycrystal NMC532. SEM image of a) single and b) polycrystal NMC532. c) 1st cycle voltage profile of single crystal and polycrystal NMC532 electrode.

We further investigated the particle size effect by breaking the hierarchical meatball structure, which reduces the particle size. As shown in the SEM images in Figure 2.5a and b, upon ball milling, the particle size was reduced from tens of micron meters to submicron level. To examine whether the material has been damaged during ball milling, synchrotron X-ray diffraction was conducted on both the pristine and ball milled samples. The result imply that additional defects were introduced during balling. The reversibility of the material within the low voltage range was tested, as shown in Figure 2.5c. The ball milled material delivers 40% more capacity when discharged to 2.8 V. The reversible capacity loss decreases by 7.5 mAh g^{-1}, while the irreversible loss disappears. The above results show that the 1st cycle capacity loss can be tuned by a synergistic

effect of defects introduction and particle size reduction, which is another evidence for the diffusion limitation argument for the commonly observed 1st cycle irreversibility.

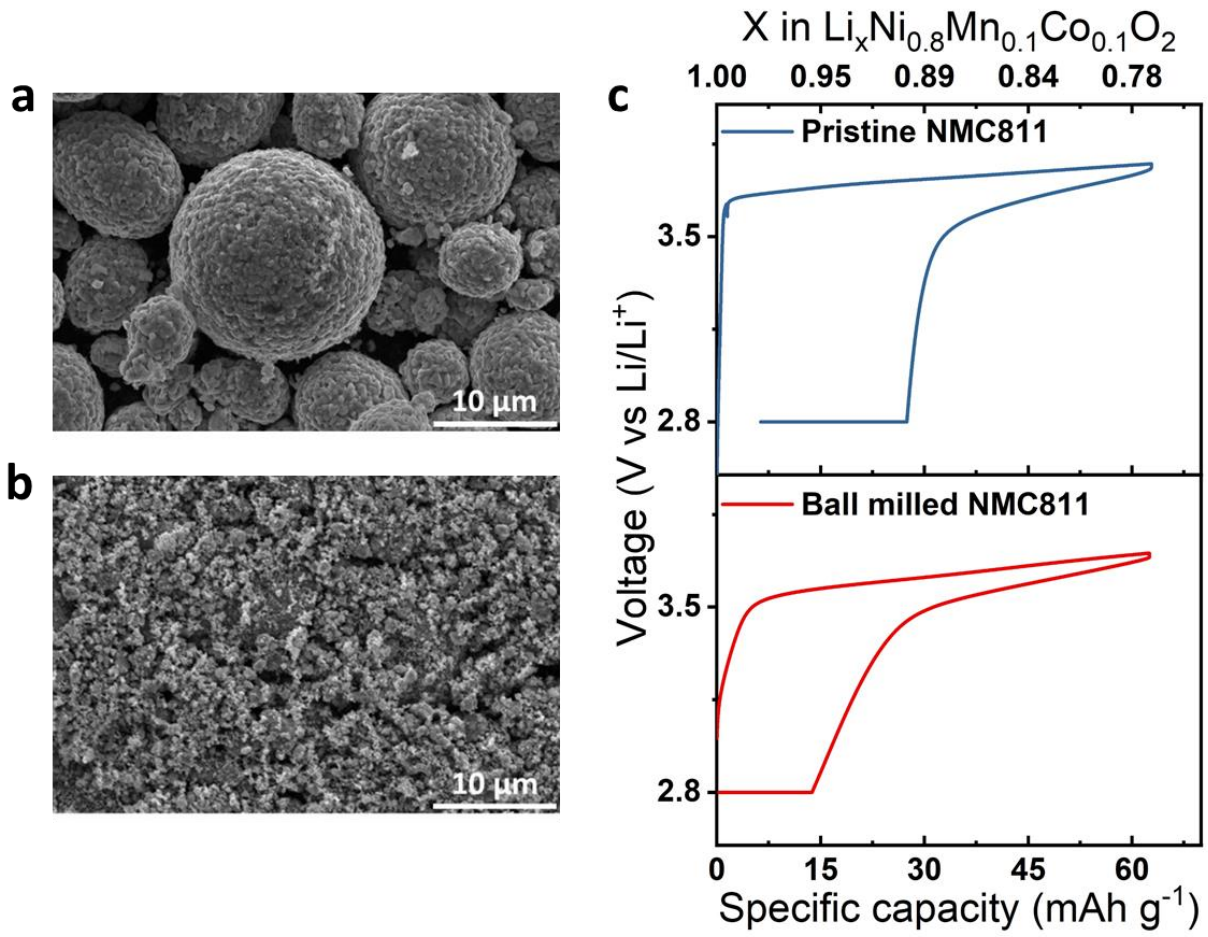

Figure 2.5 Effects of particle size on the 1st cycle irreversibility. SEM images of a) pristine NMC811 particle, b) ball milled NMC811 particle. c) Voltage profiles of 63 mAh g^{-1} cycling of pristine and ball milled NMC811.

According to the model proposed by Van Der Ven et al, the dominant Li diffusion pathway is hopping through the tetrahedral sites, which requires the presence of divacancies.[39] This diffusion mechanism significantly increases the dependence of diffusion rate on the vacancy concentration and distribution, particularly when the Li occupancy approaches saturation. To further confirm this theorem, we performed a relaxation experiment with the results shown in

Figure 2.6a. An electrode was charged to a capacity of 31.5 mAh g^{-1}. The electrode was then discharged immediately or was allowed to relax under open circuit for 24 hours before discharging. The capacity delivered by the constant current discharge step is 80% lower after relaxation than an immediate discharge. We hypothesize that there is a Li vacancy gradient in the cathode particle at the end of charge. The Li vacancy concentration at the surface should be higher than that in the center, since the deintercalation starts from the surface. The vacancy gradient formed during charging facilitates faster Li ion diffusion, which renders higher reversibility. However, the relaxation allows the redistribution of Li ions in the NMC811 particle, which reduces the vacancy gradient, as illustrated in Figure 2.6b. Fewer vacancies on the surface after the rest leads to lower diffusivity and consequently less reversibility. The relaxation effect is particularly pronounced at low degree of delithiation. It is worth noting that one will not observe such a phenomenon if the cell is relaxed at a high SoC, since the overall Li vacancy concentration after relaxation is still high enough for fast Li hopping. The relaxation effect was also examined with 10.5 mAh g^{-1} and 63 mAh g^{-1} cycling, as shown in Figure 2.7 and 2.8. In both cases, relaxation effectively reduced the constant current discharge capacity, which further proves our hypothesis about the vacancy redistribution. A series of electrochemical impedance spectroscopy tests were conducted during the relaxation period, to study the diffusion coefficient change. The data presented in Figure 2.6c and Figure 2.7b show that the diffusion coefficient decreased by an order of magnitude during relaxation in the 31.5 mAh g^{-1} and 10.5 mAh g^{-1} cycling, respectively. Furthermore, once the intercalation starts, the Li ion will accumulate at the surface layer due to limited diffusivity, which will further reduce the diffusion rate.

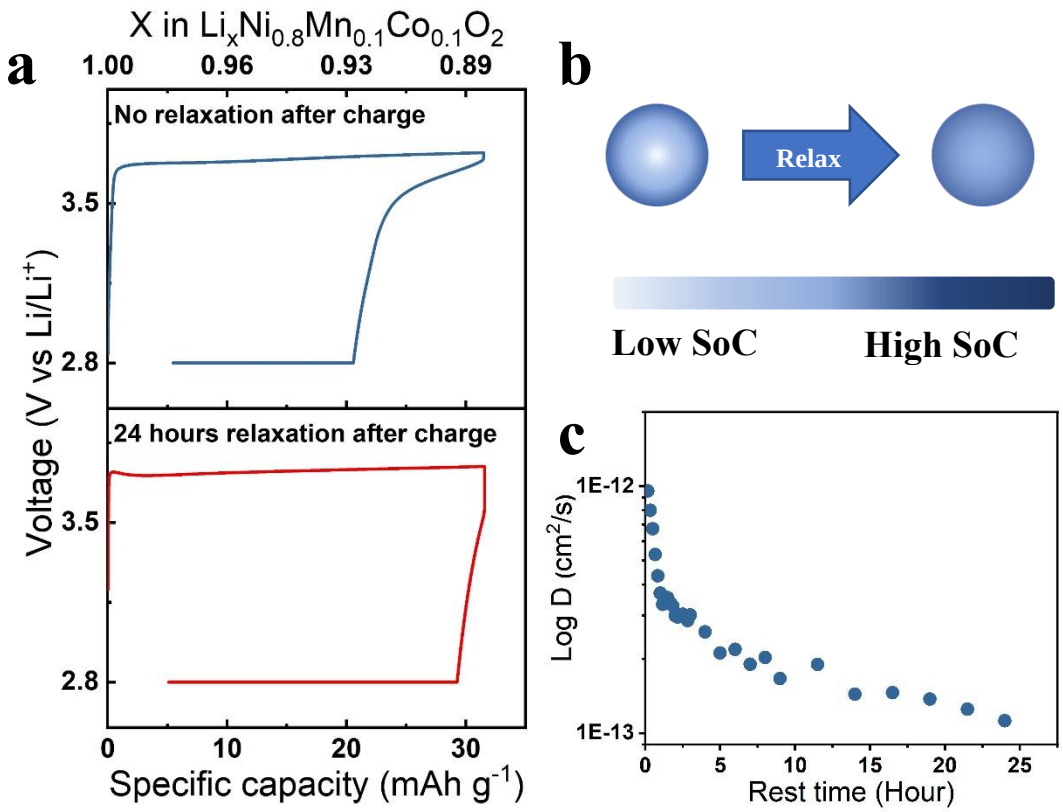

Figure 2.6 Effects of relaxation on the 1st cycle irreversibility. a) Voltage profiles of 31.5 mAh g^{-1} cycling with and without a 24-hour relaxation between charge and discharge. b) Diffusion coefficient of relaxing NMC811 after 31.5 mAh g^{-1} determined by electrochemical impedance spectroscopy. c) schematic illustration of the Li redistribution process during relaxation.

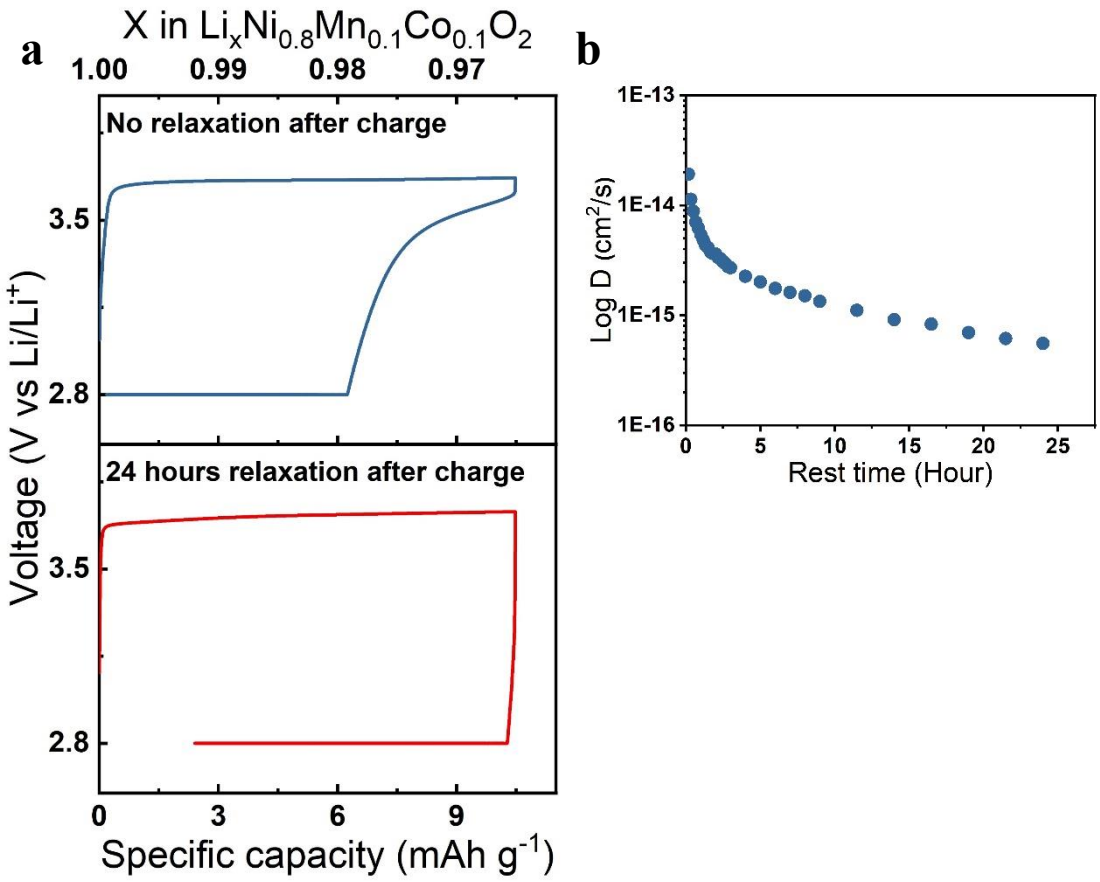

Figure 2.7. a) Voltage profiles of 10.5 mAh g^{-1} cycling with and without 24 hours relaxation between charge and discharge. b) Diffusion coefficient of relaxing NMC811 after charge.

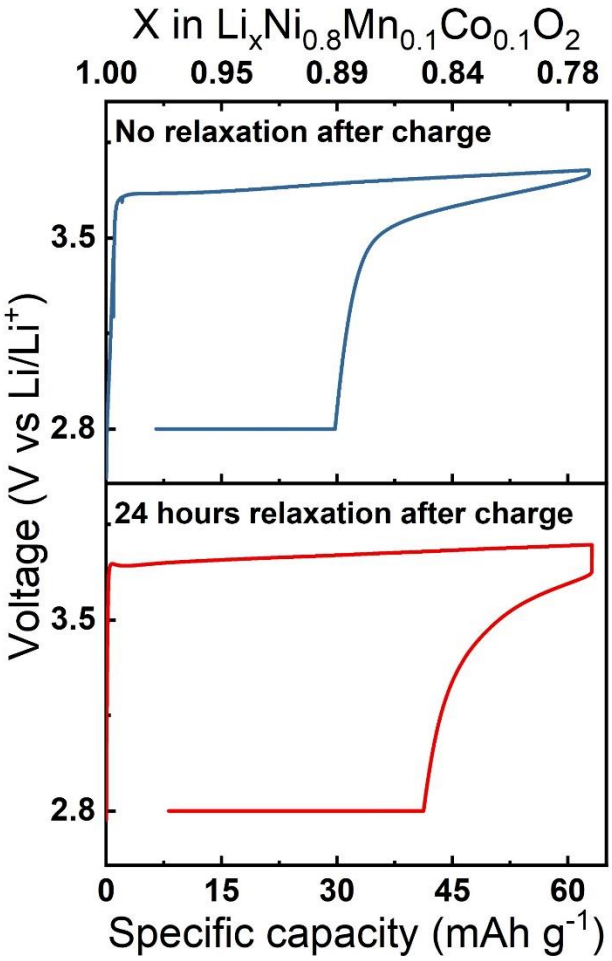

Figure 2.8. a) Voltage profiles of 63 mAh g^{-1} cycling with and without 24 hours relaxation between charge and discharge. b) Diffusion coefficient of relaxing NMC811 after charge.

Operando XRD was used to further investigate the crystallographic evolution during cycling and rest (Figure 2.9a and d). Rietveld refinement was used to investigate the change in lattice parameters and anti-site defects. Although a single NMC phase could model the pristine and discharged samples, it failed to model the charged samples. In this case, A range of NMC phases from 100% SOC to 40% with 5% difference were used to describe the distribution. Microstructures (crystal size and strain), lithium concentration, and anti-site defect were globally

refined and shared between those phases assuming NMC particles at all SOC having the same chemical/physical environments.

Contribution of NMC phases at different SOC were extracted (Figure 2.9b and e) for samples with/without relaxation, and the standard deviation of SOC distribution were plotted for both (Figure 2.9c and f). An increase of inhomogeneity was observed during charge that a small portion of NMC (less than 20%) respond faster than the bulk. Surprisingly, 40% SOC was reached for the fast response portion while the bulk was at a much lower SOC. The slow diffusion of of Li in NMC lattice is the origin of this phenomenon. The outer region of the NMC particles, either the secondary or the primary, was delithiated firstly at the beginning of charging associated, while the Li ion diffusion from the inner particle is not fast enough to replenish it.

This inhomogeneity was eliminated by either discharge or relaxation while the time needed is different. Basically, a reverse behavior could be seen during discharge that a sharp lithiation was observed for the "outer region" while a slow lithiation was observed for the bulk due to the difference between diffusivity and diffusion length. On the other hand, a slow re-distribution was observed during relaxation that the bulk and the fast response region were merging toward the averaged SOC during relaxation. After 24 hrs of relaxation the concentration gradient was uniformized indicated by the narrow distribution and the highest σ.

The difference between relaxed and non-relaxed samples suggests that the lithium diffusion kinetic is the main limiting factor for the 1st cycle CE lost. Without relaxation, a "vacancy rich" region was formed during charge with a high divacancy concentration. Fast lithium diffusion was enabled with the present of this "vacancy rich" region until high SOC was obtained during charge. On the other hand, the "vacancy rich" region disappears after relaxation and thus the surface divacancy concentration is in the similar level with the discharged sample. In this case, as seen in

the e-chem data, little capacity could be extracted during the constant current process. During holding, for both cases, lithium ion was intercalated into the lattice with only monovacancy presents.

The above-mentioned observation confirmed our hypothesis that a steep Li vacancy gradient formed during shallow charge, facilitating faster Li re-intercalation.

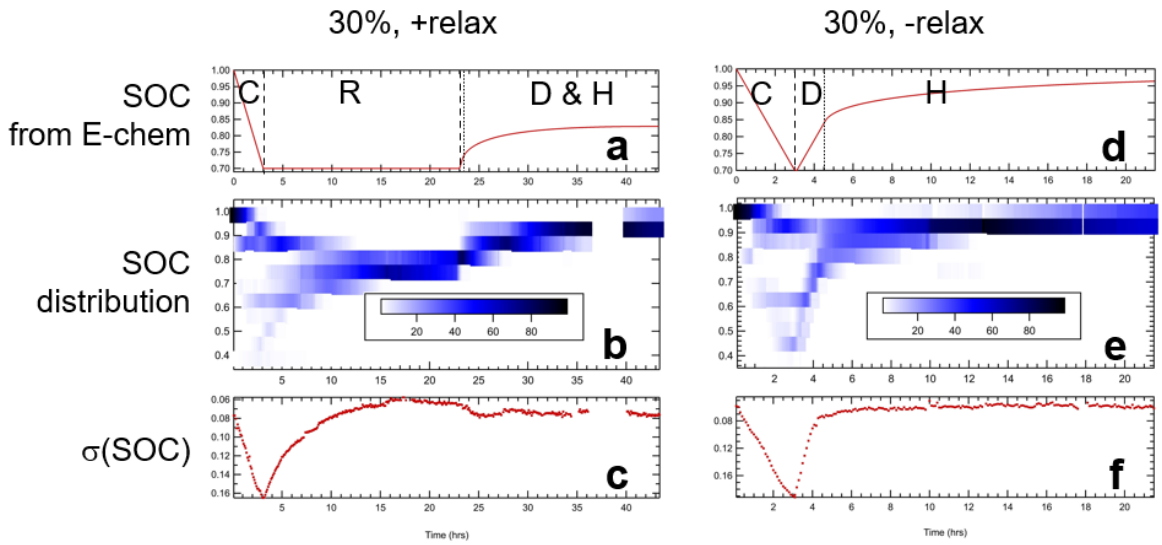

Figure 2.9. Electrochemical and crystallographic data of cell with and without relaxation. a and d, voltage profiles of NMC811 cells with and without relaxation. b and e, SoC distribution of cells with and without relaxation. c and f, standard deviation of the SoC distribution of cells with and without relaxation.

2.4 conclusion

In conclusion, shallow charging combined with the constant voltage discharge experiment have been employed to study the 1st cycle capacity loss evolution, without the complexity of CEI formation at high voltage. Our results show that the 1st cycle capacity loss of NMC is a kinetic issue developed at an early stage, where only 0.23 Li is deintercalated. Ball milling significantly improves the reversibility by reducing particle size and introducing defects, indicating that the ion

diffusion might be the limiting factor of the 1st cycle reversibility. In addition to the positive effect from the ball milling experiment, a negative effect on the initial efficiency is observed in a relaxation experiment. A 24-hour rest applied right after the shallow charge reduces the reversible capacity by 80%. Operando X-ray diffraction confirms a redistribution of the Li vacancy during the relaxation, which results in diffusivity reduction evidenced by EIS measurement. Combining the ball milling and relaxation experiment, direct causality is established between the slow ion diffusion and 1st cycle capacity loss. This work provides in-depth analysis on the origin of the 1st cycle capacity loss, which will help the community to overcome this issue.

Acknowledgements

Chapter 2, in full is currently being prepared for submission for publication of the material, **Zhaohui Wu**, Zhuo Li, Haodong Liu, Peter Khalifah, Ping Liu. The dissertation author was the primary researcher and author of this material.

CHAPTER 3 UNDERSTANDING THE ROLES OF ELECTRODE/ELECTROLYTE INTERFACE FOR ENABLING STABLE LI||SPAN BATTERIES

3.1 Introduction

The demands for low cost and high energy density rechargeable batteries for both transportation and large-scale stationary energy storage encourage research to move to "beyond lithium-ion" battery systems such as metal-sulfur, metal-air, and multivalent batteries.[6,11,40–43] Since sulfur is a low-cost and abundant material with high theoretical capacity, lithium-sulfur (Li-S) battery chemistry has attracted significant interest during the past decade. The sulfur electrode in Li-S batteries undergo multiple electron transfer processes associated with long- and short-chain polysulfide (Li_2S_x) intermediates. It is well known that the long-chain polysulfides can dissolve into electrolytes with aprotic organic solvents and migrate to the Li anode side. This so-called "shuttle effect" is considered the main reason for the capacity loss and low coulombic efficiency of the Li-S system.[44,45]

Many efforts have been made to overcome the problem of polysulfide dissolution through advances of sulfur-based materials[46–48] and electrolytes [49,50] as well as cell engineering.[51] Sulfurized polyacrylonitrile (SPAN) is a promising material due to the physical confinement of the small molecular sulfur in the conductive polymer network, capable of mitigating polysulfide shuttling.[52] Carbonate electrolytes are widely employed for the Li||SPAN battery, exhibiting excellent chemical compatibility with the SPAN cathode.[14,53,54] However, the use of carbonate electrolytes results in poor cycling stability of the Li metal anode.[55,56] On the other hand, ether-based electrolytes provide much more stable Li metal anode cycling; the mixed solvent of 1,2-dimethoxyethane (DME) and 1,3-dioxolane (DOL) is employed in most Li metal anode battery

research, including Li-S batteries.[57] However, it has been reported that DME/DOL-based electrolytes cause the dissolution of lithium polysulfides from the SPAN and the resulting polysulfide shuttle effect, effectively negating any benefits offered by SPAN.[58,59] Several attempts have been made to improve the stability of SPAN in ether electrolytes either by increasing the salt/solvent ratio or introducing additives.[52,58,60–63] For example, Xing et al.[60] reported that a crystalline cathode electrolyte interface (CEI) layer composed of LiF and $LiNO_2$ formed by introducing $LiNO_3$ aids in suppressing polysulfide dissolution in a dilute DME/DOL-based electrolyte. These works mainly focused on improving the performance of Li||SPAN cells, with little understanding of the conversion of sulfur in SPAN during the electrochemical cycling process and the roles of the electrode-electrolyte interfaces on retaining the sulfur species in SPAN cathode.

In this report, we investigate the performance and working mechanisms of Li||SPAN batteries in three different electrolytes: 1M LiTFSI in EC/DMC (CarE), 1M LiTFSI in DME/DOL (EE), and 1M LiTFSI and 0.5 M $LiNO_3$ in DME/DOL (ENE) that enable stable cycling of SPAN, Li, and both SPAN and Li, respectively. To probe the fate of the sulfur-containing species in different electrolytes, a spatially-resolved X-ray absorption spectroscopy (XAS) combined with X-ray fluorescence (XRF) microscopy characterization technique is utilized. The morphological changes and the redistribution of sulfur and polysulfide in both the SPAN cathode and lithium metal anode are monitored through the XRF images, while the chemical state changes of the S in SPAN and sulfur-containing interfacial layer are characterized with XAS. Coupled with X-ray photoelectron spectroscopy (XPS) and scanning electron microscopy (SEM), the results in this study provide an in-depth understanding of the reaction processes and the key roles of the CEI and SEI for stabilizing the SPAN and Li electrodes. Besides the enhanced fundamental understandings, the stable cycling of high areal loading SPAN cathode (> 6.5 mAh cm^{-2}) with a lean electrolyte

amount of 3 g Ah^{-1} is successfully demonstrated in the ENE electrolyte with a LiF-rich CEI. In contrast, the Li||SPAN cell using CarE shorted during its 4^{th} cycle. The excellent performance of our Li||SPAN cell paves the way for the development of practical high-energy density Li||SPAN batteries.

3.2 Experimental section

SPAN synthesis

To synthesize SPAN material, elemental sulfur (Alfa Aesar) and polyacrylonitrile (Sigma-Aldrich, Mw = 150,000) in a weight ratio of 4:1 were hand-milled in an agate mortar to ensure homogeneous mixing. The mixture was heated in an argon-filled furnace at 450 ºC for 6 h with a ramp rate of 2 ºC/min, then allowed to cool to room temperature.[35]

Electrochemical characterization

SPAN cathode was prepared with SPAN powder, Super-P, and PVDF at a weight ratio of 70:15:15 mixed in N-methyl pyrrolidinone (NMP) solvent and cast on Al foil. After drying in a vacuum oven at 80 ºC overnight, the electrode was punched into a 12 mm disk. The SPAN cathode loading was around 2.0 mg cm^{-2}. A fixed amount of electrolyte (~66 µL cm^{-2}) is added into each coin cell to guarantee the complete wetting of the separator and electrodes. The electrolyte/SPAN ratio is 33 µL mg^{-1}. The thick SPAN electrode for a lean electrolyte test was made by mixing SPAN, binder, and Super P in a weight ratio of 80: 10: 10. The loading was controlled at around 10 mg cm^{-2}. The 2032 type coin was assembled in an argon-filled glovebox. The cycling performance tests of using excess lithium sources were carried out in different electrolytes

assembled with lithium discs (MTI, 500 μm thickness) and 2501 Celgard separators (Celgard, USA). 1 M LiTFSI in EC/DMC (1:1), 1 M LiTFSI in DME/DOL (1:1) and 1 M LiTFSI in DME/DOL (1:1) with 0.5 M $LiNO_3$ were used as electrolytes. In the lean electrolyte test, the electrolyte/capacity ratio is 3 g Ah^{-1}. The amount of electrolyte was also verified by measuring the weight of the coin cell before and after adding electrolyte. The electrochemical test was carried out on a LAND battery tester (Wuhan, China). Galvanostatic charge/discharge was conducted in a fixed voltage range of 1–3 V vs. Li/Li^+ at room temperature with C/5 (1C = 550 mAh/g) current density based on SPAN weight.

X-ray absorption spectroscopy and fluorescence imaging

X-ray fluorescence microscopy and sulfur K-edge XAS experiments were carried out at beamline 8-BM (TES) of the National Synchrotron Light Source II (NSLS II) at Brookhaven National Laboratory. The sample was prepared in an argon-filled glove box. The cycled electrode collected from the coin cell was washed with DME solvent and dried. The dried electrodes were attached to the Kapton tape (face to backside of electrode, current collector side) and covered with an Mylar film (face to the electrode surface) to avoid air exposure. The XRF/XAS measurement was conducted in the He-filled chamber at the TES beamline, thus air exposure of the sample was minimized in this study. X-ray fluorescence microscopy measurements were performed in a fly scan mode with a 25 μm pixel size. The X-ray energy was set at different energies of 2469, 2475, 2480 eV to obtain the XRF images for different transition states of sulfur species. After XRF imaging, the XAS was measured for selected spots using the same size of micro-beam, 16 um (horizontal) x 5 um (vertical). Depending on the quality of spectra, 15-20 spectra were measured and merged. XANES data were analyzed using the Demeter software package.[45]

X-ray Photoelectron Spectroscopy

X-ray Photoelectron Spectroscopy (XPS) (Physical Electronics, Quantera Scanning XPS Microprobe System) was carried out using Al anode source at 15 kV. Samples were collected at the end of the fifth charge. Obtained data were calibrated based on the reference of C-C bond at 284.6 eV and fitted in CasaXPS.

3.3 Results and discussions

We first compare the electrochemical performance of SPAN in the three different electrolytes (Figure 3.1). The areal capacity of the SPAN electrode is ~ 1 mAh cm^{-2}. The volume of the electrolyte is 75 μL in order to investigate the compatibility between electrolytes and the SPAN material. SPAN shows stable cycling in CarE at C/5 between 1 and 3V, consistent with previous reports.[53] The electrode maintains a reversible capacity of ~ 550 mAh g^{-1} after 100 cycles (Figure 3.1b). However, the SPAN material does not cycle well in the EE electrolyte. There is a long charge plateau at ~ 2.4 V, indicating that the shuttling reaction of Li_2S_n takes place in this ether electrolyte, resulting in active sulfur loss from the SPAN and low coulombic efficiency (Figure 3.1c, Figure 3.2). Within 10 cycles, its capacity decreases from 471 mAh g^{-1} to 309 mAh g^{-1}. With the addition of 0.5 M of $LiNO_3$ to form the ENE electrolyte, the charge plateau related to the polysulfide shuttle is effectively eliminated (Figure 3.1d). The ENE electrolyte shows high coulombic efficiency towards both Li anode (>98%) and SPAN cathode (~100%), as shown in Figure 3.3. Besides the high coulombic efficiency, the cell delivers a capacity of 536 mAh g^{-1} at

its 100th cycle, corresponding to a capacity retention rate of 93.2% (based on the capacity at the 5th cycle).

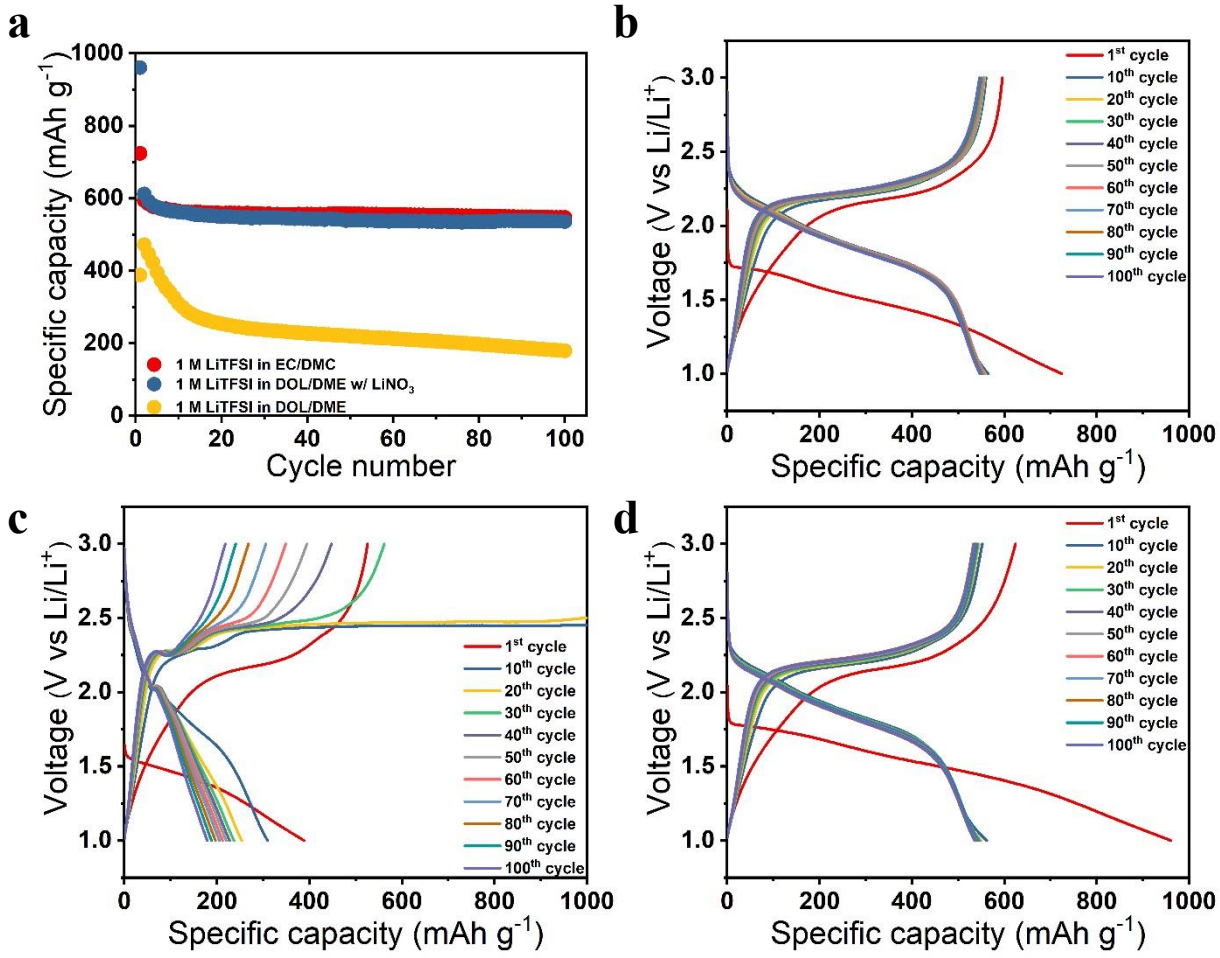

Figure 3.1 Electrochemical performance of SPAN cathode in different electrolytes. (a) Cycling performance of SPAN electrode in 1 M LiTFSI-EC/DMC (red dots, CarE), 1 M LiTFSI-DME/DOL (yellow dots, EE), and 1 M LiTFSI-DME/DOL with 0.5 M $LiNO_3$ (blue dots, ENE). Galvanostatic charge and discharge profiles of Li||SPAN coin-cell throughout 100 cycles using the electrolyte of 1 M LiTFSI in different electrolyte solvents: (b) CarE, (c) EE, and (d) ENE. The cells were cycled at C/5 (1C = 550 mAh g^{-1}).

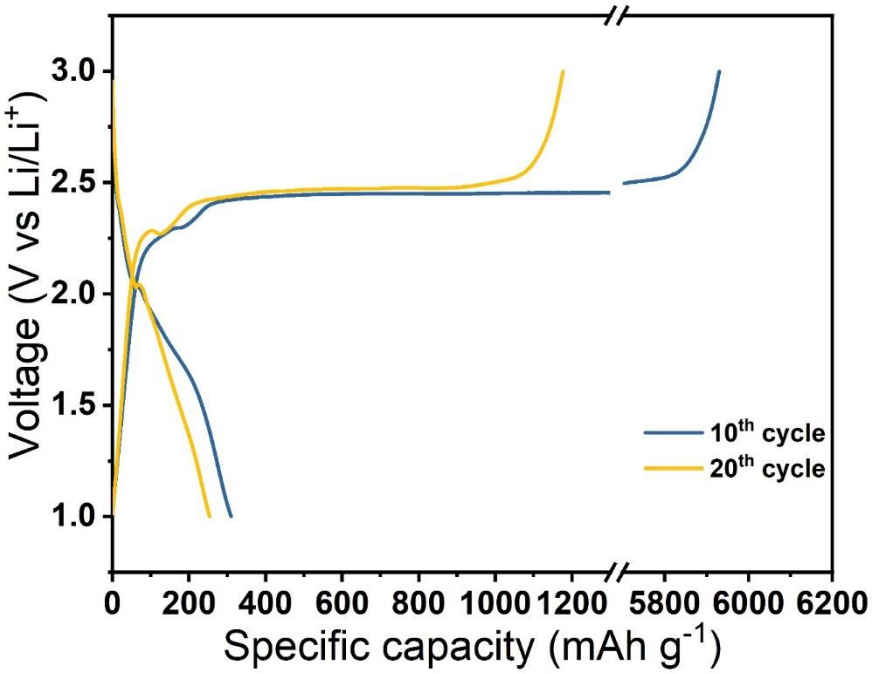

Figure 3.2. 10th and 20th cycle voltage profiles of Li||SPAN cell with EE as electrolyte.

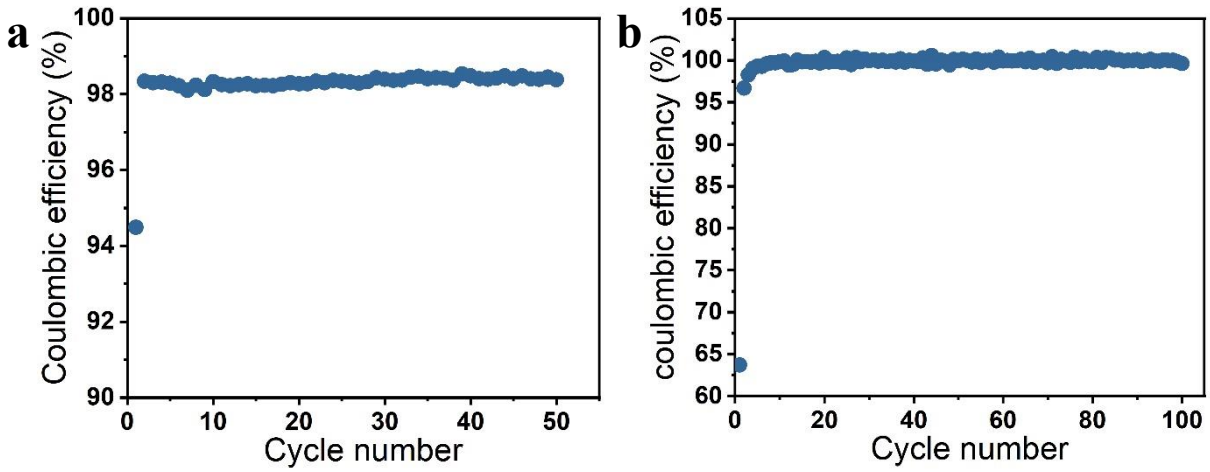

Figure 3.3. a) Li anode efficiency in ENE. b) SPAN cathode efficiency in ENE. Li||Cu cell was cycled under 0.5 mAh cm^{-2} for 1 mAh cm^{-2}.

Evidently, the SPAN performs differently in carbonate and ether-based electrolytes. We hypothesized that the presence of a CEI layer on the SPAN cathode is the key to enabling the stable cycling of SPAN in ENE. X-ray photoelectron spectroscopy (XPS) was conducted on SPAN electrodes after five cycles and in a charged (delithiated) state to examine the compositions of CEI

formed in different electrolytes. The C1s spectra (Figure 3.4a-c**)** show that the O-C=O and C-O peaks dominate the C1s region of SPAN cycled in CarE, likely due to the decomposition of carbonate solvents to form a RCO_3Li rich CEI, where R is an alkyl group.[64,65] In contrast, the decomposition of ether on the SPAN cathode is negligible. Both C-F and LiF peaks are observed in all three cases (Figure 3.4d-f). The C-F bond is attributed to the PVdF binder, while the LiF derived from the LiTFSI salt is the CEI component [66]. The SPAN electrode from the ENE showed a significantly higher LiF concentration in its CEI layer. A LiF-rich CEI on the SPAN electrode surface is believed to prevent polysulfide dissolution[60]. Figure 3.4g-i show the S2p spectra of the cycled SPAN electrodes. Doublets at around 168 eV and 160 eV are assigned to Li_2SO_x and Li_2S, which are observed in all three electrolyte systems[60]. However, the C-S/S-S signals from SPAN are found only on the SPAN electrode cycled in EE [67]. This indicates that polysulfide dissolution takes place in EE due to the lack of LiF-rich CEI as the protective layer, while the RCO_3Li rich CEI in carbonate electrolyte prevents the detection of underlying SPAN structure.

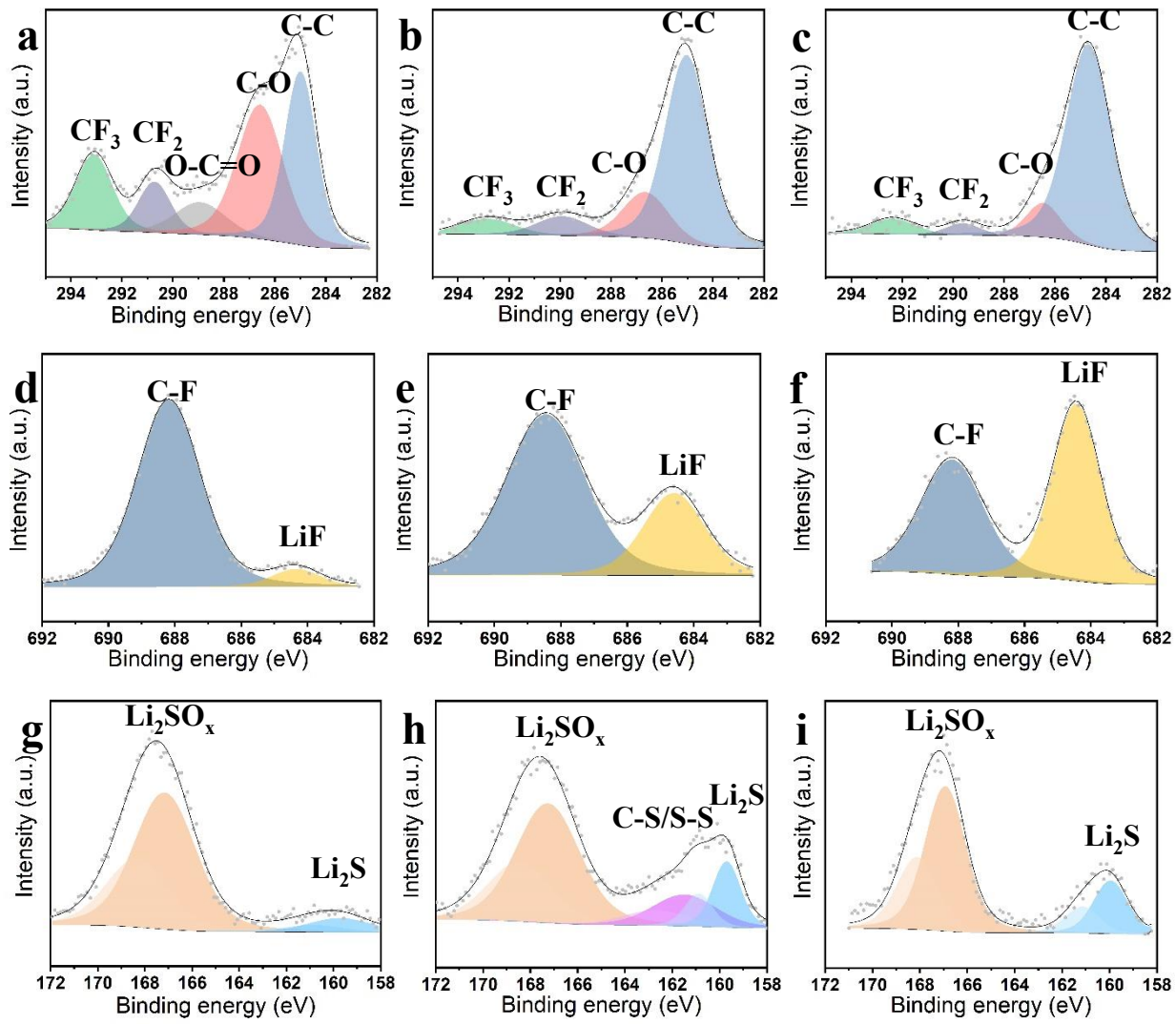

Figure 3.4. XPS of cycled SPAN cathode. C1s spectra in (a) CarE, (b) EE, (c) ENE. F1s spectra (d) CarE, (e) EE, (f) ENE. S2p spectra in (g) CarE, (h) EE, (i) ENE.

To further investigate how the sulfur-based species evolve in the SPAN electrodes, we utilized a combined XRF and S K-edge XAS technique, which not only provides global elemental distribution over the electrode at mm length scale but also probes the spatially resolved chemical information of sulfur-based species using the micro-sized beam. Figure 3.5a shows an XRF image of a pristine SPAN cathode (2 x 4 mm^2 area) measured at an incident X-ray beam energy of 2480 eV. An inhomogeneous distribution of sulfur-based species is observed, as depicted with circles

for high and low S concentration areas in Figure 3.5a. The corresponding XAS spectra of the selected areas are shown in Figure 3.5b. The absorption intensity, so-called 'edge-jump,' indicates the total absorption of sulfur species at the spot where the micro-sized beam (16 um (horizontal) x 5 um (vertical)) shined. For a more detailed investigation of the chemical state, the XAS plot is normalized, as shown in Figure 3.5c. A spectral distortion is observed at the XANES, which should be mainly caused by self-absorption due to the high sulfur concentration for the spectrum collected from the high S area. Except for the spectral distortion, the chemical status of the pristine SPAN cathode is uniform and only has a slight thickness variation that might have been induced by the slurry casting process used for electrode fabrication. Both spectra represent the same three major peaks as indicated: 1 (2468.5 eV), 2 (2470.8 eV), and 3 (2472.5 eV) (Figure 3.5c**)**. These peaks can be attributed to the transition from S 1s to S=C π*, S-S σ*, and S-C σ* states in the SPAN structure, respectively.[68,69] The corresponding bonding structure is displayed with a colored circle over the SPAN structure in Figure 3.5d. The proposed structure in Figure 3.5d is adopted from the previous report by Fanous et al.[70] We note that this model is only one of several structures that have been proposed, [59,71–73] which might be due to the variance of the synthesis route and the resulting complexity of the polymeric structure of SPAN. Although the proposed structures differ in detail, all of them incorporate covalent bonding between sulfur and carbon in the SPAN, instead of the physical absorption of elemental sulfur in carbon. In this study, we use the structure in Figure 3.5d for the following discussions, which is consistent with the observed result from the XAS data.

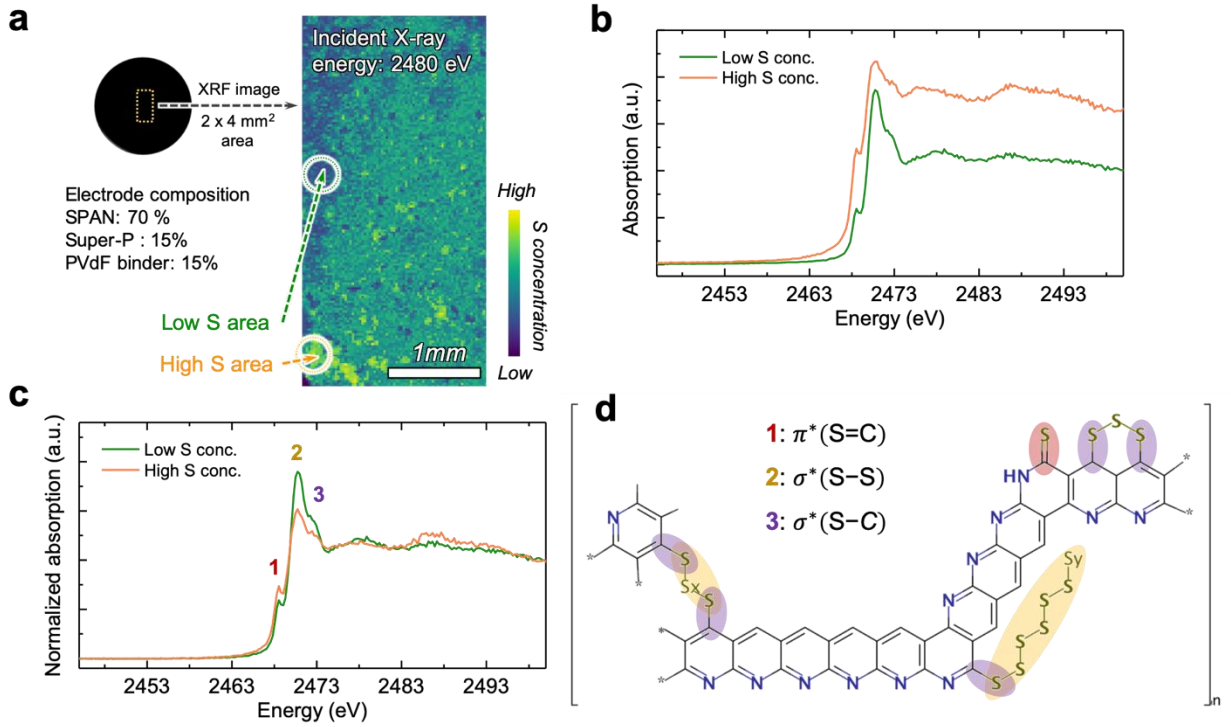

Figure 3.5 XRF and XANES characterization of cycled SPAN. (a) XRF image of pristine SPAN cathode measured at incident X-ray beam energy of 2480 eV with indications of inhomogeneous distribution of sulfur contained chemical species, (b) measured S K-edge μXANES spectra at the selected area for low and high S concentration indicated in XRF image. (c) normalized S K-edge μXANES spectra and (d) model structure of SPAN re-drawn based on the previous report by Fanous et al.[70] All of the red, yellow and purple regions indicating S=C, S-S, and S-C bonds exist in the SPAN in this study.

Figure 3.6a shows the XRF images for SPAN cathodes after five cycles and in a charged (delithiated) state with different electrolytes. XRF images were collected at two different incident X-ray energies of 2469 eV and 2480 eV. The images collected at 2469 eV represent the chemical states of low valence S (e.g., S=C π*, Li_2S_x) only, while the images collected at 2480 eV are used for representing excitations of all sulfur states available below 2480 eV. Interestingly, a lower S concentration area (dark blue color region) is observed for the EE case at the 2469 eV, whereas no noticeable difference is observed at 2480 eV. This indicates that the transition allowed states for the pre-edge region in EE case are diminished, which implies a reduced concentration of S=C π* (or low valence state S such as LiS_x). The corresponding XAS spectra for each selected area are

shown in Figure 3.6b, which contain three distinct peaks featured at around 2469 eV, 2471 eV, and 2478 eV. All the electrodes show a uniform S distribution with almost no variance in each spectrum, while some variations in peak developments are observed in different electrolyte systems.

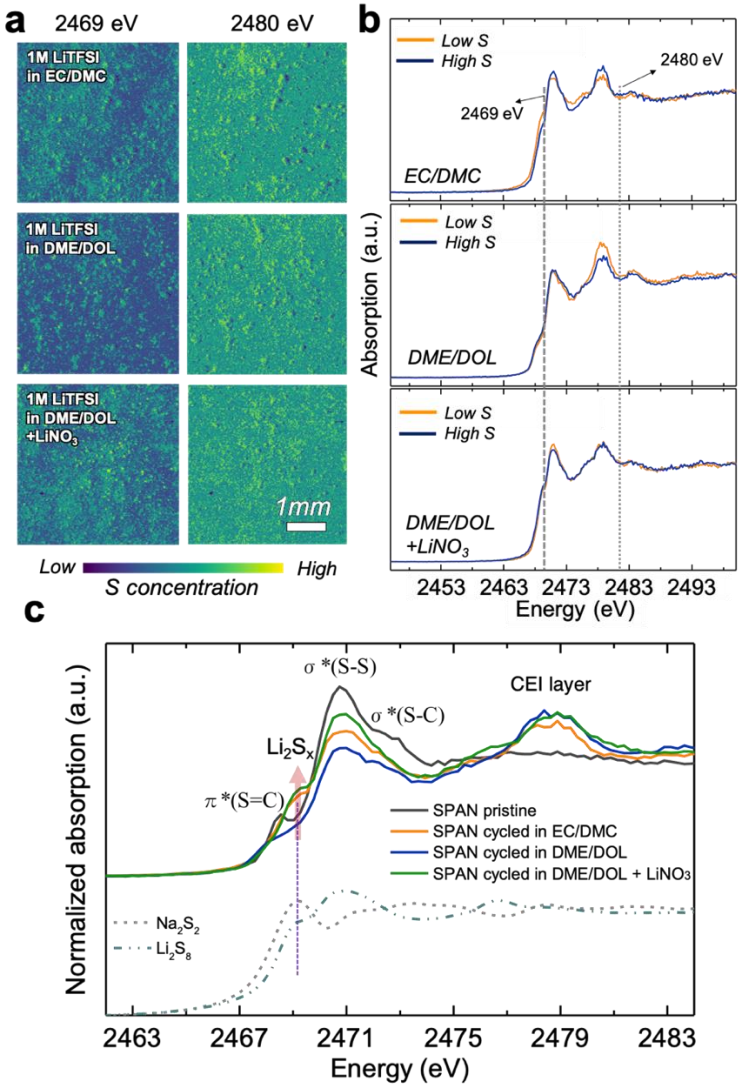

Figure 3.6 Comparison of SPAN electrodes cycled in different electrolytes. (a) XRF image of SPAN cathodes (4 x 4 mm^2 area) cycled in EC/DMC, DME/DOL, DME/DOL with $LiNO_3$, measured with an incident beam energy of 2469 eV and 2480 eV. (b) Corresponding S K-edge XANES spectra were measured at low and high S concentration regions chosen from (a). (c) Normalized S K-edge XANES spectra for comparison with reference spectra of Na_2S_2 and Li_2S_8.[74]

A more detailed analysis of the chemical states can be performed with normalized XAS spectra in Figure 3.6c. By comparing the spectra with that of pristine SPAN, several distinct peak changes could be observed. First, the S=C π* peak of SPAN diminishes in all electrolytes after cycling, which does not fully recover to its initial status, reflecting the irreversible cleavage of the S=C bond. Further investigation on the irreversible cleavage of the S=C was made with the SPAN electrode at a fully discharged state (at 1.0 V vs. Li/Li^+) and fully charged state after the 1^{st} cycle (at 3.0 V vs. Li/Li^+) in EE or ENE. As shown in Figure 3.7a and b, the peak for the S=C bond disappears regardless of CEI composition at the fully discharged state. The S=C bond is only partially recovered during the charging process, which might lead to the irreversible capacity loss during the 1^{st} cycle. Additionally, in contrast to the EE case, a new peak associated with Li_2S_x appeared after 1^{st} charge for the cases of CarE and ENE. Notably, the Li_2S_x peak is enhanced upon cycling in the presence of $LiNO_3$ (Figure 3.7b), indicating the accumulation of Li_2S_x on the SPAN cathode during the cycling. The lack of Li_2S_x for the EE electrolyte implies dissolution of Li_2S_x into the electrolyte rather than being retained in the SPAN cathode.[75] This is a direct evidence of the polysulfides Li_2S_x dissolution that might result in polysulfide shuttling. The shuttling of polysulfide is also confirmed by cross-checking the Li metal surface, which will be discussed later.

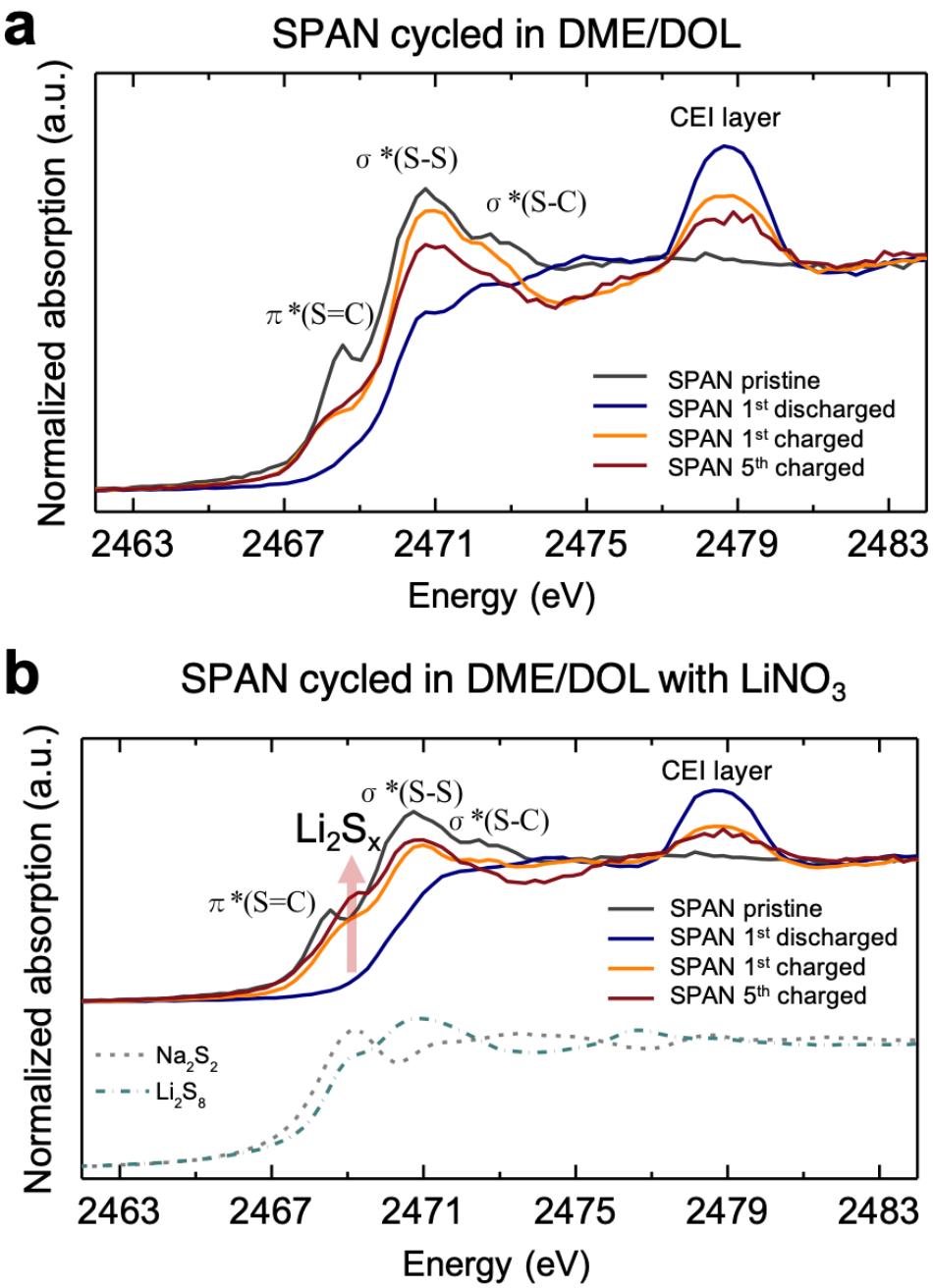

Figure 3.7. Normalized S K-edge XANES for pristine and cycled SPAN cathodes cycled in (a) EE, and (b) ENE.

We next analyze the spectra in Figure 3.6c in the energy range of around 2471 eV where the absorption peak intensities of the S-S bond and S-C bond decrease after 5 cycles. A change of these peaks is associated with radical type SPAN formation with cleavage of the S-S and S-C

bonds in the SPAN structure during the first cycle.[72] A dissolution or loss of sulfur units from the SPAN molecules may also be involved, and it appears as a more considerable decrease of S-S bond in the XANES spectrum for the electrode cycled in EE. Finally, a broad peak with a center at around 2478 eV, which we attribute to the CEI, appears for all the samples. The broad peak for CEI over the wide range of energy is attributed to the transition from the 1s to S-O σ^* state in the oxidized sulfur species such as $-SO_3^{2-}$ (2477eV), $-COSO^{2-}$ (2479 eV), $-SO_4^{2-}$ (2482 eV).[74,76–78]

Investigation of cycled SPAN cathodes from different electrolytes has addressed the following points regarding the structural changes of SPAN and the role of a LiF-rich CEI in the ether electrolyte: 1) the first cycle irreversible reaction is associated with the irreversible cleavage of S=C and S-C bonds in the SPAN structure; 2) lithium polysulfide, Li_2S_x, forms in the cathode after the first full cycle. In EE electrolyte, the decrease of the S-S bond and the Li_2S_x peak reveals that the fast capacity degradation of SPAN in EE is caused by the Li_2S_x dissolution and shuttling; 3) in contrast, the Li_2S_x peak is stable in CarE and ENE due to the formation of a LiF-rich CEI, which explains the stable cycling of SPAN in these two electrolytes. The LiF-rich CEI serves as a protective layer for the SPAN cathode to prevent the Li_2S_x from dissolving into the EE.[72]

In order to probe the effect of electrolytes on the anode, we also collected XRF images and XAS on Li electrode surface. Although the XAS is not a technique capable of directly probing the Li metal due to the low energy characteristic of Li, the sulfur-containing solid electrolyte interface (SEI) layer can be characterized with S K-edge XAS. Moreover, XRF imaging at 2480 eV can visualize the SEI layer that reflects the morphology of lithium metal underneath it. The XRF images for the cycled lithium metal anode in the different electrolytes are shown in Figure 3.8a. Non-uniform and rough shapes of Li deposition are observed for the lithium anode cycled in CarE, while spherical and relatively uniform Li deposition is observed in EE and ENE. A schematic

sketch of a cross-sectional view of lithium metal for each case is shown in Figure 3.8b. Figure 3.8c shows the morphology of lithium after one hundred cycles in CarE and ENE electrolytes. The lithium in CarE developed a mossy appearance, while the lithium in ENE electrolyte deposited as large grains with a relatively regular round shape. The better morphology is typically associated with higher coulombic efficiency of Li anode [22,79–81] because a more compact lithium deposition would result in a more uniform and efficient stripping in the next charging cycle.

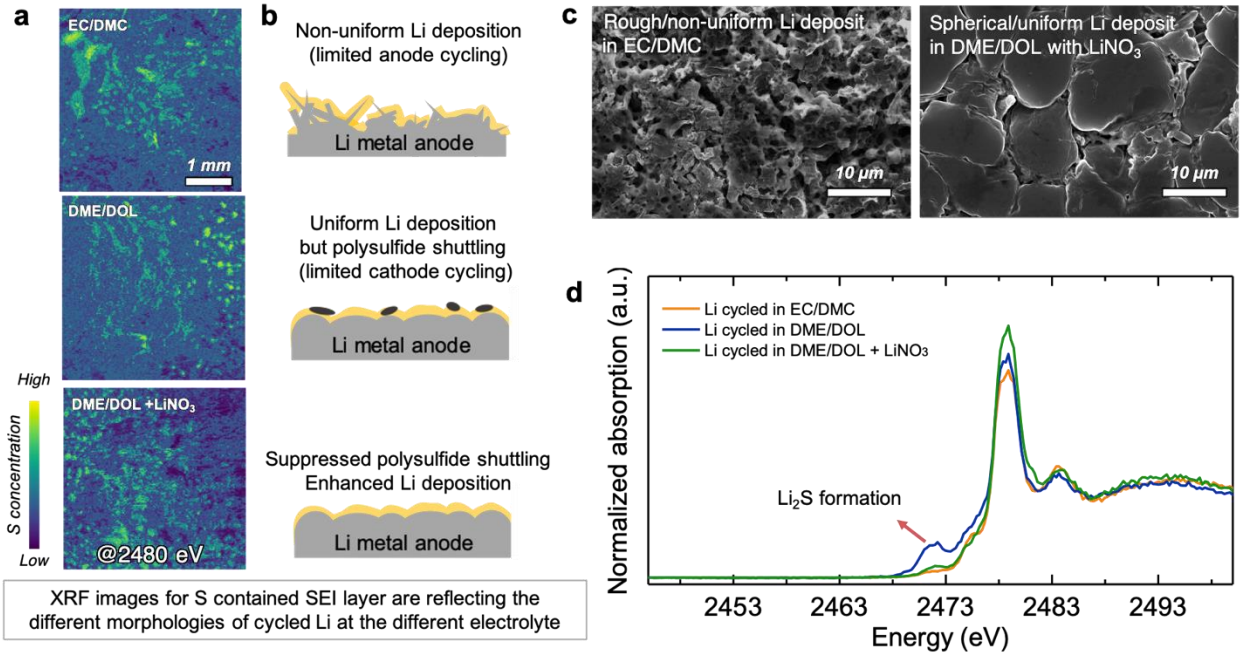

Figure 3.8 XRF and XANES characterization of Li anode cycled in different electrolytes. (a) XRF image of Li metal anodes cycled in CarE, EE, and ENE, measured at an incident beam energy of 2480 eV. (b) Corresponding schematic sketch of a cross-section view of Li metal anode for each case and (c) SEM images for Li metal anode after 100 cycled in CarE and ENE. (d) Normalized S K-XANES measured from the selected area from (a).

The corresponding XAS spectra are plotted in Figure 3.8d. The highest intensity peak at 2479 eV corresponds to the SEI layer, including oxidized sulfur species such as -$COSO_2$, a product of electrolyte decomposition.[77] A small peak of Li_2S appears just below 2473 eV in the case of EE. Li_2S, which is the final product of the conversion of lithiated sulfur, can be formed only

through the shuttling of Li_2S_x from the cathode side. In contrast, the electrode cycled in ENE shows no Li_2S peak. This result confirms that the LiF-rich CEI could effectively suppress the polysulfide shuttle in the EE electrolyte.

The SPAN electrode with an areal capacity of 1 mAh cm^{-2} shows stable cycling in both CarE and ENE. To further elucidate the benefits of ENE electrolyte under a more realistic battery testing condition, we tested a high areal capacity SPAN electrode under lean electrolyte conditions, an important step towards realizing cells with high energy density. As shown in Figure 3.9a, when the electrolyte amount was reduced to 3 g Ah^{-1}, the cell with CarE initially was unable to deliver any capacity due to the poor wettability of EC/DMC. It took 25 cycles to activate the thick SPAN electrode, but its capacity quickly decayed due to the consumption of the electrolyte. We also conducted the same experiment with 1 M LiTFSI-EC/EMC, which shows a significant improvement in wettability. The cell initially delivered a reversible capacity of 6 mAh cm^{-2}. However, it suffered from soft shorting at the 4^{th} cycle, as indicated by the fluctuating voltage profile in Figure 3.9c.

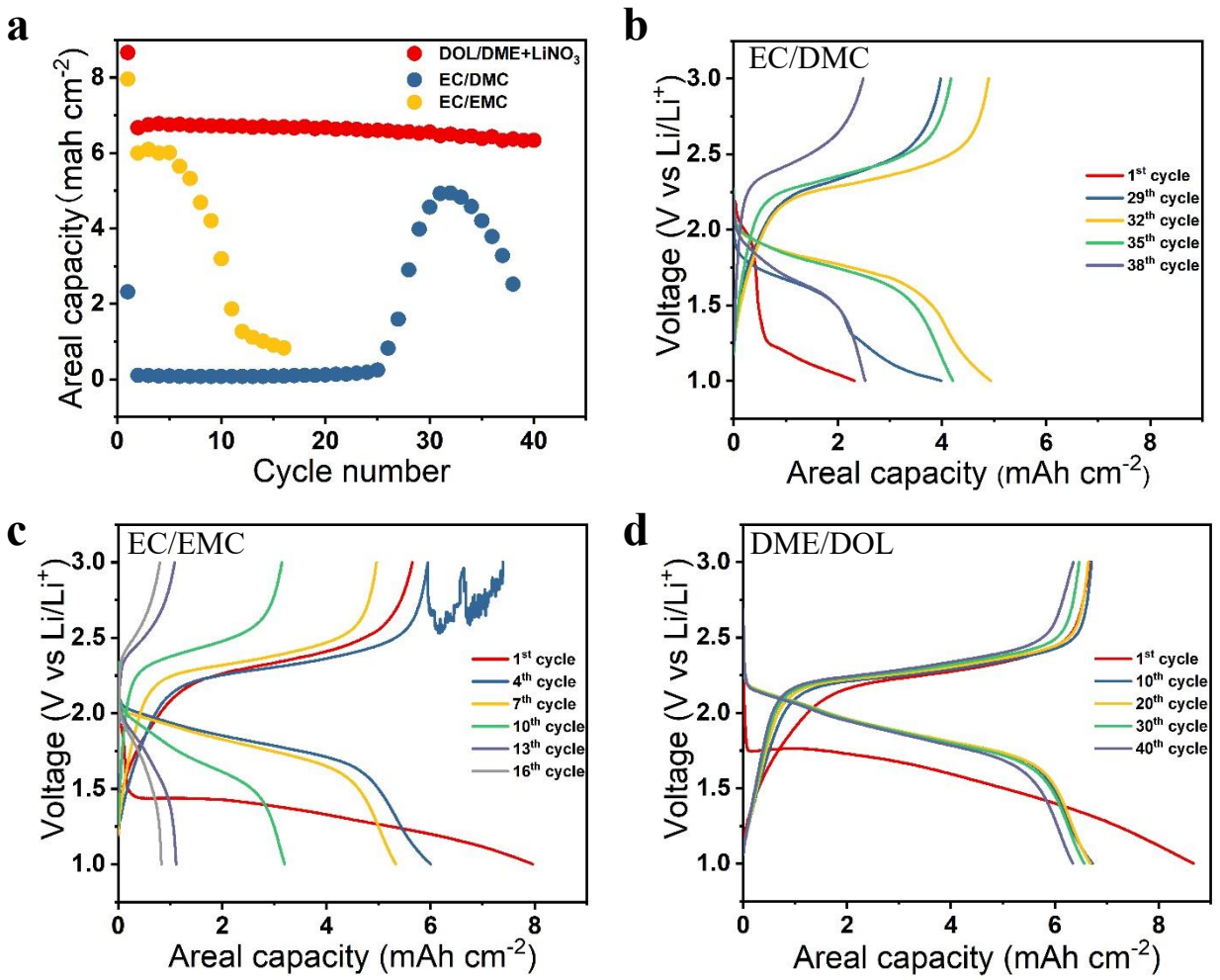

Figure 3.9 Electrochemical performance of lean electrolyte Li-SPAN batteries with different electrolytes. (a) Lean electrolyte (3g Ah^{-1}) cycling performance of thick SPAN electrode in Carbonates and DME/DOL with $LiNO_3$. (b) Voltage profile in 1 M LiTFSI-EC/DMC. (c) Voltage profile in 1 M LiTFSI-EC/EMC. (d) Voltage profile in 1 M LiTFSI-DME/DOL with 0.5 M $LiNO_3$. The cells were cycled at C/5 (1C = 550 mAh g^{-1}).

While the high loading SPAN cells with lean carbonate electrolyte either shorted quickly or experienced fast capacity decay, the lean ENE electrolyte cell with the help of LiF rich CEI showed very stable cycling for 40 cycles as displayed in Figure 3.9d. The electrode delivers an initial reversible capacity of 6.67 mAh cm^{-2}, which still maintains 6.34 mAh cm^{-2} at the 40th cycle. In terms of the voltage profiles, the CarE electrolyte cell shows rapid polarization increase, while the ENE one is relatively stable. The amplified difference in cycling stability arises from the

difference in lithium morphology. When the mossy morphology is formed in the carbonate electrolyte, the porous lithium requires electrolyte to fill the pores, a major issue with lean electrolyte conditions. The cell impedance will quickly rise as a consequence of electrolyte consumption. In addition, the dendritic morphology in the carbonate electrolyte could also result in internal shorts, as shown in the 1 M LiTFSI-EC/EMC electrolyte. The deposition of large lithium grains in the ENE electrolyte combined with LiF-rich CEI enabled stable cycling of high areal capacity SPAN electrode cycled under lean electrolyte conditions.

3.4 Conclusions

In conclusion, we have conducted detailed structural, chemical and electrochemical analysis of Li||SPAN cells with three electrolytes, CarE that enables stable cycling of SPAN but not Li, EE that enables stable cycling of Li but not SPAN, and ENE that allows both electrodes to cycle stably. XPS results have revealed the formation of a robust LiF-rich CEI layer in the ENE. The role of the LiF-rich CEI layer has been further explored with the S K-edge spatially-resolved XAS/XRF, which reveal the formation of Li_2S_x on the SPAN cathode after one discharge-charge cycle. In the EE electrolyte, Li_2S_x diffuses to the Li anode and covers the Li surface in its reduced form of Li_2S. In ENE, a robust LiF-rich CEI on the SPAN cathode enables effective prevention of Li_2S_x shuttling and retaining Li_2S_x on the SPAN cathode, as evidenced by the absence of Li_2S formation on the Li metal anode. Leveraging the good compatibility between Li and ether-based electrolyte and our improved understanding in the role of LiF-rich CEI, we are able to realize a stable-cycling and high-energy density Li||SPAN cell with a high areal loading SPAN cathode (> 6.5 mAh cm^{-2}) and a lean electrolyte amount of 3 g Ah^{-1} that shows 40 stable cycles in the ENE electrolyte. Our work proves the benefits of using an ether electrolyte with nitrate additives for

Li||SPAN cells under a high-loading, lean-electrolyte condition and advanced the understanding of the critical roles of electrode/electrolyte interfaces on enabling stable cycling of SPAN.

Acknowledgements

Chapter 3, in full, is a reprint of the material as it appears in ACS Applied Materials & Interfaces, **Zhaohui Wu**, Seong-Min Bak, Zulipiya Shadike, Sicen Yu, Enyuan Hu, Xing Xing, Yonghua Du, Xiao-Qing Yang, Haodong Liu, Ping Liu. The dissertation author was the primary investigator and author of this paper.

CHAPTER 4 BINDER EFFECTS ON CYCLING PERFORMANCE OF HIGH AREAL CAPACITY SPAN ELECTRODES

4.1 Introduction

Li-S battery is regarded as a highly desirable choice to replace Li-ion batteries due to its high energy density and the absence of transition metals. Sulfurized polyacrylonitrile (SPAN) has promising specific energy (> 1249 Wh kg^{-1}) with superior cycling performance, in contrast to elemental S-based materials.[12,60] In addition, the solid-solid reaction mechanism of SPAN unlocks the possibility of decreasing the porosity of the electrode, key to minimizing the amount of electrolyte and achieve high cell energy density.[6] However, most reported studies on SPAN have been performed with modest active material loadings, resulting in low practical cell-level energy densities.[58,66,82] The main challenges for high loading cathodes are mechanical failures such as cracking and delamination from the current collector, leading to cell capacity degradation as the conductive network breaks. These structure failures are further exaggerated by the volume change during repeated lithiation and de-lithiation.[17] To address these challenges, binder is the key as they provide the mechanical skeleton of the electrode structure. Regarding the amount of binder, 10% is commonly used in literature to fabricate SPAN electrodes.[82–84] Adding more binder could improve the durability of the SPAN cathode but sacrifice the overall energy density. Improving the mechanical property of the binder is another way to tackle this problem without sacrifing cell energy. For example, Yang et al. and Chen et al. have developed two novel binders to improve the cycling performance of SPAN cathode.[17,85] However, their binders are not commercially available, which limit their practical applications.

This work studies the effects of binders on the cycling performance of high areal capacity (> 6 mAh g^{-1}) SPAN cathode. We compare electrodes made with two commercially available

binders, PVdF and CMC. Although previous work indicates that CMC binder improves the rate capability of SPAN electrodes with low areal capacity (~ 1 mAh cm^{-2}),[86] here, we show that the choice of the binder has a decisive effect on the mechanical integrity and cycling stability of high areal capacity SPAN cathodes, especially at low electrode porosities.

4.2 Experimental section

The synthesis of SPAN was described previously.[87] The electrodes were made by mixing SPAN, SuperP, and binder (PVdF or CMC) in an 8:1:1 ratio. After drying, electrodes were punched into 12 mm disks. Roll-press calendering was employed to control the porosity of the cathode. The thickness of the electrode was measured by a micrometer to confirm that the desired porosity was achieved. The porosity of the electrode is calculated by the following equation: $\epsilon = \left(1 - \frac{\rho_{appa}}{\rho_{theo}}\right) \times 100\% = \left(1 - \frac{\frac{W_{cathode}}{V_{cathode}}}{\rho_{SPAN} \times u_{SPAN} + \rho_{carbon} \times u_{carbon} + \rho_{binder} \times u_{binder}}\right) \times 100\%$, where ρ_{appa}, ρ_{theo}, $W_{cathode}$, $V_{cathode}$, ρ_{span}, u_{span}, ρ_{carbon}, u_{carbon}, ρ_{binder}, u_{binder}, are the apparent density, theoretical density, weight, and volume of the cathode; density, and volume fraction of SPAN; density, and volume fraction of carbon, density, and volume fraction of binder, respectively. The densities of the active material, carbon black, and binder used for porosity calculation were 1.81, 2.0, and 1.78 or 1.6 g/cm^3, respectively. 2032 coin cells were assembled in argon filled glovebox with oxgen and moisture levels of < 0.1 ppm. The electrolyte was prepared by mixing 1.8 M LiFSI in Diethyl ether (DEE)/Bis(2,2,2-trifluoroethyl)ether (BTFE) (weight ratio 1:4) solution. Cells were cycled at C/20 rate for two cycles and then switched to C/5 rate. Electrochemical impedance spectroscopy (EIS) was performed using BioLogic VSP 300 potentiostat from 7 MHz to 10 mHz. Scanning electron microscopy (SEM) was performed on the FEI Quanta 250 SEM. The 180° peeling test was adopted from work by Ryou et al.[88]

4.3 Results and Discussion

We first performed a cell specific energy modeling to define the desired cathode loading. As shown in Figure 4.1, a loading of > 6 mAh cm^{-2} is required to reach 334 Wh kg^{-1} for the Li||SPAN cell, enough to compete with Li-ion batteries.[89] When PVdF is used as the binder, the SPAN electrode with a 1 mg cm^{-2} loading and 50% porosity shows excellent cycling stability, with no noticeable change of the voltage profiles throughout 60 cycles at a C/5 rate, indicating the material itself is highly stable (Figure 4.2a and b). We chose a rate of C/5 for cycling since it is close to practical battery operation conditions. Even higher rates would lead to severe degradation of the lithium counter electrode due to the high current density, particularly when the cathode loading is high. Unfortunately, as shown in Figure 4.2a and c, the Li||SPAN cell shows rapid capacity fade from 650 to 400 mAh g^{-1} within 60 cycles for an electrode loading of 10 mg cm^{-2}. The corresponding voltage profiles in Figure 4.2c also indicate a fast polarization increase.

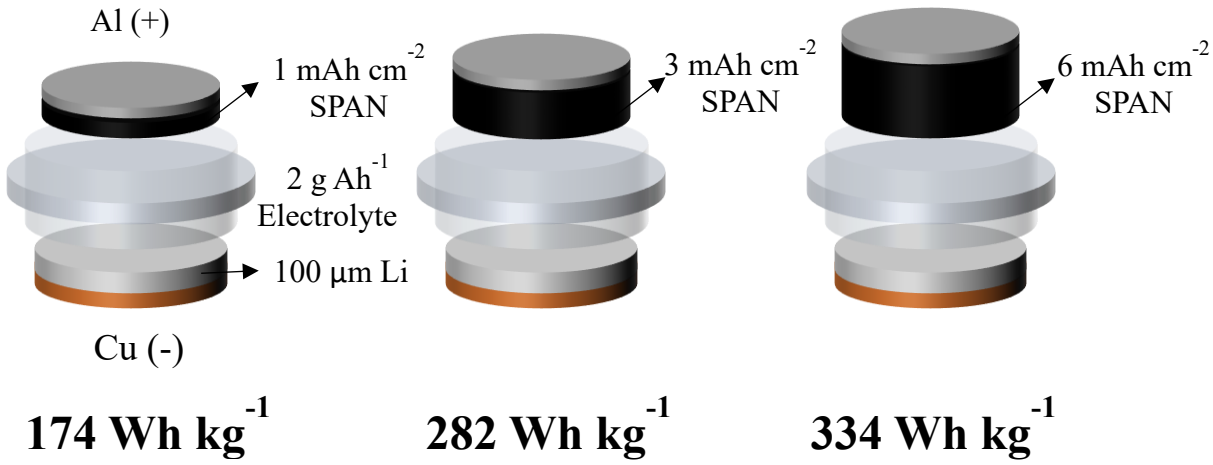

Figure 4.1. Energy density projection of Li||SPAN pouch cell with different areal capacity SPAN cathodes.

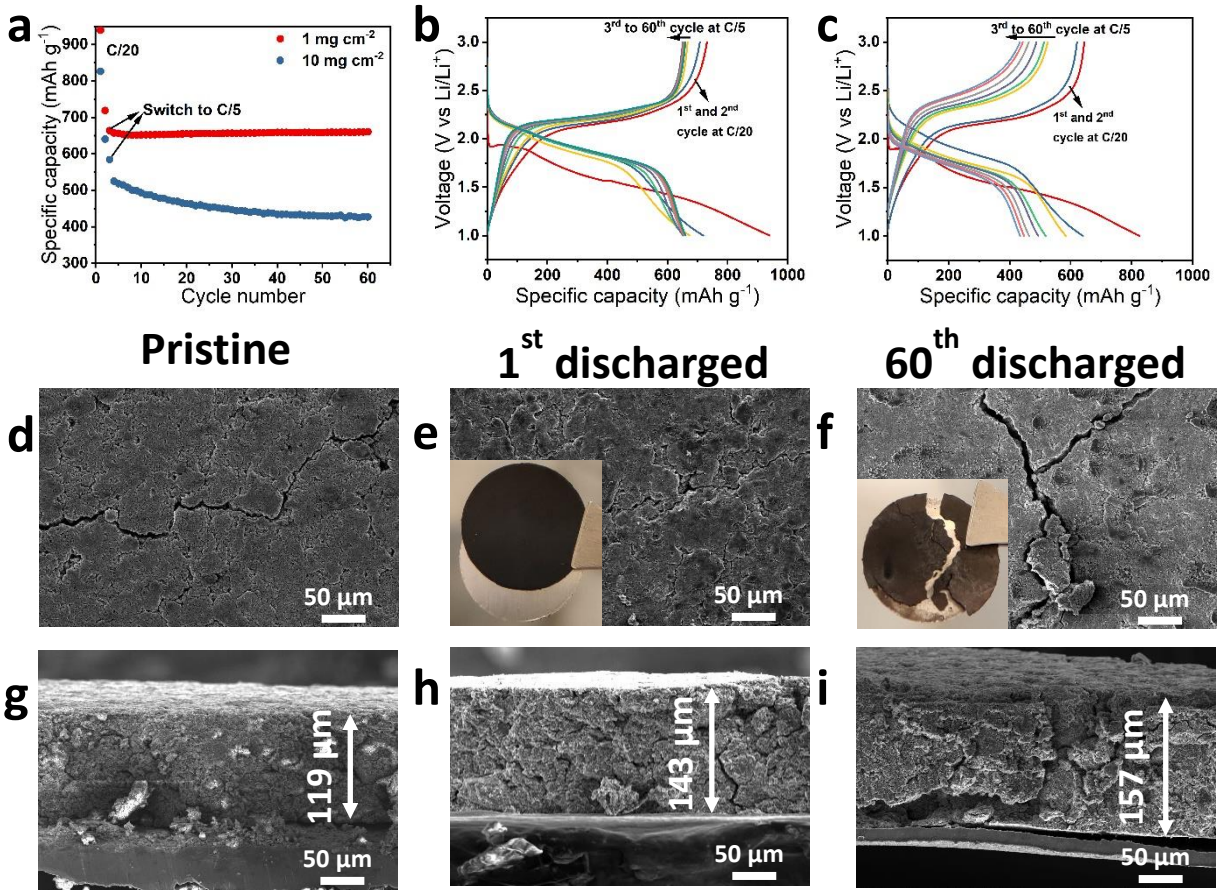

Figure 4.2. Comparison of the cycling performance of SPAN cathodes with different areal mass loading. a) capacity retention of 1 mg cm^{-2} and 10 mg cm^{-2} SPAN electrode with PVdF as the binder, b) voltage profiles of 1 mg cm^{-2} SPAN cathode, c) voltage profiles of 10 mg cm^{-2} SPAN cathode. The cell was cycled under C/20 rate for two formation cycles and then cycled under C/5 rate, 1C=550 mA h g^{-1}. Top view SEM images of d) pristine, e) 1st discharged, f) 60th discharged high areal capacity SPAN electrode. Cross-sectional view SEM images of g) pristine, h) 1st discharged, i) 60th discharged high areal capacity SPAN electrode.

The degradation observed in Figure 4.2c is due to the failure of the thick cathode, not the Li anode. To prove this, we note that the electrolyte used in these tests is LDEE (1.8 M LiFSI in DEE/BTFE).[16] The average Li metal coulombic efficiency in this electrolyte is > 99% for 200 cycles, in contrast to < 90% with rapid deterioration in 30 cycles in carbonate electrolytes (Figure 4.3). It is well known that the effect of Li degradation is insignificant at low current densities. Therefore, SPAN cathodes have been reported to be stable in carbonate electrolytes when tested against Li.[53,70,73] However, at high loadings and current densities, Li metal degradation becomes significant.[55,56] Figure 4.4 shows that Li||SPAN cell experiences continuous capacity decay in carbonate electrolytes caused by both cathode and anode failure. The use of the LDEE electrolyte thus allows us to focus on the degradation of the thick cathode only.

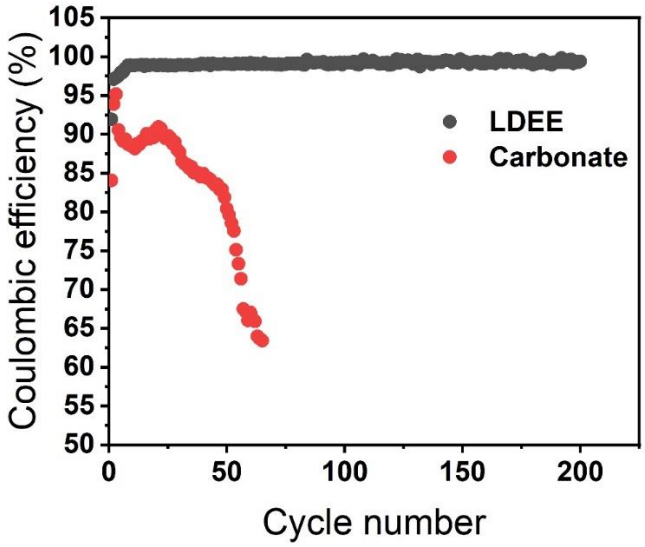

Figure 4.3. Li||Cu cell coulombic efficiency in LDEE (1.8 M LiFSI in Diethyl ether/Bis(2,2,2-trifluoroethyl) ether (weight ratio 1:4)) and carbonate electrolyte (1 M $LiPF_6$ in Ethylene carbonate/Ethyl methyl carbonate (weight ratio 1:1)). Plating at 0.5 mA cm^{-2} and stripping at 0.5 mA cm^{-2} for 1 mAh cm^{-2}.

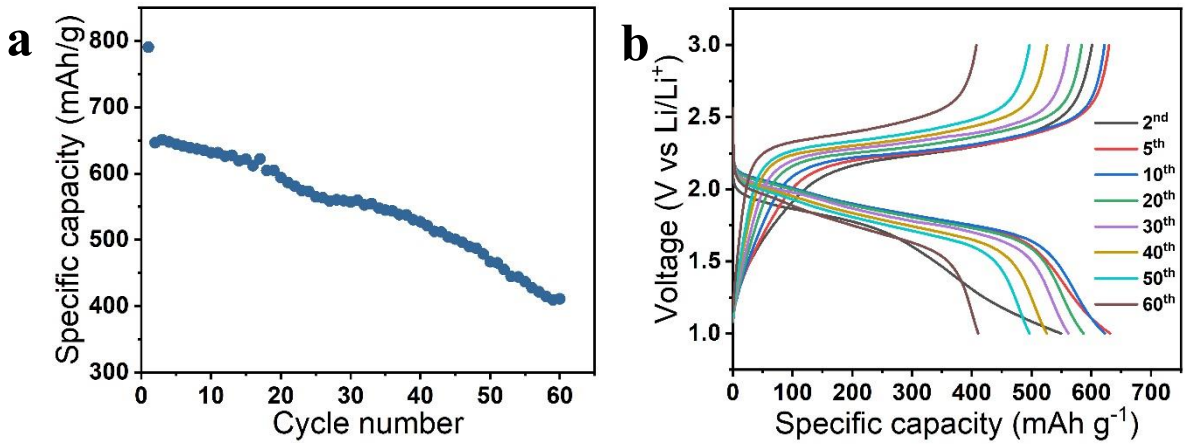

Figure 4.4. Cycling performance of the > 6 mAh cm^{-2} SPAN cathode in carbonate electrolyte. a) the specific capacity of SPAN throughout 60 cycles, b) the voltage profiles of the cell. The cell was tested under a C/5 rate against Li foil.

The morphology of the thick SPAN cathodes before and after cycling were studied by SEM. Figure 4.2d and g are the top and cross-sectional view images of the pristine cathode. The presence of cracks indicates the poor mechanical property and is likely due to the stress generated during solvent evaporation. After the 1st cycle, the electrode is shown to have already delaminated from the current collector (optical image, Figure 4.2e inset). The cathode thickness has increased from 119 to 143 μm after the first lithiation (Figure 4.2h). More cracks have formed vertically from the bottom to the top of the electrode. Additional contact resistance could arise at the interface between the current collector and the electrode. The mechanical failure due to crack, delamination, and volume change is likely the root cause of the rapid capacity fading of the 10 mg cm^{-2} SPAN electrode. After 60 cycles, the repeated expansion/contraction and the faster rate after formation cycles led to a more severe mechanical failure. **(**Figure 4.2f and i). Cracks, delamination, and even pulverization are observed in both optical and SEM images. The mechanical disintegration of the thick electrode will further lead to the breakage of the conductive network thus causing active material loss and/or polarization increase during cycling.

Optimizing the polymer binder is an effective approach to improve the electrode mechanical integrity. For example, He et al. showed that sulfur cathode with CMC-SBR binder performed much better than PVdF because of stronger adhesion and better dispersion.[90] Figure 4.5 shows the results from a 180° peeling test on thick SPAN electrodes with two different binders. The CMC-based electrode is much more robust, with an average peeling force at 1.03 N, three times that of PVDF-based electrode. As shown in Figure 4.6a, the 6 mAh cm^{-2} SPAN cathode with CMC binder maintains 94.5% of its capacity (based on the 3rd cycle) at the 60th cycle, a dramatic improvement over the corresponding value of 66.7% for PVDF. The voltage profiles in Figure 4.6b also indicate minimal degradation. We note that the initial reversible capacity is higher than the electrode with the PVdF binder. This is likely due to the improved mechanical property preventing SPAN particles disintegrating from the conductive network. Furthermore, the SEM images of the pristine and cycled electrodes in Figure 4.6c-f reveal no visible cracks or delamination, proving the electrode's durability. Electrochemical impedance spectroscopy (EIS) was used to characterize PVdF and CMC based electrodes after cycling. Figure 4.6g shows results from the electrodes at 50% SoC of the 1st charge. The EIS spectra were fitted using the equivalent circuit illustrated in Figure 4.7. The much larger charge transfer resistance from the PVdF based electrode (62.68 Ω) as compared to the CMC one (21.54 Ω) implies that even after 1st discharge the cathode with PVdF binder has already degraded. The charge transfer resistance of the PVdF based electrode significantly increases to 127.4 Ω after 10 cycles, while the CMC based electrode shows only a slight increase of the cell impedance (Figure 4.6h). The EIS analysis further proves the advantages of CMC binder.

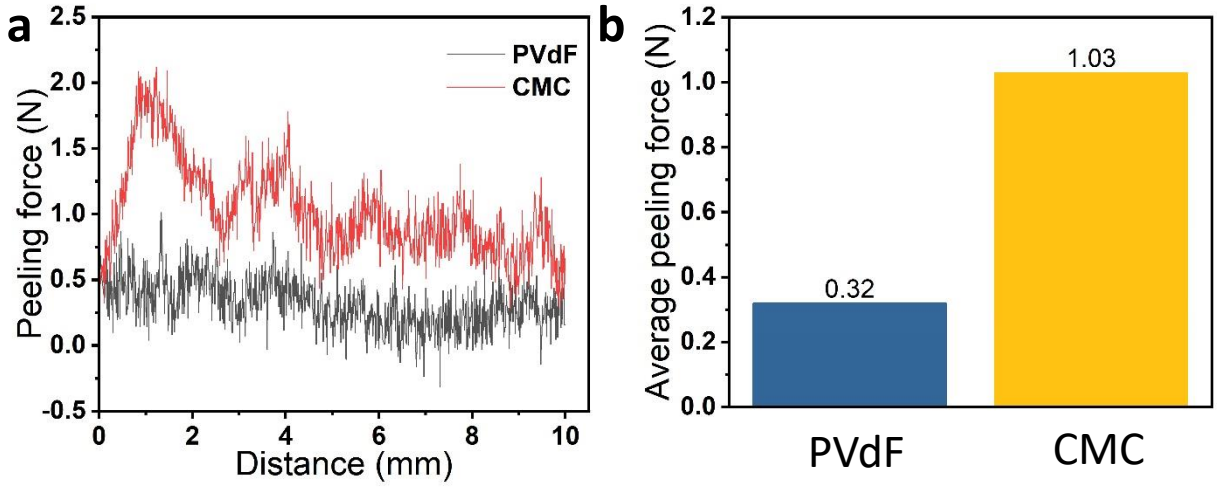

Figure 4.5. a) Peeling force of 10 mg cm^{-2} SPAN electrode with different binders. b) average peeling force.

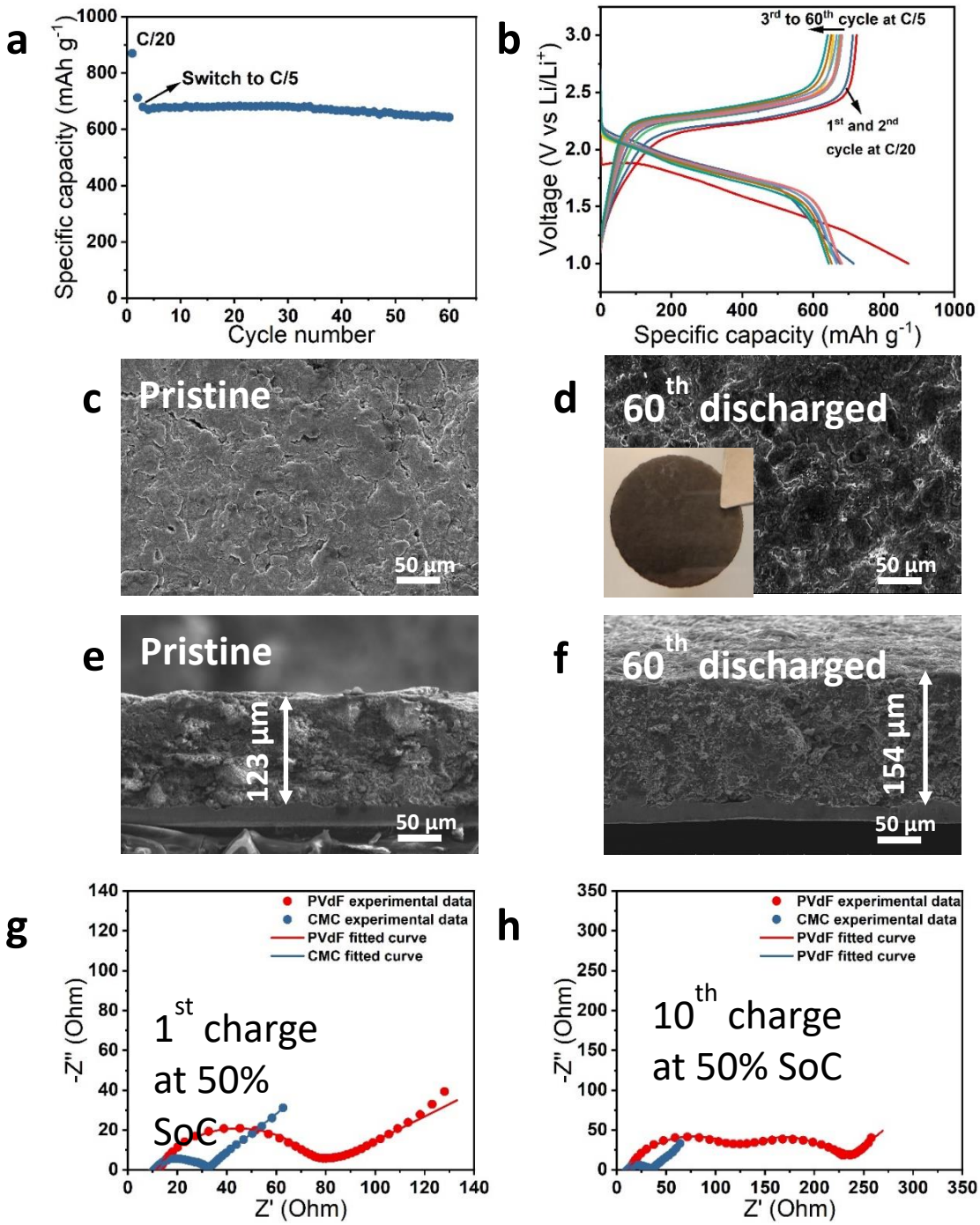

Figure 4.6. High areal loading SPAN cathode with CMC as the binder. a) Capacity retention of 10 mg cm^{-2} SPAN electrode with CMC as the binder. b) Voltage profiles of the same SPAN cell. SEM images of high areal capacity SPAN cathode with CMC binder. Top-view images of c) pristine, d) after 60^{th} discharge. Cross-sectional view images of e) pristine, f) after 60^{th} discharge. Electrochemical impedance spectroscopy of SPAN electrode with different binder at g) 50% SoC of 1^{st} charge, h) 10^{th} charge.

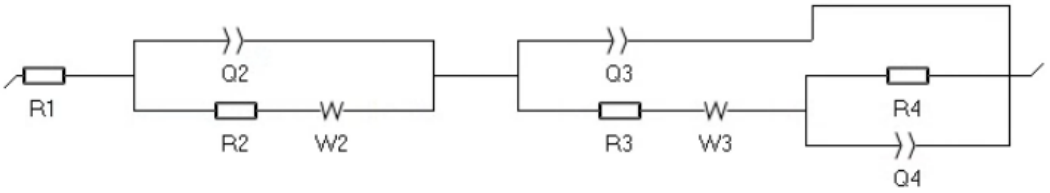

Figure 4.7. Equivalent circuit for Li||SPAN cells impedance simulation. R1 is resistance from the electrolyte. Q2 is the CPE from cathode. R2 is the charge transfer resistance from cathode. W2 is the Warburg diffusion from cathode. Q3 is the CPE from electrolyte and SEI interface. R3 is the resistance from SEI. W3 is the diffusion element from anode. Q4 is the charge transfer resistance from anode. Q4 is the CPE element from interface between SEI and anode.

Another critical step towards high energy density Li||SPAN battery is to reduce the cathode porosity. Because lower porosity electrode requires less electrolyte, resulting in higher cell level energy density. The binder plays a key role at low porosity because the SPAN electrode will expand outwardly due to the limited spaces inside, which will apply significant stress on the binder skeleton. We tested SPAN cathodes with 40% and 30% porosity, with the results shown in Figure 4.8a and b. The capacity of PVdF based electrodes quickly decays from 600 to < 150 mA h g^{-1} within 10 cycles, which is much faster than the PVdF based cathode with 50% porosity. Less room inside the electrodes promotes the outward expansion instead of inward expansion. The former leads to breakage of the carbon network, while the later could reinforce the contact between carbon and SPAN particles. Therefore, the cathode with less porosity shows a dramatically worse cyclability. In contrast, the 30% and 40% porosity SPAN electrodes using CMC binder are shown to maintain high capacity retention of 95.1% and 94.4%, respectively (Figure 4.8c and d), clearly demonstrating the benefits of using CMC for high areal loading, low porosity SPAN cathodes.

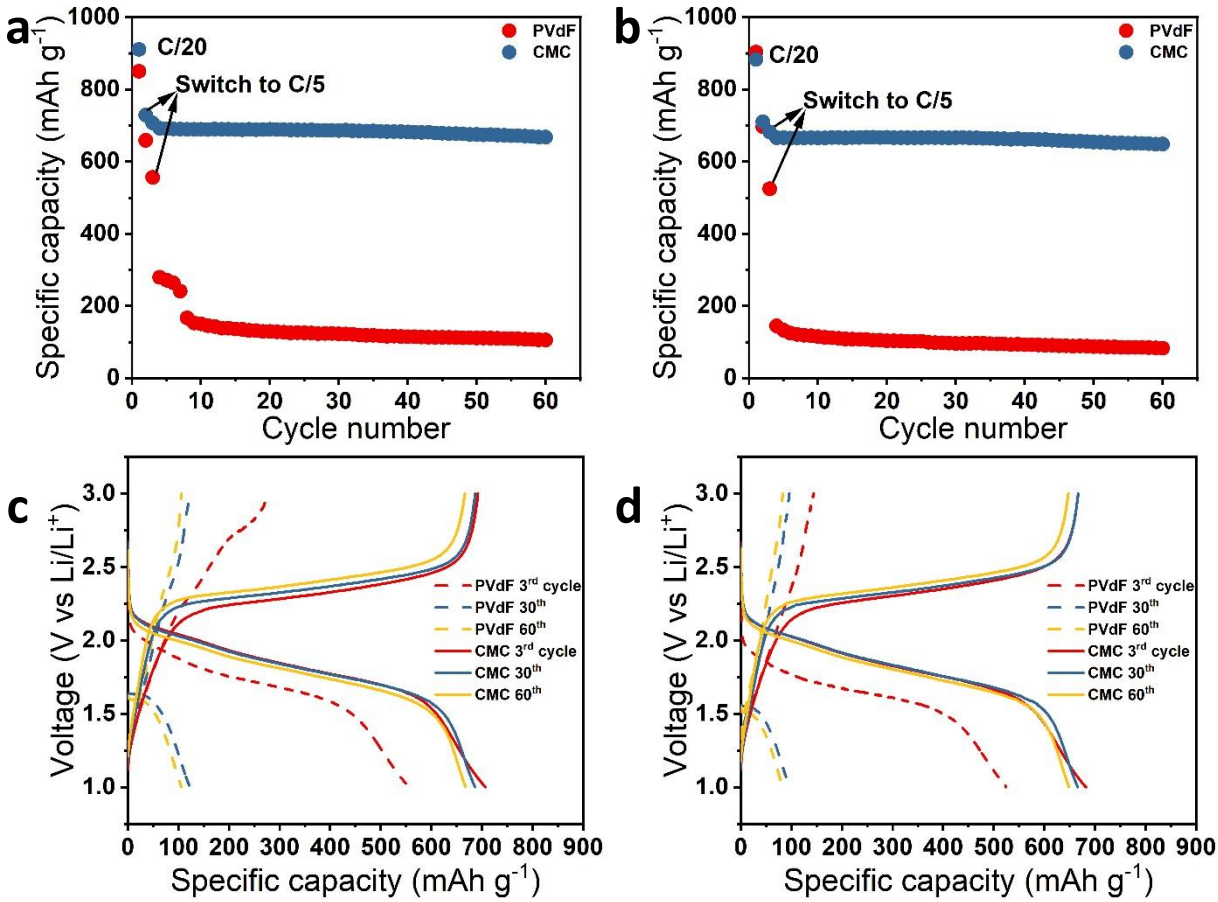

Figure 4.8. Comparison of the cycling performance of high areal capacity SPAN electrodes. a) 40% cathode porosity, b) 30% cathode porosity. Voltage profiles of Li||SPAN cells with c) 40% cathode porosity, different binder, d) 30% cathode porosity, different binder.

4.4 Conclusions

We have studied the effect of binders on cycling performance of high areal capacity SPAN cathodes. The mechanical property of the electrode is significantly improved when switching from PVdF to CMC. Therefore, the cracking, delamination, and pulverization issues of the thick SPAN cathodes are mitigated. As a result, the SPAN cathode (> 6mAh cm^{-2}, 50% porosity) with CMC binder shows significantly improved capacity retention of 94.5% for 60 cycles, while the SPAN cathode with PVDF binder rapidly degrades to 66.7% of its original capacity. In addition, the 30% porosity electrode with CMC retains a high specific capacity of 648.6 mAh g^{-1} after 60 cycles.

Thus, we show binder optimization is an essential step toward a Li||SPAN battery with high cell-level energy density.

Acknowledgements

Chapter 4, in full, is a reprint of the material as it appears in Journal of the Electrochemical Society, **Zhaohui Wu**, Haodong Liu, Sicen Yu, Ping Liu. The dissertation author was the primary investigator and author of this paper.

CHAPTER 5 REGULATING LI NUCLEATION AND GROWTH FOR REALIZING STABLE LITHIUM METAL BATTERIES UNDER PRACTICAL CONDITIONS

5.1 Introduction

Li metal is regarded as the holy grail of rechargeable battery anode due to its high capacity (3862 mAh g^{-1}, 2062 Ah L^{-1}) and low electrochemical potential (-3.04 V vs. SHE).[6,91] Despite many efforts having been made,[16,79,92–94] the industrial deployment of Li metal battery (LMB) is still impeded by its low reversibility and short cycle life, which are fundamentally related to the dendritic and porous morphology of electrochemically deposited Li.[19,95] The parasitic reaction accelerated by the high surface area of porous Li and the "dead" Li formation caused by non-uniform dissolution of dendritic Li were proven to be the primary sources of Li loss in LMB.[96,97] Many approaches have been taken to improve the morphology of the Li deposition, including designing electrolyte with optimized composition,[16,93,98] protecting Li surface with artificial coatings,[22,99] and constructing 3D skeleton structure to host Li,[100,101] etc.

Modifying the current collector is another promising strategy since it directly affects the current and Li-ion flux distribution. For example, copper nitride was employed as a substrate modification on Cu to regulate Li deposition.[23] Cu_3N is electrochemically converted into Cu/Li_3N nanocomposites, providing uniform surface conductivity, which results in improved Li morphology and cyclability. Another study has shown that modifying the Cu current collector with lithophilic Ag nanoparticles could regulate the Li morphology.[102] Substrate modification would directly affect the Li nucleation behavior, which dictates the following deposition. The Li nucleation process has been intensively studied due to its scientific interests and practical application. A Li-SEI model was proposed to understand the Li nucleation and growth mechanism quantitatively and was combined with chronoamperometry to determine important kinetic

parameters during nucleation and growth.[103] Another report elucidated the dependence of lithium nuclei size, shape, areal density on current.[104] The effects of crystallographic orientation were examined by cryogenic TEM and X-Ray diffraction,[105–107] where exposing (110) planes was found to be energetically favorable. The high current initial deposition was employed to plant ultrafine Li seeds, guiding the following deposition.[108] Electrolyte additive, such as $LiNO_3$, was found to be effective in tuning the Li nucleation and deposition.[109]

This work aims to provide an in-depth analysis of the substrate effect on Li nucleation and how it affects the following deposition and cycling performance. Here, we propose to use Fe/LiF nanocomposite modified Cu as a substrate for Li deposition. (Figure 5.1) The *in-situ* conversion of FeF_3 generates uniform Fe/LiF nanocomposite. Our previous study has shown that the lithiation of iron halogen compounds generated exceptionally smaller size metal particles, compared to copper and other transition metal.[110] We believe that the nanosize Fe particle will provide abundant nucleation sites for Li, leading to a uniform Li seeding at the initial deposition stage. The other conversion product, LiF, has been demonstrated to have high surface energy and low diffusion barrier for Li, which will preferentially induce dendrite-dree morphology.[95] Multiple reports have shown that columnar Li deposition was realized by applying a LiF-rich layer on Cu,[111,112], which clearly proves the Li regulation effect of LiF.

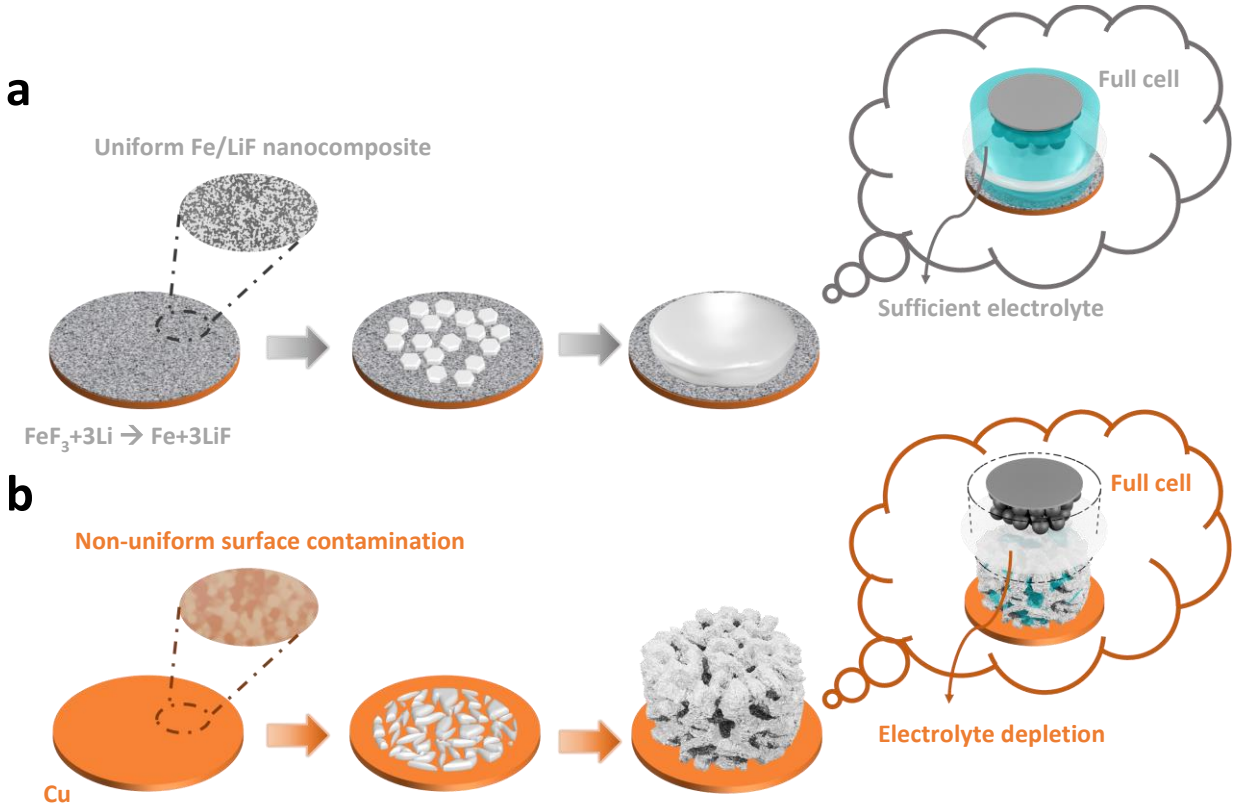

Figure 5.1. Schematic illustration of Li plated on different substrate. a, Fe/LiF nanocomposite regulates Li nucleation and growth, resulted in dense Li deposition and improved full cell performance. b, Random Li nucleation on bare Cu leads to porous Li plating and consequently poor performance in full cell due to electrolyte depletion.

In this work, we deposited Li on Fe/LiF nanocomposite substrate and observed micron size hexagonal Li crystal nucleation behavior, which was proven to be independent of the current density and temperature. Transmission electron microscopy (TEM) confirmed that the hexagonal Li is a single crystal and dominated by $(110)_{Li}$ crystallographic orientation. The unique nucleation behavior led to regulated Li growth in the following deposition. Specifically, Li morphology with different capacities (up to 9 mAh cm^{-2}) and deposition current density (up to 5 mA cm^{-2}) was examined by scanning electron microscopy (SEM), where significantly denser Li deposition was observed on the Fe/LiF nanocomposite substrate than the Cu. Half-cell tests have shown more than 1000 and 600 stable cycles at 3 mA cm^{-2} and 5 mA cm^{-2}, respectively, with an average efficiency

> 99%. A remarkable performance improvement was also observed in the 3 mAh cm^{-2} NMC811 full cell test, when lean electrolyte (3 g Ah^{-1}) and 1x excess Li were used, which was attributed to the much less porosity of Li deposited on Fe/LiF nanocomposite modified Cu.

5.2 Experimental section

FeF3 thin film

The FeF3 thin film was prepared by thermal evaporation (Angstrom Engineering Nexdep EB Evaporator) of FeF3 powder (Sigma-Aldrich).

Cathode

NMC811 was purchased from Targray. A cathode slurry was prepared by mixing NMC811, SuperP, and polyvinylidene fluoride (PVdF) in N-methylpyrrolidone (NMP) solution by Thinky mixer. The ratio between three components is 90:5:5. The slurry was coated on Al foil using doctor blade. The areal mass loading was controlled at 16 mg cm-2 and 8 mg cm-2, respectively. After drying in the vacuum oven at 120 °C overnight, the electrodes were calendered into 30% porosity, and then punched into 12 mm diameter disk for coin cell test.

Electrolyte

Dimethoxyethane was purchased from Gotion. Lithium bis(fluorosulfonyl)imide (LiFSI) was purchased from Sigma-Aldrich. Lithium bis(fluorosulfonyl)imide was purchased from Synquest Lab. The LDME electrolyte was prepared by dissolving 2.54 M LiFSI in DME/BTFE. Here, 1 M is defined as 1 M salt dissolved into 1 kg of solvent.

Battery assembly

2016-type coin cells were used for Li deposition and half-cell test. Each cell includes a 250 μm Li chip, a 25 μm celgard separator, a 1 mm spacer, a piece of bare Cu or Fe/LiF coated Cu, and 75 μL electrolyte.

2032-type coin cells with Al coated positive case were used for full cell test. The Al coated case was used to prevent corrosion. Predetermined amount of Li was deposited on Cu or Fe/LiF nanocomposite modified Cu. Full cells were assembled with NMC811 cathodes, Cu or Fe/LiF modified Cu with pre-deposited Li, celgard separators, spacers, and springs. The electrolyte amount was controlled as 3 g Ah^{-1}.

Electrochemical testing

Li deposition and half-cell tests were conducted on an LBT-5V5A battery tester (Arbin instruments). cells were firstly discharged at 10 μA until 0 V. An additional 24 hours 0.2 V constant voltage hold was applied in the Fe/LiF cells to fully lithiate the thin film. Once 0 V was reached, constant current discharges with different current densities and deposition time were applied to deposit Li. Cells for the morphology observation were disassembled after deposition. Cells for cycling test were then stripped to 1 V.

For the full cell, cycling tests were carried out using battery testers (LANHE CT2001A). The batteries were tested in the voltage range of 2.8~4.4 V under a constant-current, constant-voltage charge and a constant-current discharge mode. When the charge voltage reached the set cutoff, the constant-voltage charge process was applied until the charge current decayed to C/20. The capacity retention was calculated on the third cycle capacity, after two formation cycles.

The low temperature test was conducted in SolidCold C4-76A ultra-low chest freezers at −40 °C. The current density used in the low temperature test was 0.25 mA cm^{-2}.

SEM

To perform morphological observation, cells were disassembled in Argon filled glovebox. The deposited Li was washed with dimethyl carbonate to remove residual electrolytes. The morphology and thickness of the deposited Li were characterized using scanning electron microscopy (FEI Quanta 250 SEM). The cryogenic focused ion beam milling was conducted using FEI Scios DualBeam FIB/SEM.

Cryo-TEM experiments

The samples used for TEM observations were prepared by the method illustrated in Figure 5.2. Specifically, FeF_3 was evaporated on a thin carbon film supported Cu grid, which was assembled into a coin cell. After electrochemically converting FeF_3 into Fe/LiF nanocomposite, 0.1 mAh cm^{-2} Li was plated on it. The SEM image of the Li deposited TEM grid was shown in Figure 5.3, where hexagonal shape Li crystals were observed, showing great agreement with Li plated on the Fe/LiF nanocomposite modified Cu.

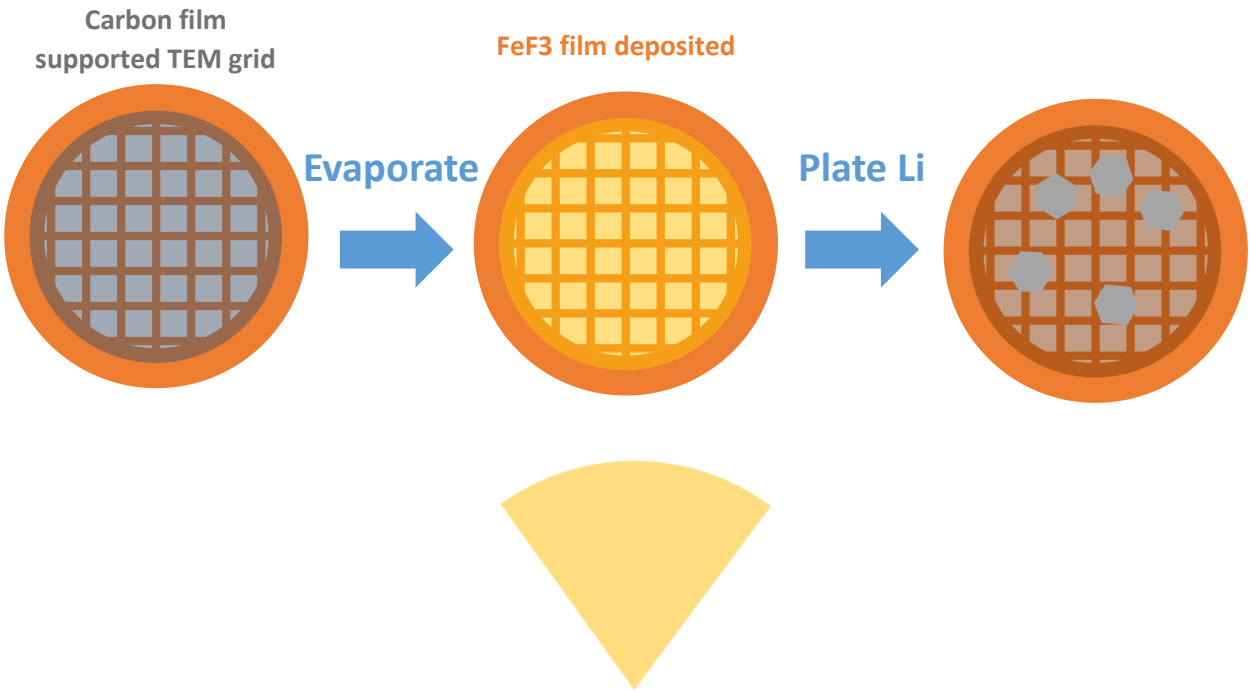

Figure 5.2 Schematic of method for preparing TEM sample.

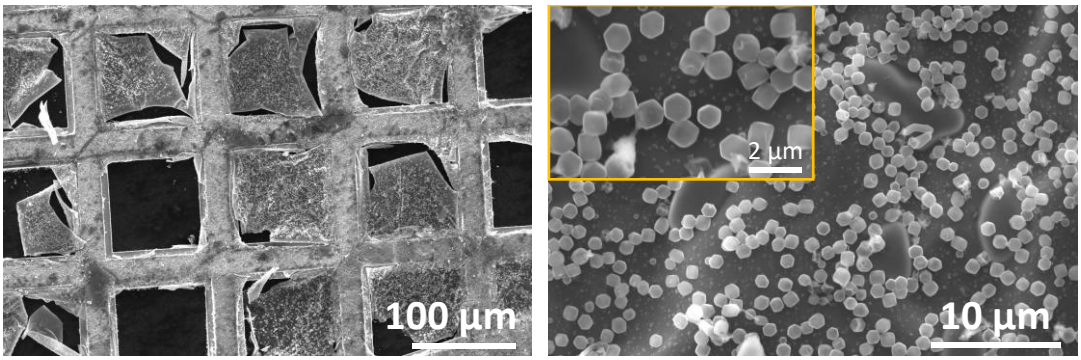

Figure 5.3 SEM images of 0.1 mAh cm-2 Li deposited on Fe/LiF nanocomposite coated carbon film supported TEM grid.

The cryo-TEM experiments were conducted in an FEI Talos F200X transmission electron microscope (operated at 200 kV) with an X-FEG field emission source and Super-X EDS detectors. To keep the sample at cryogenic temperature (~ -185 °C) in TEM, a Gatan liquid nitrogen holder with an anti-frost window was used to transfer the TEM sample at liquid nitrogen temperature. To prepare the TEM samples for the cryo-TEM experiments, we assembled coin cells with copper grids inserted onto a Cu foil electrode in a glove box protected by an argon atmosphere. After electrochemical deposition, coin cells were disassembled and the copper grids were sealed in aluminum pouch bags. The sealed grids were plunged into a liquid nitrogen bath and quickly loaded onto the precooled cryo holder. With the protection of the anti-frost widow, the cryo holder was soon inserted into the TEM for further characterization. To perform the cryo-TEM tomography experiments, annular dark-field scanning transmission electron microscopy (ADF-STEM) imaging mode was used to acquire tilt series with a maximum tilt range of +/-80°. The data were aligned by cross-correlation function and reconstructed by SIRT algorithm. The 3D tomographic reconstruction was visualized by Avizo.

XPS

X-ray Photoelectron Spectroscopy (XPS) (Physical Electronics, Quantera Scanning XPS Microprobe System) was carried out using Al anode source at 15 kV. Obtained data were calibrated based on the reference of C-C bond at 284.6 eV and fitted in CasaXPS.

5.3 Results and Discussions

Preparation and characterizations of FeF_3 substrate

The FeF_3 substrate was prepared by thermal evaporation of FeF_3 powder onto Cu. Top view SEM image of the obtained film showed a crack-free morphology. (Figure 5.4a) The thickness of the film was determined to be ~ 270 nm by the cross-sectional view image obtained by FIB-SEM. (Figure 5.4b) Energy-dispersive X-ray spectroscopy (EDX) of the FeF_3 thin film showed a uniform Fe and F distribution, as shown in Figure 5.4c and d. X-ray photoelectron spectroscopy (XPS) data was collected to study the chemical composition of the thin film, where Fe2p and F1s spectra showed agreement with literature data. (Figure 5.5) The elemental ratio between Fe and F was determined from the XPS data to be 1:3. (Table 5.1) Therefore, the obtained sample was proved to be a 200-300 nm thick uniform FeF_3 thin film.

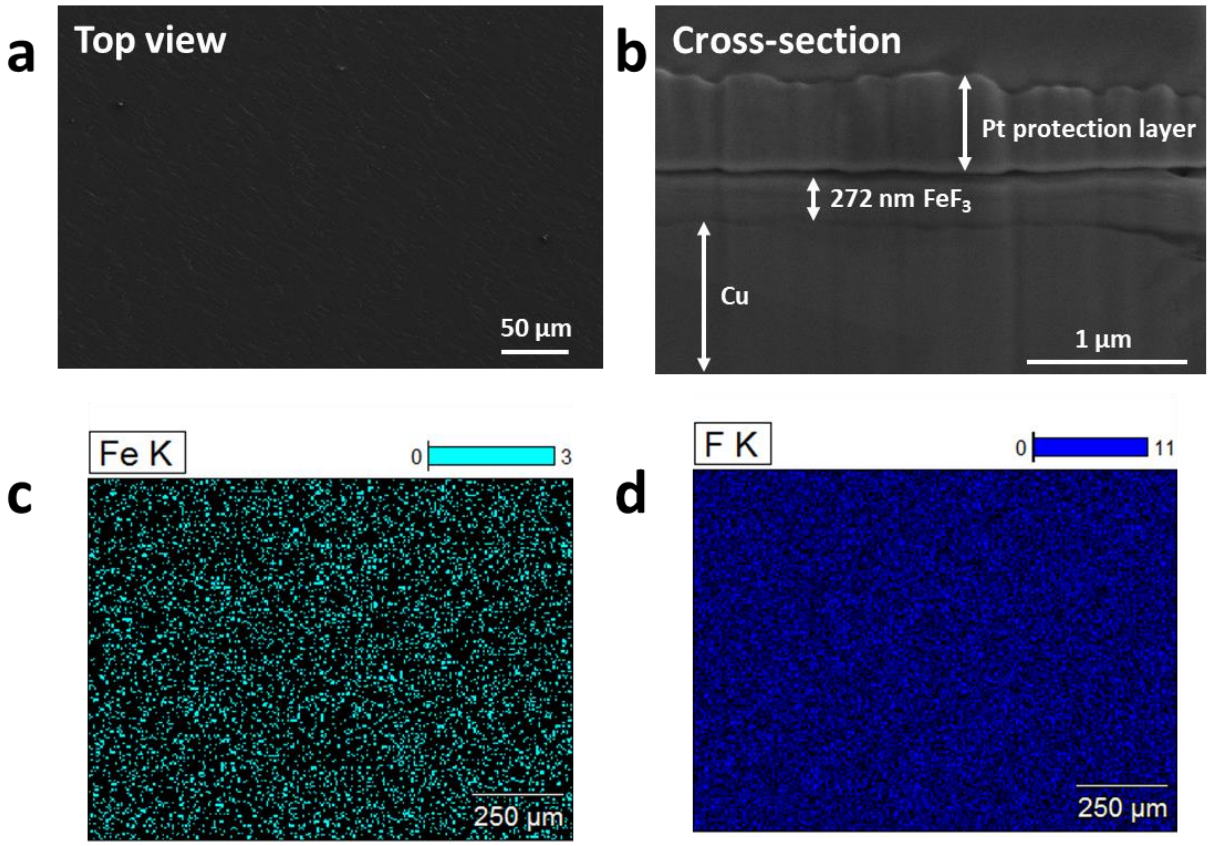

Figure 5.4 Morphological characterization of FeF_3 film. a, Top view SEM image of FeF_3 film. b, Cross-sectional image of FeF_3 by FIB-SEM. Energy dispersive X-ray spectroscopy (EDS) of FeF_3 film, c, Fe distribution, d, F distribution.

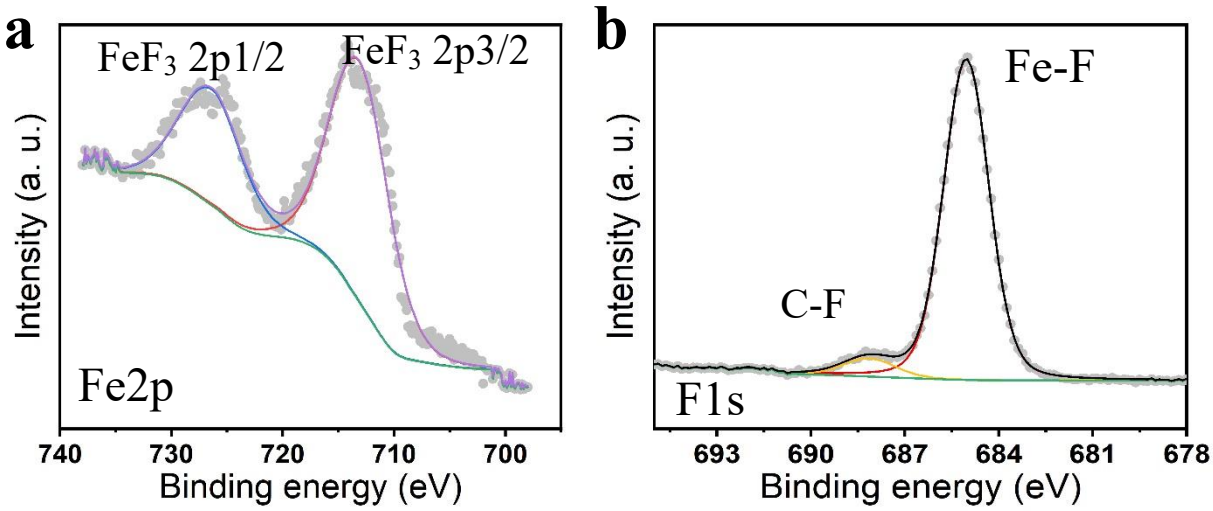

Figure 5.3 X-ray photoelectron spectroscopy of FeF_3 film. a, Fe2p spectra. b, F1s spectra.

Table 5.1. Elemental ratio of Fe, F, C, and O.

Elemental ratio
13.27
36.94
29.28
20.51

Li nucleation behavior on FeF_3 substrate

To investigate how the substrate affects the nucleation and initial growth of Li, 0.1 mAh cm^{-2} Li was deposited on Fe/LiF nanocomposite and Cu, after discharging to 0 V. The electrolyte used in the test is 2 M LiFSI in DME/BTFE (1:4 by weight) (LDME), which is an electrolyte that was proven to produce ultrahigh Li efficiency (> 99%) and dendrite free Li morphology.[16] The SEM images of Li deposition are shown in Figure 5.6 and 5.7. Despite the Li deposition in LDME

electrolyte is typically dendrite free,[113] to our surprise, the initial Li growth on Cu showed randomly oriented dendritic morphology. In contrast, the images of 0.1 mAh cm^{-2} Li deposited on Fe/LiF nanocomposite revealed uniformly distributed micron size hexagonal crystals, which, to the best of our knowledge, is the first time reported in the literature. Furthermore, different current density tests showed that the hexagonal crystal feature was well reserved up to 5 mA cm^{-2}, indicating the fast-charging capability of the Fe/LiF nanocomposite modified Cu (Figure 5.6 and 5.7). Additional evidence, the optical images of the deposited Li, was collected to investigate the morphological difference from a macroscopic view (Figure 5.8). The optical images of the Li deposited on Fe/LiF nanocomposite showed a silver color, while the Cu one is darker, which is typically associated with an irregulated morphology. In addition, -40 °C Li deposition was conducted to study the temperature influence on the unique nucleation behavior. It was found that the hexagonal crystal growth behavior persisted, which implies its promising application in low temperature LMB (Figure 5.9).

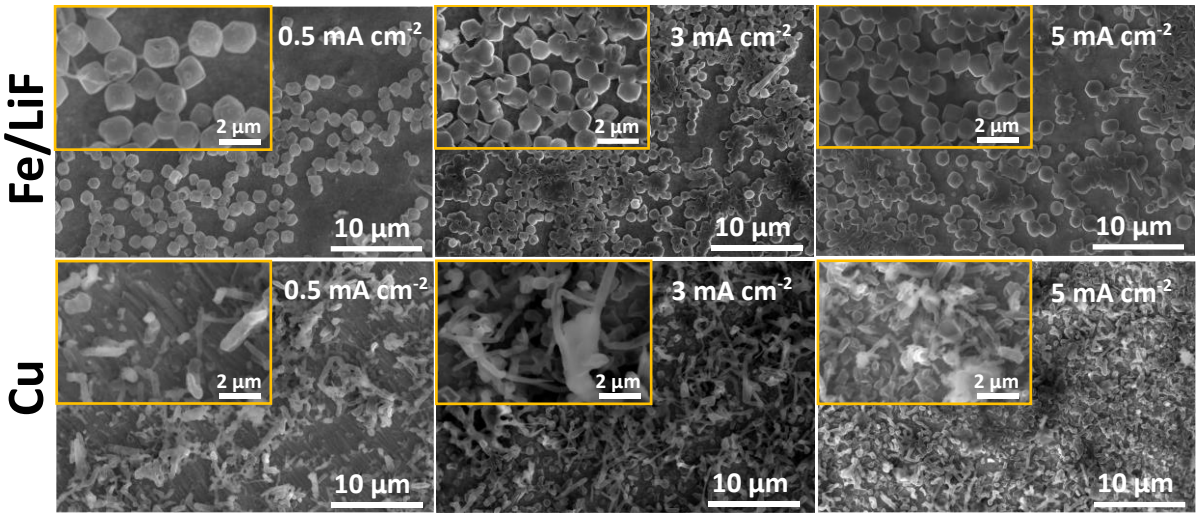

Figure 5.6 Morphology of initial Li deposition on different substrate. a, SEM images of 0.1 mAh cm^{-2} Li deposited on Fe/LiF nanocomposite and Cu, under different current density, including 0.5, 3, and 5 mA cm^{-2}. Inset figures are the higher magnification images.

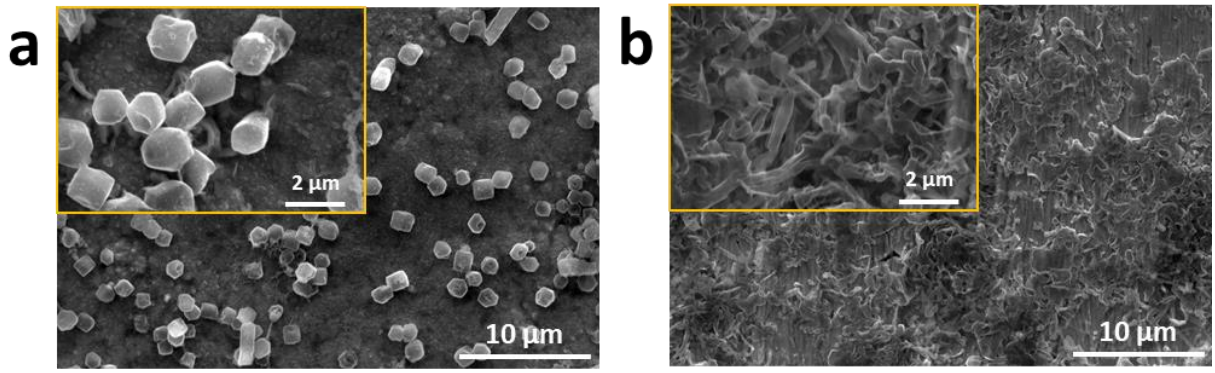

Figure 5.7 SEM images of 0.1 mAh cm^{-2} Li deposited on a, Fe/LiF nanocomposite, b, Cu, under 1 mA cm^{-2}.

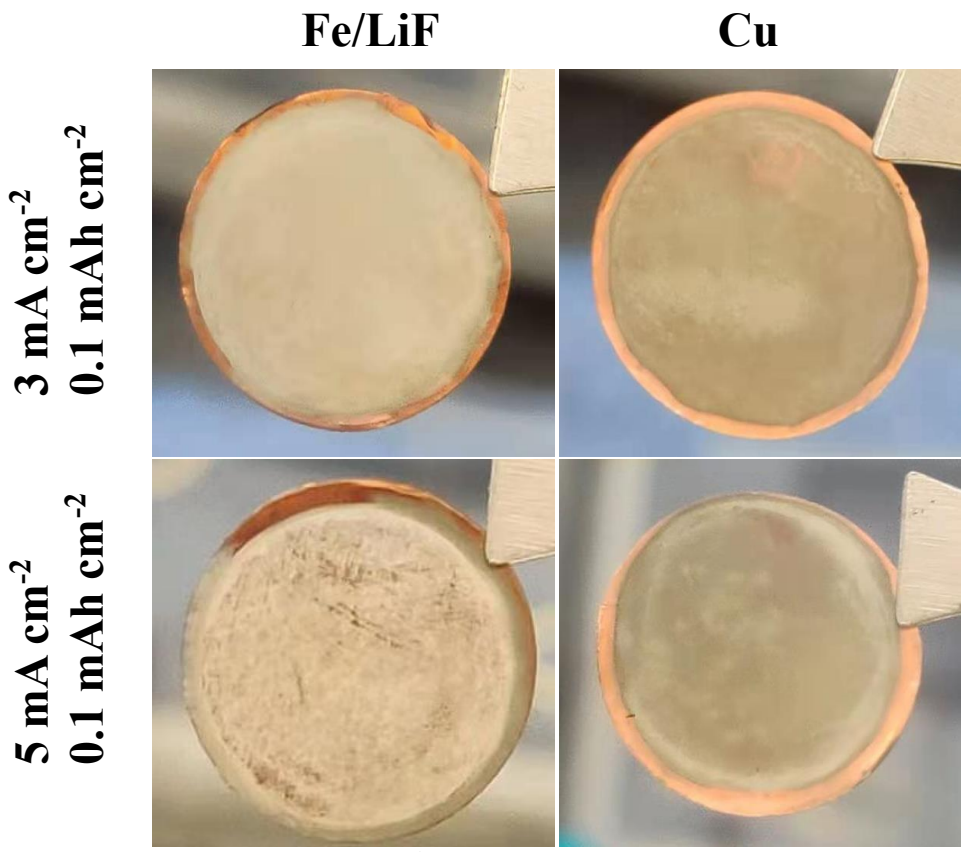

Figure 5.8 Optical images of 0.1 mAh cm^{-2} Li deposited on different substrate, under different current.

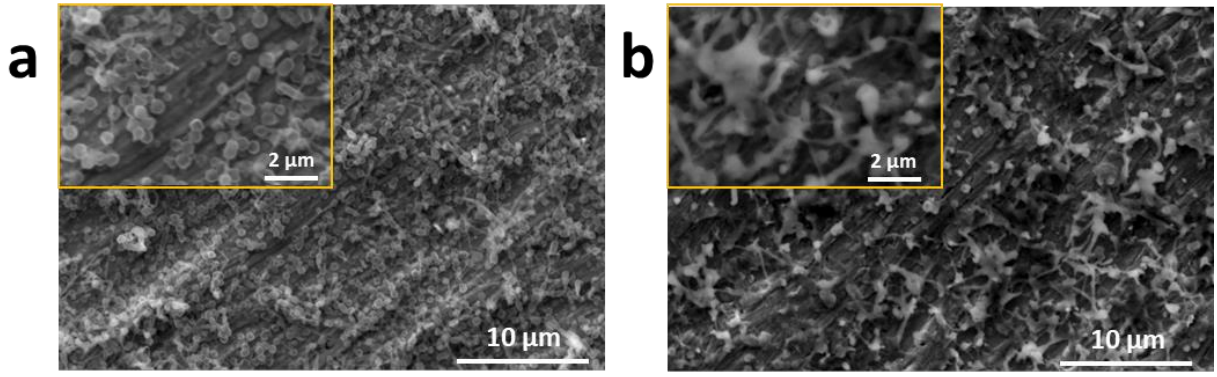

Figure 5.9 SEM images of 0.1 mAh cm^{-2} Li deposited on a, Fe/LiF nanocomposite, b, Cu, under 0.25 mA cm^{-2}, at -40 °C.

We performed cryogenic TEM characterization of the Fe/LiF nanocomposite substrate and the as deposited Li crystals in their native states (see methods for details). Figure 5.10 a-c show the cryo-TEM imaging and diffraction of the FeF_3 thin film after electrochemical Li deposition.

Dark-field cryoEM image shows the formation of nano-sized domains in the substrate. The small nanoscale polycrystalline structure is verified by atomic-resolution cryo-TEM imaging. The atomic-resolution image shows the formation of supranano BCC Fe nanoparticles as well as the presence of disordered/amorphous domains (Figure 5.10b). The electron diffraction pattern shows the reacted Fe/LiF nanocomposite substrate has Bragg rings corresponding to BCC Fe. The halo pattern likely corresponds to the disordered or amorphous materials which could originate from disordered Fe or LiF. Figure 5.10d, e and f show the cryo-imaging of the plated Li crystal. Figure 5.10d shows the energy dispersive X-ray spectroscopic (EDS) images showing the deposited Li crystal has thin, conformal SEI film that contains C, O, F, S and N. Figure 5.10e and the inset show that the hexagonal-shaped Li crystal indeed is a single crystal—both the high-resolution cryo-TEM image and the diffraction pattern show a perfect hexagonal symmetry down the [111] zone axis. We further performed cryo-electron tomography to image the 3D shape of the Li crystal. The 3D reconstruction in Figure 5.10f shows the single-crystalline Li metal has a near elongated hexagonal bipyramidal shape mainly terminated with low-energy {110} facets.

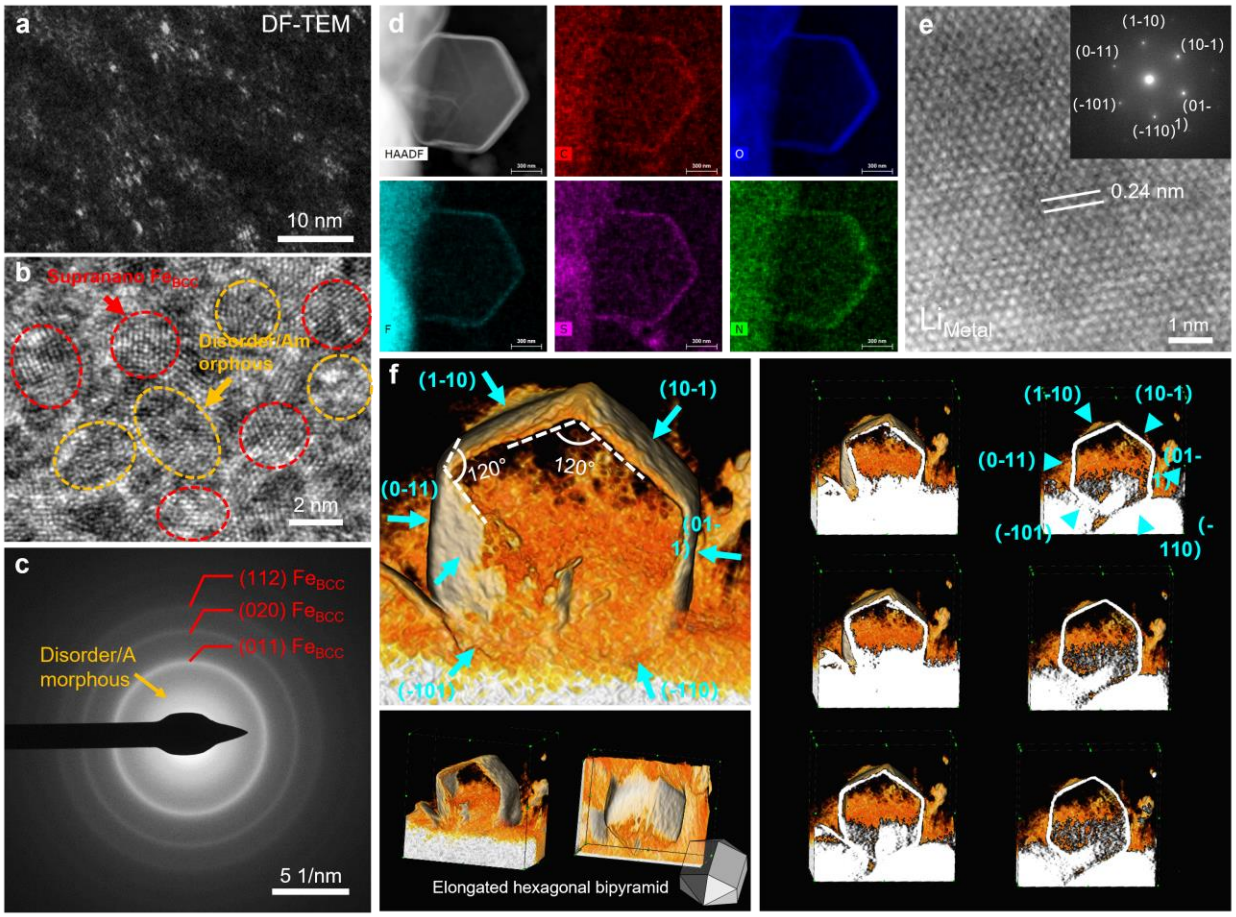

Figure 5.10 Cryo-transmission electron microscopy (cryo-TEM) imaging and crystallographic analysis of the single-crystalline Li crystals. **a,** Dark-field TEM (DF-TEM) image showing the formation of nano-sized domains in the substrate after electrochemical Li deposition. **b,** Atomic-resolution TEM image showing the formation of supranano (<10nm) body-centered cubic (BCC) Fe nanoparticles (red circles) and disordered/amorphous domains (orange circles). **c,** Electron diffraction pattern (EDP) of the reacted substrate showing diffraction rings correspond to BCC Fe and halo pattern corresponding to amorphous phase. **d,** Energy dispersive X-ray spectroscopy (EDS) maps of C, O, F, S, N. The result shows that a thin layer of uniform solid-electrolyte interface (SEI) forms on the surface the Li crystal. **e,** Atomic-resolution TEM image of the Li_{Metal} obtained along the [111] zone axis. The EDP in the inset shows that the Li crystal in **d** is perfectly single-crystalline. **f,** 3D imaging and crystallographic analysis of the hexagonal-shaped single-crystalline Li_{Metal} in **d** by cryo-TEM tomography. The single-crystalline Li metal has a near elongated hexagonal bipyramidal shape mainly terminated with low-energy {110} facets. The cross-section analysis in the right panel highlights the elongated prism side surfaces corresponding to the {110} planes of BCC Li_{Metal}.

Morphological characterization of plated Li

Though we have shown dramatically different morphology under 0.1 mAh cm^{-2} capacity, such a low-capacity deposition is not practically useful. To study whether the Li regulation effect still persists when the layer grows thicker, we gradually increased the deposition capacity from 0.1 to 3 mAh cm^{-2}. The top view SEM images are shown in Figure 5.11. As the capacity increased from 0.1 to 0.5 mAh cm^{-2}, the hexagonal Li crystals were gradually merging to form a substrate with uniform Li orientation. Meanwhile, another layer of Li started to be plated on top of the smooth Li substrate, which appears to be dendrite-free and dense. The uniform Li deposition continued as capacity increased from 0.5 to 3 mAh cm^{-2}. On the contrary, Li deposits on Cu started with randomly oriented Li filaments. As deposition capacity increased from 0.1 to 1 mAh cm^{-2}, the filaments grew thicker but did not vanish. Only when 3 mAh cm^{-2} deposited, the Li merged into granular deposits. The different Li morphology evolution behavior indicates that the substrate effect can still be perceived as the deposition continues.

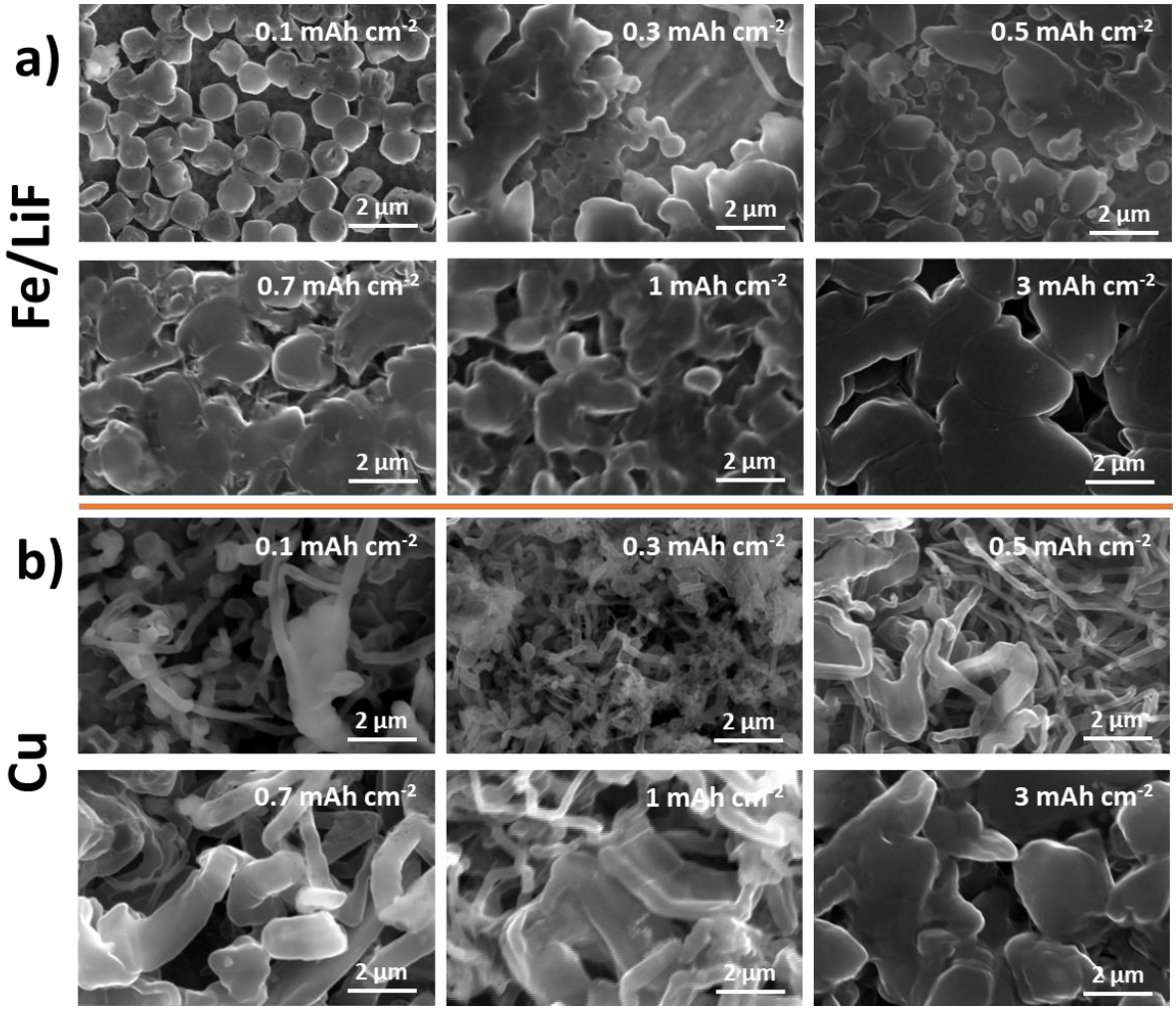

Figure 5.11 Top view SEM images of Li deposited on different substrates, under the same current (3 mA cm^{-2}), with different capacity.

SEM images of 1 mAh cm^{-2} Li deposited under different current densities, ranging from 0.5 to 5 mA cm^{-2}, were taken to systematically study the substrate influence on the Li morphology and how it is affected by the current density. Figure 5.12 and 5.13 show the cross-sectional SEM images of the deposited Li, where significant thickness differences were observed between the Fe/LiF nanocomposite and Cu sample, especially at high current density. The thickness of Li layer on Fe/LiF nanocomposite, under 0.5, 1, 3, and 5 mA cm^{-2}, were measured to be 6.1, 6.7, 7.3, and 8.7 µm, while the ones on Cu are 8.5, 10.1 15.8, and 17.8 µm, respectively. The theoretical

thickness of 1 mAh cm^{-2} Li is 4.85 μm, assuming it is fully dense. The fact that Li deposited on Cu, especially at high current, is more than three times thicker than the fully dense Li indicates its high porosity. To better reveal the porosity difference, cryo-FIB SEM was utilized to cut the Li plated at 3 mA cm^{-2} on different substates. The cryo-FIB milling process very well reserved the Li morphology, allowing us to image the cross-sectional interface without too much damaging. As shown in Figure 5.12b, Li deposited on Fe/LiF nanocomposite shows a columnar structure with some sub-micron pores distributed in the Li layer. On the contrary, few μm size interconnected pores were observed in Li plated on Cu. The FIB-SEM visually illustrated how Li was packed differently on different substrates. How the deposition capacity affects the porosity was illustrated in Figure 5.14, where the current density was kept at 3 mA cm^{-2}, but the capacity was varied from 0.3 to 9 mAh cm^{-2}. It was found that the Li plated on Fe/LiF nanocomposite is denser than the Cu counterpart, independent of the deposition amount. To better visualize the porosity difference and evolution as current or capacity increased, in Figure 5.12c and d, we summarized the thickness data of Li layer deposited under different current densities (0.5 to 5 mA cm^{-2}, maintaining the same capacity, 1 mAh cm^{-2}) and capacity (0.3 to 9 mAh cm^{-2}, maintaining the same current density, 3 mA cm^{-2}). The yellow color dashed lines represent the thickness of fully dense Li deposits. The data clearly show that no matter what current or capacity is, the Li plated on Fe/LiF nanocomposite is always much denser than that on Cu. The SEM images we used to get the thickness information are included in Figure 5.12a, 5.13, and 5.14. In addition to side-view observations, we also investigated the top view morphology. SEM images of 1 mAh cm^{-2} Li deposited in 0.5, 1, 3, 5 mA cm^{-2} are shown in Figure 5.15. It is quite clear that the Li plated on Cu shows more dendritic morphology than the Fe/LiF nanocomposite, especially under high current density, which agrees with our cross-sectional observations.

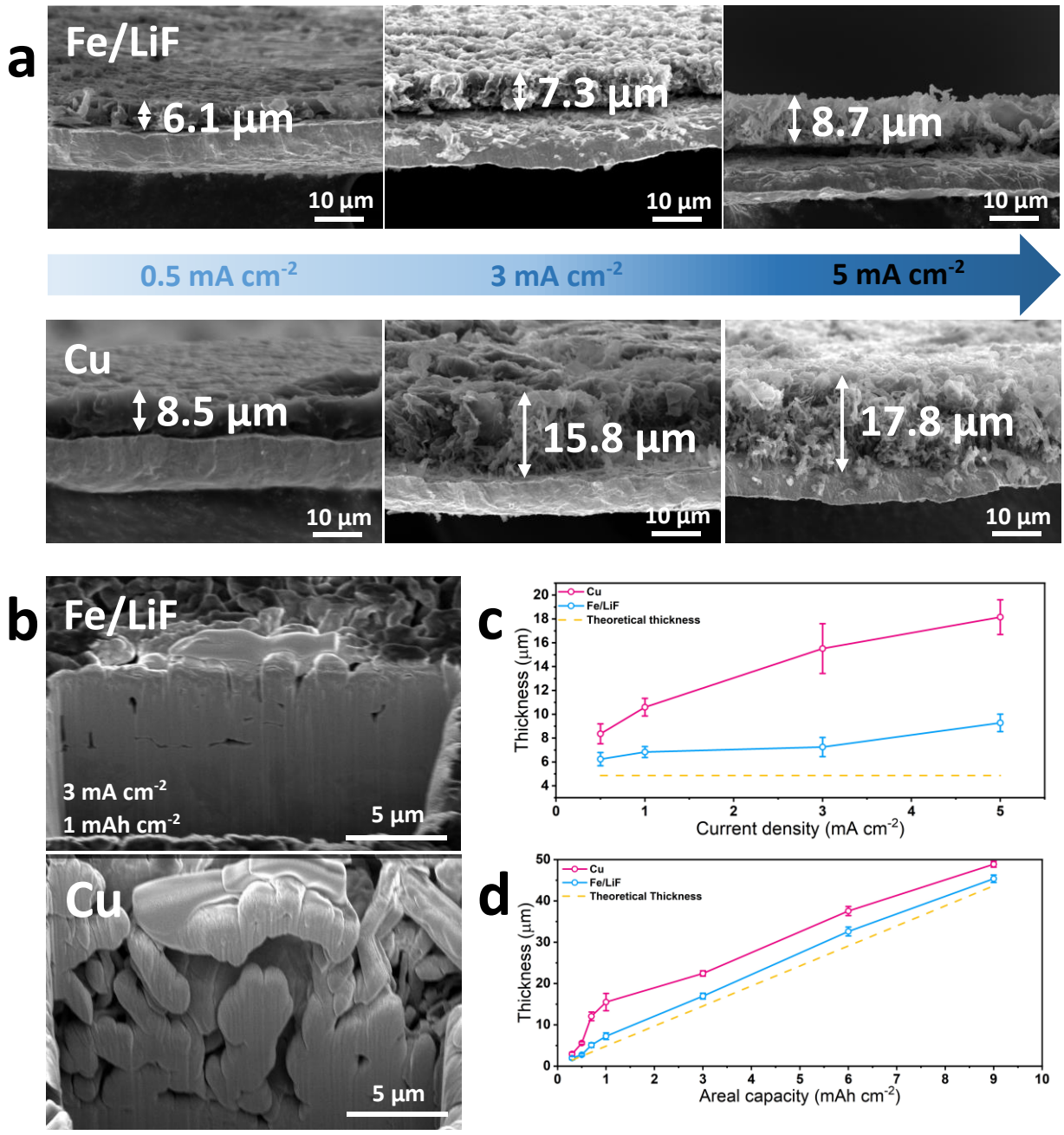

Figure 5.12 Cross-sectional morphology and thickness of the deposited Li layer. a, SEM images of 1 mAh cm^{-2} Li plated on Fe/LiF nanocomposite and Cu substrate, under 0.5, 3, 5 mA cm^{-2}. b, Cryo-FIB-SEM images of 1 mAh cm^{-2} Li deposited on Fe/LiF nanocomposite and Cu substrate under 3 mA cm^{-2}. c, Summarized thickness data of 1 mAh cm^{-2} Li deposited on Fe/LiF nanocomposite and Cu substrate under different current. d. Summarized thickness data of different amount of Li deposited on Fe/LiF nanocomposite and Cu substrate under 3 mA cm^{-2}.

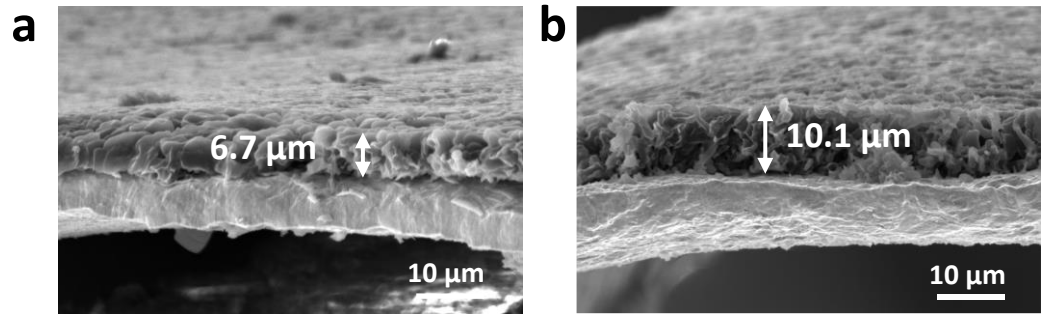

Figure 5.13 SEM images of 1 mAh cm^{-2} Li morphology under 1 mA cm^{-2}.

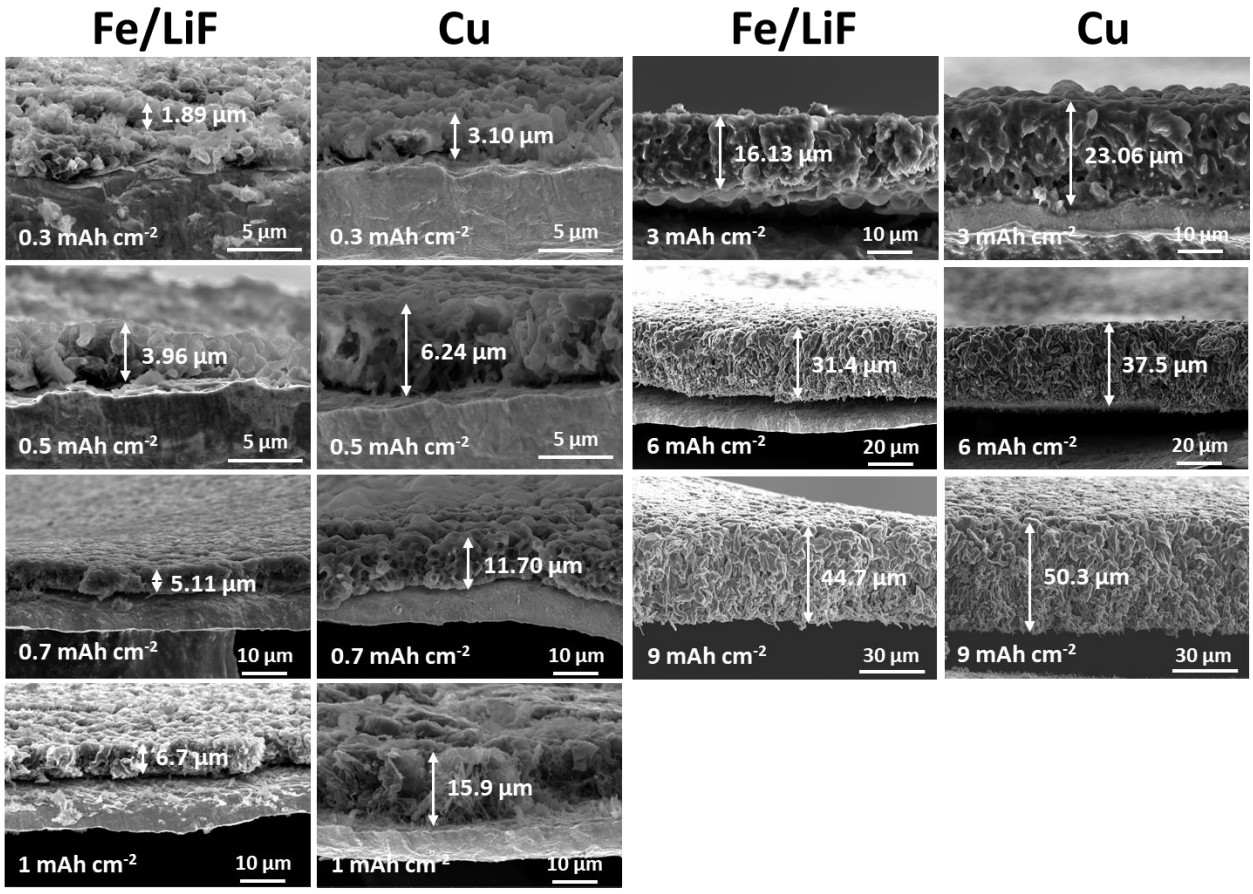

Figure 5.14 Cross-section SEM images of Li deposited under 3 mA cm^{-2}, different capacity.

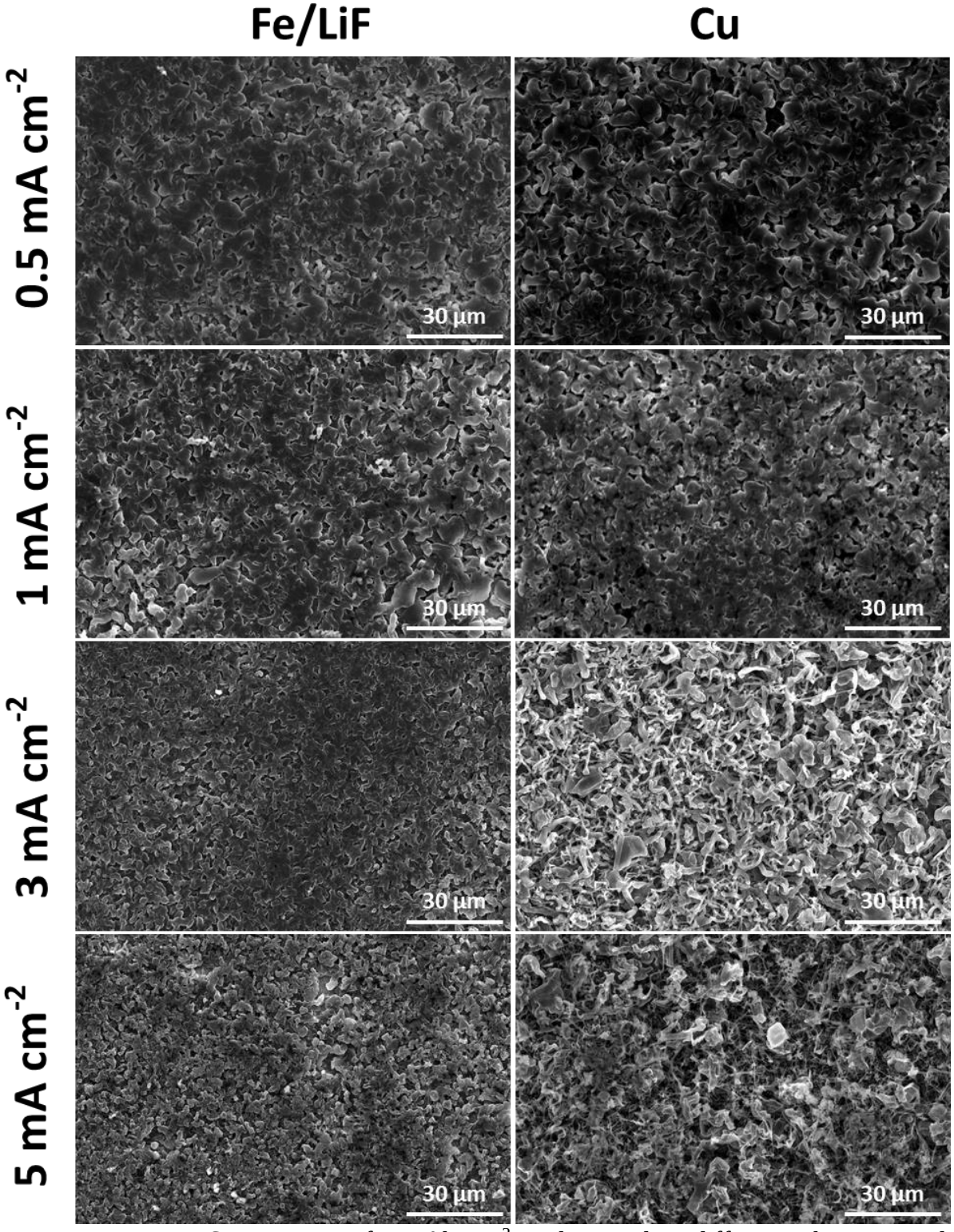

Figure 5.15 Top view SEM images of 1 mAh cm^{-2} Li deposited on different substrates, under different current (0.5-5 mA cm^{-2}).

Half cell and full cell performance

By far, we have shown that the Fe/LiF nanocomposite significantly tuned the nucleation behavior, and the smooth initial deposition led to much-improved morphology and reduced porosity in the following deposition. In principle, better morphology would result in superior cycling performance. Li||Cu or Li||Fe/LiF nanocomposite half cells were constructed to compare the cyclability. Figure 5.16 shows the coulombic efficiency (CE) data of half cells tested under different conditions, with the voltage profiles as the inset. 3 and 5 mA cm^{-2} were chosen to cycle the batteries because of the significant morphological differences observed between the Fe/LiF nanocomposite and Cu samples under such conditions. Lower current density cycling data is included in Figure 5.17. In addition to the current variation, the cycling capacity is also alternated between 1 and 3 mAh cm^{-2}, to demonstrate the applicability of Fe/LiF nanocomposite in different conditions. Figure 5.16a and b show the cycling performance of cells tested under 3 mA cm^{-2} current, 1 or 3 mAh cm^{-2} capacity. Remarkable long cycle life of the Fe/LiF nanocomposite cell was observed (> 1000, and > 300 cycles), while the Cu cells shorted quite early due to the exceptionally high current. The Cu cell performance deteriorated significantly when the current increased to 5 mA cm^{-2}. Cu cell shorted at 113^{th} and 2^{nd} cycle when 1 and 3 mAh cm^{-2} Li was cycled, respectively, while the Fe/LiF nanocomposite cell delivered 600 and 80 stable cycles under such challenging conditions. We also noticed that the average CE of the Cu cell is only 97.32%, when 1 mAh cm^{-2} Li was cycled at 5 mA cm^{-2}. However, no matter what conditions were used, the average CE for the Fe/LiF nanocomposite cell was always > 99%. The superior cycling performance and coulombic efficiency of Fe/LiF nanocomposite cell suggest its promising application in the full cell.

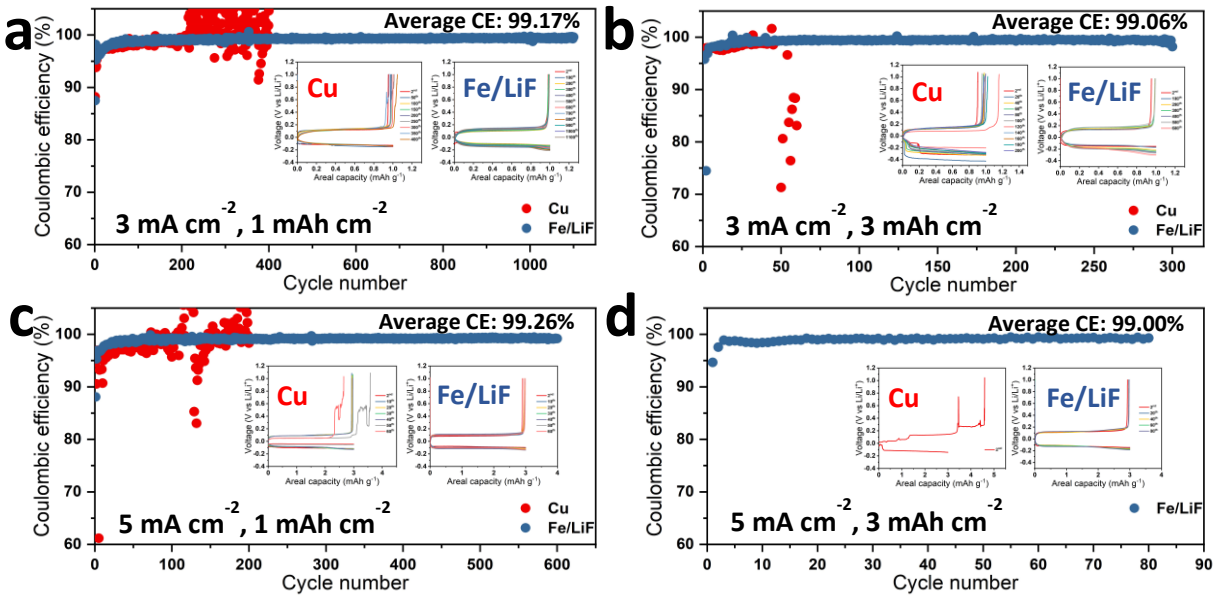

Figure 5.16 Electrochemical performance of half-cell with different substrates. Coulombic efficiency versus cycle number of Li||Cu or Fe/LiF nanocomposite cell under different conditions, a, 3 mA cm^{-2}, 1 mAh cm^{-2}; b, 3 mA cm^{-2}, 3 mAh cm^{-2}; c, 5 mA cm^{-2}, 1 mAh cm^{-2}; d, 5 mA cm^{-2}, 3 mAh cm^{-2}. Voltage profiles are presented in the figure insets.

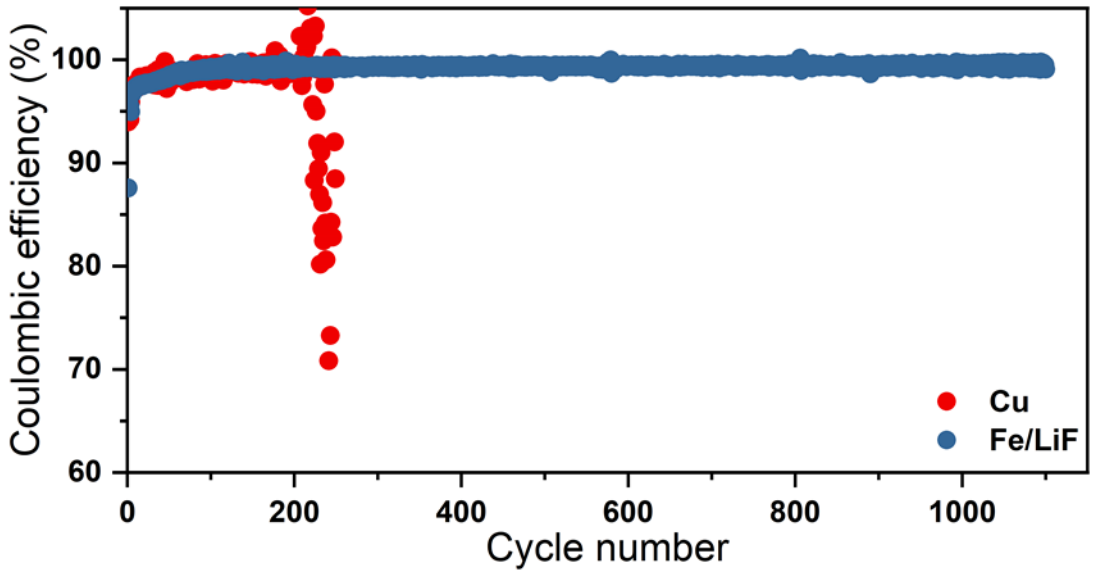

Figure 5.17. Electrochemical performance of half-cell with different substrates. Coulombic efficiency versus cycle number of Li||Cu or FeF_3 cell under 1 mA cm^{-2}, 1 mAh cm^{-2}.

We further investigated the performance of Fe/LiF nanocomposite substrate in a full cell, which comprised an NMC811 cathode with > 3 mAh cm^{-2} areal capacity and a Cu or Fe/LiF nanocomposite modified Cu film with pre-deposited Li. Previous reports have demonstrated that a low N/P (negative/positive) ratio and lean electrolyte conditions needed to be satisfied to deliver a competitive cell-level energy density.[6,79] Therefore, we deposited only 3 mAh cm^{-2} Li on Fe/LiF nanocomposite and Cu, which translated to an N/P ratio of 1. The amount of electrolyte added is 3 g Ah^{-1}. (only ~ 10 µL per coin cell) In addition to the above-mentioned challenging condition, NMC811 full cells were tested under 1C rate, which is 3 mA cm^{-2}. Figure 5.18 shows the cycling performance comparison of the full cell. The Cu cell only lasted for 20 cycles before quick degradation. The cell capacity decayed from > 3 mAh cm^{-2} to almost 0 within a few cycles. The degradation symptom is similar to some lean electrolyte cells reported in the literature, which was attributed to electrolyte depletion.[7,79,114] It is worth noting that such a phenomenon is typically observed in LMB with carbonate electrolyte while not in the Li-friendly ether electrolyte system. However, in our test, the high current density deposition poses a great challenge to the anode side, which results in such a catastrophic degradation. On the contrary, the Fe/LiF nanocomposite cell showed stable cycling for 130 cycles before it decayed to 80% of its original capacity. To figure out the origin of the significantly different cyclability, cells were disassembled after 20 cycles to observe the Li morphology. As shown in Figure 5.18, top-view SEM images showed dramatically different morphology. The Li on the Fe/LiF nanocomposite substrate comprises few-micron size Li ‘chunks’, while the Cu showed extremely porous and mossy morphology. The cross-sectional images also revealed a great difference in the Li layer thickness. The Li on Fe/LiF nanocomposite is 25.9 µm, while the Li on Cu is 59.1 µm. The difference indicates that the substrate effect persists after cycles. The voltage profile, as shown in Figure 5.19 also implies that with the help of Fe/LiF

the Li impedance evolves much slowly. In addition to the high areal loading full cell, NMC811 cathode with 1.5 mAh cm^{-2} areal loading was also tested under similar conditions, 1x excess Li and 1C rate, as shown in Figure 5.20 and 5.21, where similar phenomenon was observed. The above results demonstrate that when combined with lean electrolyte, the porosity difference resulted in significantly different cyclability.

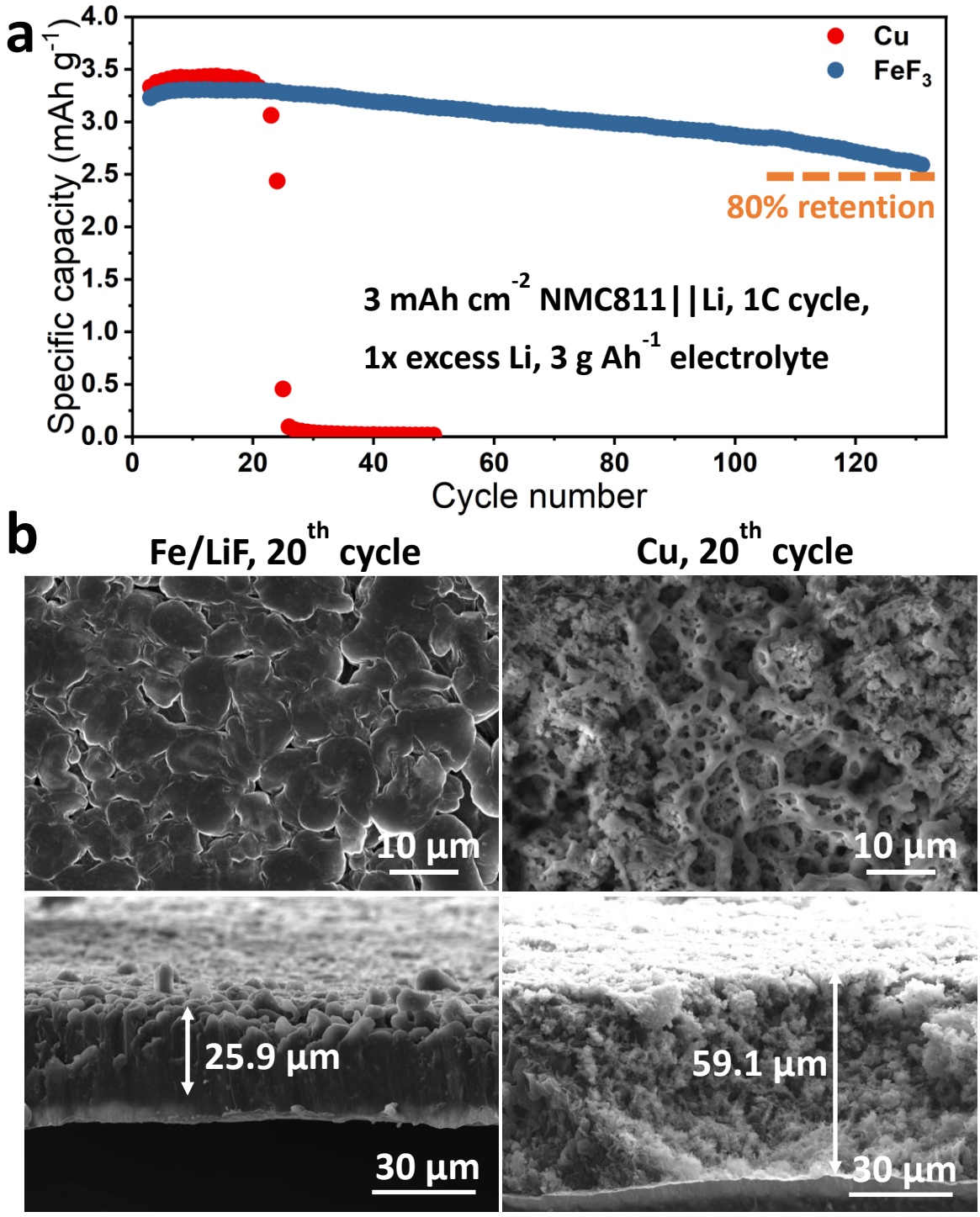

Figure 5.18 Electrochemical performance of full cell with different substrates. a. capacity retention of full cell with 3 mAh cm^{-2} NMC811 as the cathode, 3 mAh cm^{-2} Li plated on different substrates as the anode. 3 g Ah^{-1} electrolyte was added to each cell. CCCV cycling was performed at 1C rate, with the voltage window of 2.8-4.4 V.

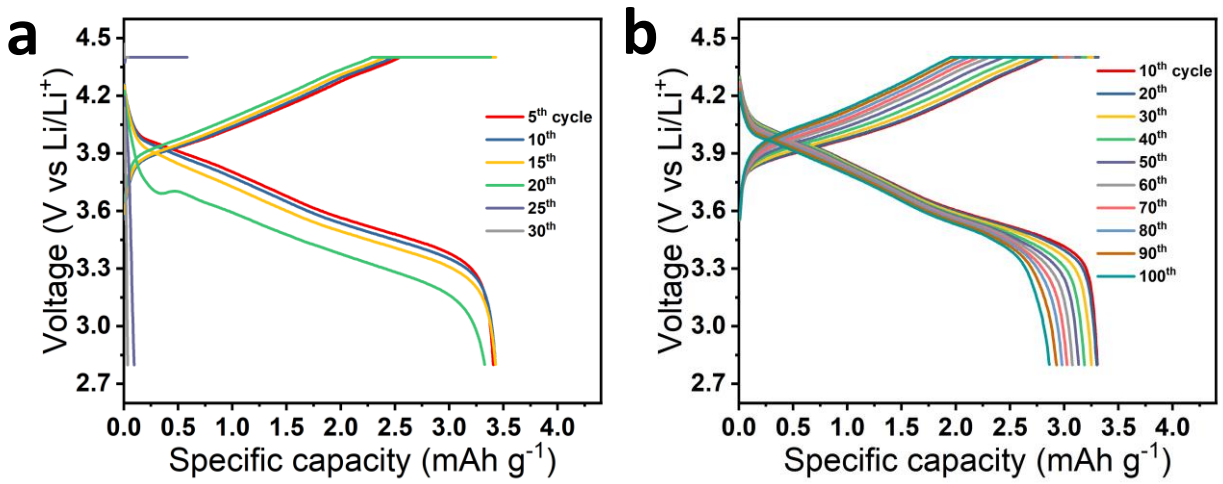

Figure 5.19 Voltage profiles for 3 mAh NMC811 full cell with different anodes. a, 3 mAh cm^{-2} Li deposited on Cu. b, 3 mAh cm^{-2} Li deposited on Fe/LiF nanocomposite. Cells were cycled under 1C rate, between 2.8 and 4.4 V.

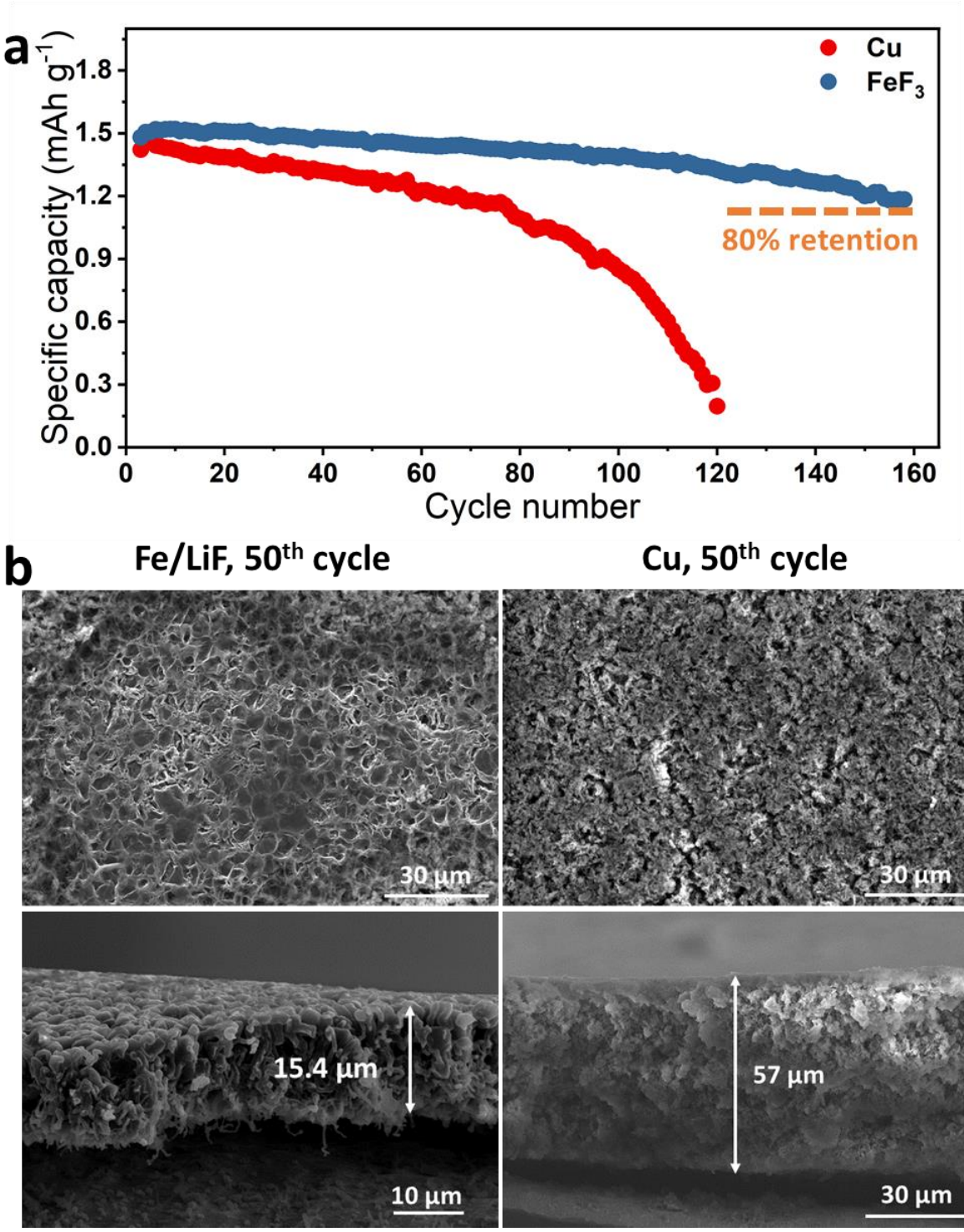

Figure 5.20 Electrochemical performance of full cell with different substrates. a. capacity retention of full cell with 1.5 mAh cm^{-2} NMC811 as the cathode, Li plated on different substrates as the anode. 3 g Ah-1 electrolyte was added to each cell. Cells were cycled at 1C rate, with the voltage window of 2.8-4.4 V.

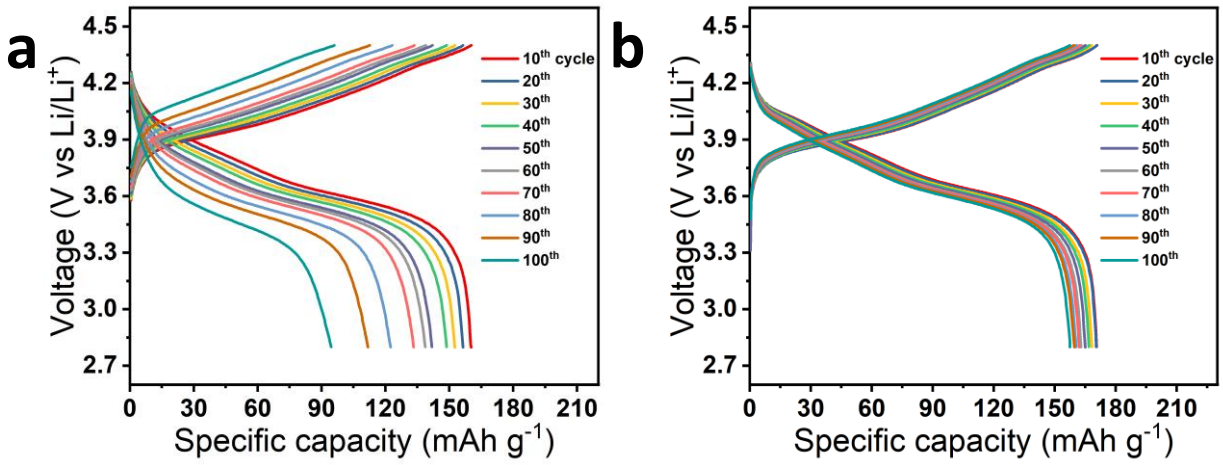

Figure 5.21 Voltage profiles for 1.5 mAh cm^{-2} NMC811 full cell with different anodes. a, 1.5 mAh cm^{-2} Li deposited on Cu. b, 1.5 mAh cm^{-2} Li deposited on Fe/LiF nanocomposite. Cells were cycled under 1C rate, between 2.8 and 4.4 V.

5.4 Conclusion

In summary, we have demonstrated that tuning the substrate notably affected the nucleation behavior of Li, by comparing the initial growth of Li on bare Cu or Fe/LiF nanocomposite modified Cu. Hexagonal single crystal Li nucleation was observed, which led to remarkably improved morphology and reduced porosity in the following Li plating. Leveraging the dendrite-free Li deposition, half cells constructed with Fe/LiF nanocomposite showed > 1000 and > 600 cycles under 3 and 5 mA cm^{-2}, respectively. Compared to the Cu cell, significant cyclability improvement was observed in full cell tests with lean electrolyte (3 g Ah^{-1}) and 1C rate cycling, which resulted from the denser Li deposition. This work presents a novel strategy to tune the Li nucleation behavior and its consequent Li deposition, which is of great scientific and practical importance.

Acknowledgements

Chapter 5, in full is currently being prepared for submission for publication of the material, **Zhaohui Wu**, Chunyang Wang, Haodong Liu, Shen Wang, Sicen Yu, Xing Xing, John Holoubek,

Huolin Xin, Ping Liu. The dissertation author was the primary researcher and author of this material.

REFERENCES

(1) Duffner, F.; Kronemeyer, N.; Tübke, J.; Leker, J.; Winter, M.; Schmuch, R. Post-Lithium-Ion Battery Cell Production and Its Compatibility with Lithium-Ion Cell Production Infrastructure. *Nat. Energy* **2021**, *6* (2), 123–134.

(2) Duffner, F.; Wentker, M.; Greenwood, M.; Leker, J. Battery Cost Modeling : A Review and Directions for Future Research. *Renew. Sustain. Energy Rev.* **2020**, *127* (May), 109872.

(3) Mauler, L.; Duffner, F.; Zeier, W. G. Environmental Science Battery Cost Forecasting : A Review of Methods and Results with an Outlook to 2050 †. **2021**, 4712–4739.

(4) Cano, Z. P.; Banham, D.; Ye, S.; Hintennach, A.; Lu, J.; Fowler, M.; Chen, Z. Batteries and Fuel Cells for Emerging Electric Vehicle Markets. *Nat. Energy* **2018**, *3* (April), 279–289.

(5) Abraham, K. M. Prospects and Limits of Energy Storage in Batteries. *J. Phys. Chem. Lett.* **2015**, *6* (5), 830–844.

(6) Liu, J.; Bao, Z.; Cui, Y.; Dufek, E. J.; Goodenough, J. B.; Khalifah, P.; Li, Q.; Liaw, B. Y.; Liu, P.; Manthiram, A.; Meng, Y. S.; Subramanian, V. R.; Toney, M. F.; Viswanathan, V. V; Whittingham, M. S.; Xiao, J.; Xu, W.; Yang, J.; Yang, X.; Zhang, J. Pathways for Practical High-Energy Long-Cycling Lithium Metal Batteries. *Nat. Energy* **2019**, *4* (March), 180–186.

(7) Niu, C.; Lee, H.; Chen, S.; Li, Q.; Du, J.; Xu, W.; Zhang, J. G.; Whittingham, M. S.; Xiao, J.; Liu, J. High-Energy Lithium Metal Pouch Cells with Limited Anode Swelling and Long Stable Cycles. *Nat. Energy* **2019**, *4* (7), 551–559.

(8) Campbell, G. A. The Cobalt Market Revisited. *Miner. Econ.* **2020**, *33* (1–2), 21–28.

(9) Liu, W.; Oh, P.; Liu, X.; Lee, M. J.; Cho, W.; Chae, S.; Kim, Y.; Cho, J. Nickel-Rich Layered Lithium Transition-Metal Oxide for High-Energy Lithium-Ion Batteries. *Angew. Chemie - Int. Ed.* **2015**, *54* (15), 4440–4457.

(10) Manthiram, A. A Reflection on Lithium-Ion Battery Cathode Chemistry. *Nat. Commun.* **2020**, *11* (1), 1–9.

(11) Wu, F.; Yushin, G. Conversion Cathodes for Rechargeable Lithium and Lithium-Ion Batteries. *Energy Environ. Sci.* **2017**, *10* (2), 435–459.

(12) Wang, J.; Yang, J.; Xie, J.; xu naixin. A Novel Conductive Polymer ± Sulfur Composite. *Adv. Mater.* **2002**, *050* (13), 963–965.

(13) Ahmed, M. S.; Lee, S.; Agostini, M.; Jeong, M. G.; Jung, H. G.; Ming, J.; Sun, Y. K.; Kim, J.; Hwang, J. Y. Multiscale Understanding of Covalently Fixed Sulfur–Polyacrylonitrile Composite as Advanced Cathode for Metal–Sulfur Batteries. *Adv. Sci.* **2021**, *8* (21), 1–34.

(14) Xiang, J.; Guo, Z.; Yi, Z.; Zhang, Y.; Yuan, L.; Cheng, Z.; Shen, Y.; Huang, Y. Facile

Synthesis of Sulfurized Polyacrylonitrile Composite as Cathode for High-Rate Lithium-Sulfur Batteries. *J. Energy Chem.* **2020**, *49*, 161–165.

(15) Chen, W.-J.; Li, B.-Q.; Zhao, C.-X.; Zhao, M.; Yuan, T.-Q.; Sun, R.-C.; Huang, J.-Q.; Zhang, Q. Electrolyte Regulation towards Stable Lithium Metal Anode in Lithium–Sulfur Batteries with Sulfurized Polyacrylonitrile Cathode. *Angew. Chemie* **2019**, ange.201912701.

(16) Liu, H.; Holoubek, J.; Zhou, H.; Chen, A.; Chang, N.; Wu, Z.; Yu, S.; Yan, Q.; Xing, X.; Li, Y.; Pascal, T. A.; Liu, P. Ultrahigh Coulombic Efficiency Electrolyte Enables Li||SPAN Batteries with Superior Cycling Performance. *Mater. Today* **2021**, *42* (February), 17–28.

(17) Chen, J.; Zhang, H.; Yang, H.; Lei, J.; Naveed, A.; Yang, J.; Nuli, Y.; Wang, J. Towards Practical Li–S Battery with Dense and Flexible Electrode Containing Lean Electrolyte. *Energy Storage Mater.* **2020**, *27*, 307–315.

(18) Cheng, X. B.; Zhang, R.; Zhao, C. Z.; Zhang, Q. Toward Safe Lithium Metal Anode in Rechargeable Batteries: A Review. *Chem. Rev.* **2017**, *117* (15), 10403–10473.

(19) Zheng, J.; Kim, M. S.; Tu, Z.; Choudhury, S.; Tang, T.; Archer, L. A. Regulating Electrodeposition Morphology of Lithium: Towards Commercially Relevant Secondary Li Metal Batteries. *Chem. Soc. Rev.* **2020**, *49* (9), 2701–2750.

(20) Cao, X.; Jia, H.; Xu, W.; Zhang, J.-G. Review—Localized High-Concentration Electrolytes for Lithium Batteries. *J. Electrochem. Soc.* **2021**, *168* (1), 010522.

(21) Niu, C.; Liu, D.; Lochala, J. A.; Anderson, C. S.; Cao, X.; Gross, M. E.; Xu, W.; Zhang, J. G.; Whittingham, M. S.; Xiao, J.; Liu, J. Balancing Interfacial Reactions to Achieve Long Cycle Life in High-Energy Lithium Metal Batteries. *Nat. Energy* **2021**, *6* (7), 723–732.

(22) Gao, Y.; Yan, Z.; Gray, J. L.; He, X.; Wang, D.; Chen, T.; Huang, Q.; Li, Y. C.; Wang, H.; Kim, S. H.; Mallouk, T. E.; Wang, D. Polymer–Inorganic Solid–Electrolyte Interphase for Stable Lithium Metal Batteries under Lean Electrolyte Conditions. *Nat. Mater.* **2019**, *18* (4), 384–389.

(23) Li, Q.; Pan, H.; Li, W.; Wang, Y.; Wang, J.; Zheng, J.; Yu, X.; Li, H.; Chen, L. Homogeneous Interface Conductivity for Lithium Dendrite-Free Anode. *ACS Energy Lett.* **2018**, *3* (9), 2259–2266.

(24) Whittingham, M. S. Lithium Batteries and Cathode Materials. *Chem. Rev.* **2004**, *104* (10), 4271–4301.

(25) Zhao, W.; Zheng, J.; Zou, L.; Jia, H.; Liu, B.; Wang, H.; Engelhard, M. H.; Wang, C.; Xu, W.; Yang, Y.; Zhang, J. G. High Voltage Operation of Ni-Rich NMC Cathodes Enabled by Stable Electrode/Electrolyte Interphases. *Adv. Energy Mater.* **2018**, *8* (19).

(26) Gao, H.; Zeng, X.; Hu, Y.; Tileli, V.; Li, L.; Ren, Y.; Meng, X.; Maglia, F.; Lamp, P.; Kim, S. J.; Amine, K.; Chen, Z. Modifying the Surface of a High-Voltage Lithium-Ion Cathode.

ACS Appl. Energy Mater. **2018**, *1* (5), 2254–2260.

(27) Li, H.; Liu, A.; Zhang, N.; Wang, Y.; Yin, S.; Wu, H.; Dahn, J. R. An Unavoidable Challenge for Ni-Rich Positive Electrode Materials for Lithium-Ion Batteries. *Chem. Mater.* **2019**, *31* (18), 7574–7583.

(28) Sander, J. S.; Erb, R. M.; Li, L.; Gurijala, A.; Chiang, Y. M. High-Performance Battery Electrodes via Magnetic Templating. *Nat. Energy* **2016**, *1* (8), 1–7.

(29) Kuang, Y.; Chen, C.; Kirsch, D.; Hu, L. Thick Electrode Batteries: Principles, Opportunities, and Challenges. *Adv. Energy Mater.* **2019**, *9* (33), 1–19.

(30) Kang, S. H.; Yoon, W. S.; Nam, K. W.; Yang, X. Q.; Abraham, D. P. Investigating the First-Cycle Irreversibility of Lithium Metal Oxide Cathodes for Li Batteries. *J. Mater. Sci.* **2008**, *43* (14), 4701–4706.

(31) Kang, S. H.; Abraham, D. P.; Yoon, W. S.; Nam, K. W.; Yang, X. Q. First-Cycle Irreversibility of Layered Li-Ni-Co-Mn Oxide Cathode in Li-Ion Batteries. *Electrochim. Acta* **2008**, *54* (2), 684–689.

(32) Zhang, S. S.; Xu, K.; Jow, T. R. Formation of Solid Electrolyte Interface in Lithium Nickel Mixed Oxide Electrodes during the First Cycling. *Electrochem. Solid-State Lett.* **2002**, *5* (5), 92–94.

(33) Kasnatscheew, J.; Evertz, M.; Streipert, B.; Wagner, R.; Klöpsch, R.; Vortmann, B.; Hahn, H.; Nowak, S.; Amereller, M.; Gentschev, A. C.; Lamp, P.; Winter, M. The Truth about the 1st Cycle Coulombic Efficiency of LiNi1/3Co1/3Mn1/3O2 (NCM) Cathodes. *Phys. Chem. Chem. Phys.* **2016**, *18* (5), 3956–3965.

(34) Zhou, H.; Xin, F.; Pei, B.; Whittingham, M. S. What Limits the Capacity of Layered Oxide Cathodes in Lithium Batteries? *ACS Energy Lett.* **2019**, *4* (8), 1902–1906.

(35) Grenier, A.; Reeves, P. J.; Liu, H.; Seymour, I. D.; Märker, K.; Wiaderek, K. M.; Chupas, P. J.; Grey, C. P.; Chapman, K. W. Intrinsic Kinetic Limitations in Substituted Lithium-Layered Transition-Metal Oxide Electrodes. *J. Am. Chem. Soc.* **2020**, *142* (15), 7001–7011.

(36) Liu, A.; Phattharasupakun, N.; Cormier, M. M.; zsoldos, E.; zhang, ning; lyle, erin; Arab, P.; Sawangphruk, M.; Dahn, J. R. Factors That Affect Capacity in the Low Voltage Kinetic Hindrance Region of Ni-Rich Positive Electrode Materials and Diffusion Measurements from a Reinvented Approach. *J. Electrochem. Soc.* **2021**.

(37) Xu, K. Nonaqueous Liquid Electrolytes for Lithium-Based Rechargeable Batteries. *Chem. Rev.* **2004**, *104* (10), 4303–4417.

(38) Wen, B.; Deng, Z.; Tsai, P. C.; Lebens-Higgins, Z. W.; Piper, L. F. J.; Ong, S. P.; Chiang, Y. M. Ultrafast Ion Transport at a Cathode–Electrolyte Interface and Its Strong Dependence on Salt Solvation. *Nat. Energy* **2020**, *5* (8), 578–586.

(39) Ven, A. Van Der; Ceder, G. Lithium Diffusion in Layered Li x CoO 2. *Electrochem. Solid-State Lett.* **2000**, *3* (7), 301–304.

(40) Fang, R.; Xu, J.; Wang, D. W. Covalent Fixing of Sulfur in Metal-Sulfur Batteries. *Energy Environ. Sci.* **2020**, *13* (2), 432–471.

(41) Zhang, X.; Chen, K.; Sun, Z.; Hu, G.; Xiao, R.; Cheng, H.-M.; Li, F. Structure-Related Electrochemical Performance of Organosulfur Compounds for Lithium-Sulfur Batteries. *Energy Environ. Sci.* **2020**.

(42) Rahman, M. A.; Wang, X.; Wen, C. High Energy Density Metal-Air Batteries: A Review. *J. Electrochem. Soc.* **2013**, *160* (10), A1759–A1771.

(43) Ponrouch, A.; Bitenc, J.; Dominko, R.; Lindahl, N.; Johansson, P.; Palacin, M. R. Multivalent Rechargeable Batteries. *Energy Storage Mater.* **2019**, *20* (April), 253–262.

(44) Liu, T.; Hu, H.; Ding, X.; Yuan, H.; Jin, C.; Nai, J.; Liu, Y.; Wang, Y.; Wan, Y.; Tao, X. 12 Years Roadmap of the Sulfur Cathode for Lithium Sulfur Batteries (2009–2020). *Energy Storage Mater.* **2020**, *30*, 346–366.

(45) Shi, L.; Bak, S.; Shadike, Z.; Wang, C. Reaction Heterogeneity in Practical High-Energy Lithium–Sulfur Pouch Cells. *Energy Environ. Sci.* **2020**.

(46) Ji, X.; Lee, K. T.; Nazar, L. F. A Highly Ordered Nanostructured Carbon-Sulphur Cathode for Lithium-Sulphur Batteries. *Nat. Mater.* **2009**, *8* (6), 500–506.

(47) Wang, J.; Yang, J.; Wan, C.; Du, K.; Xie, J.; Xu, N. Sulfur Composite Cathode Materials for Rechargeable Lithium Batteries. *Adv. Funct. Mater.* **2003**, *13* (6), 487–492.

(48) Tao, X.; Wan, J.; Liu, C.; Wang, H.; Yao, H.; Zheng, G.; Seh, Z. W.; Cai, Q.; Li, W.; Zhou, G.; Zu, C.; Cui, Y. Balancing Surface Adsorption and Diffusion of Lithium-Polysulfides on Nonconductive Oxides for Lithium-Sulfur Battery Design. *Nat. Commun.* **2016**, *7*.

(49) Mikhaylik, Y. V. U. S. Pat. 7,352,680. **2008**, *2* (12), U. S. Pat. 7,352,680.

(50) Adams, B. D.; Carino, E. V.; Connell, J. G.; Han, K. S.; Cao, R.; Chen, J.; Zheng, J.; Li, Q.; Mueller, K. T.; Henderson, W. A.; Zhang, J. G. Long Term Stability of Li-S Batteries Using High Concentration Lithium Nitrate Electrolytes. *Nano Energy* **2017**, *40* (September), 607–617.

(51) Shaibani, M.; Mirshekarloo, M. S.; Singh, R.; Easton, C. D.; Cooray, M. C. D.; Eshraghi, N.; Abendroth, T.; Dörfler, S.; Althues, H.; Kaskel, S.; Hollenkamp, A. F.; Hill, M. R.; Majumder, M. Expansion-Tolerant Architectures for Stable Cycling of Ultrahigh-Loading Sulfur Cathodes in Lithium-Sulfur Batteries. *Sci. Adv.* **2020**, *6* (1), eaay2757.

(52) Liu, H.; Holoubek, J.; Zhou, H.; Chen, A.; Chang, N.; Wu, Z.; Yu, S.; Yan, Q.; Xing, X.; Li, Y.; Pascal, T. A.; Liu, P. Ultrahigh Coulombic Efficiency Electrolyte Enables Li||SPAN Batteries with Superior Cycling Performance. *Mater. Today* **2020**, *xxx* (xx), 7–14.

(53) Wang, L.; He, X.; Li, J.; Chen, M.; Gao, J.; Jiang, C. Charge/Discharge Characteristics of Sulfurized Polyacrylonitrile Composite with Different Sulfur Content in Carbonate Based Electrolyte for Lithium Batteries. *Electrochim. Acta* **2012**, *72*, 114–119.

(54) Wang, J.; Yang, J.; Xie, J.; xu naixin. A Novel Conductive Polymer-Sulfur Composite Material for Rechargeable Lithium Batteries. *Adv. Mater.* **2002**, *050* (13), 963–965.

(55) Markevich, E.; Salitra, G.; Chesneau, F.; Schmidt, M.; Aurbach, D. Very Stable Lithium Metal Stripping-Plating at a High Rate and High Areal Capacity in Fluoroethylene Carbonate-Based Organic Electrolyte Solution. *ACS Energy Lett.* **2017**, *2* (6), 1321–1326.

(56) Zhang, Y.; Zhong, Y.; Shi, Q.; Liang, S.; Wang, H. Cycling and Failing of Lithium Metal Anodes in Carbonate Electrolyte. *J. Phys. Chem. C* **2018**, *122* (37), 21462–21467.

(57) Lv, D.; Zheng, J.; Li, Q.; Xie, X.; Ferrara, S.; Nie, Z.; Mehdi, L. B.; Browning, N. D.; Zhang, J. G.; Graff, G. L.; Liu, J.; Xiao, J. High Energy Density Lithium-Sulfur Batteries: Challenges of Thick Sulfur Cathodes. *Adv. Energy Mater.* **2015**, *5* (16).

(58) Zhang, Y. Z.; Liu, S.; Li, G. C.; Li, G. R.; Gao, X. P. Sulfur/Polyacrylonitrile/Carbon Multi-Composites as Cathode Materials for Lithium/Sulfur Battery in the Concentrated Electrolyte. *J. Mater. Chem. A* **2014**, *2* (13), 4652–4659.

(59) Zhang, S. S. Understanding of Sulfurized Polyacrylonitrile for Superior Performance Lithium/Sulfur Battery. *Energies* **2014**, *7* (7), 4588–4600.

(60) Xing, X.; Li, Y.; Wang, X.; Petrova, V.; Liu, H.; Liu, P. Cathode Electrolyte Interface Enabling Stable Li–S Batteries. *Energy Storage Mater.* **2019**, *21*, 474–480.

(61) Yang, H.; Guo, C.; Chen, J.; Naveed, A.; Yang, J.; Nuli, Y.; Wang, J. An Intrinsic Flame-Retardant Organic Electrolyte for Safe Lithium-Sulfur Batteries. *Angew. Chemie - Int. Ed.* **2019**, *58* (3), 791–795.

(62) Yin, L.; Wang, J.; Yu, X.; Monroe, C. W.; NuLi, Y.; Yang, J. Dual-Mode Sulfur-Based Cathode Materials for Rechargeable Li-S Batteries. *Chem. Commun.* **2012**, *48* (63), 7868–7870.

(63) Zhao, C.; Chen, W.; Zhao, M.; Song, Y.; Liu, J.; Li, B.; Yuan, T.; Chen, C.; Zhang, Q.; Huang, J. Redox Mediator Assists Electron Transfer in Lithium–Sulfur Batteries with Sulfurized Polyacrylonitrile Cathodes. *EcoMat* **2021**, *3* (1), 1–8.

(64) Holoubek, J.; Yu, M.; Yu, S.; Li, M.; Wu, Z.; Xia, D.; Bhaladhare, P.; Gonzalez, M. S.; Pascal, T. A.; Liu, P.; Chen, Z. An All-Fluorinated Ester Electrolyte for Stable High-Voltage Li Metal Batteries Capable of Ultra-Low-Temperature Operation. *ACS Energy Lett.* **2020**, *5* (5), 1438–1447.

(65) Philippe, B.; Hahlin, M.; Edström, K.; Gustafsson, T.; Siegbahn, H.; Rensmo, H. Photoelectron Spectroscopy for Lithium Battery Interface Studies. *J. Electrochem. Soc.* **2016**, *163* (2), A178–A191.

(66) Frey, M.; Zenn, R. K.; Warneke, S.; Müller, K.; Hintennach, A.; Dinnebier, R. E.; Buchmeiser, M. R. Easily Accessible, Textile Fiber-Based Sulfurized Poly(Acrylonitrile) as Li/S Cathode Material: Correlating Electrochemical Performance with Morphology and Structure. *ACS Energy Lett.* **2017**, *2* (3), 595–604.

(67) Hu, Y.; Li, B.; Jiao, X.; Zhang, C.; Dai, X.; Song, J. Stable Cycling of Phosphorus Anode for Sodium-Ion Batteries through Chemical Bonding with Sulfurized Polyacrylonitrile. *Adv. Funct. Mater.* **2018**, *28* (23), 1–6.

(68) Feng, X.; Song, M. K.; Stolte, W. C.; Gardenghi, D.; Zhang, D.; Sun, X.; Zhu, J.; Cairns, E. J.; Guo, J. Understanding the Degradation Mechanism of Rechargeable Lithium/Sulfur Cells: A Comprehensive Study of the Sulfur-Graphene Oxide Cathode after Discharge-Charge Cycling. *Phys. Chem. Chem. Phys.* **2014**, *16* (32), 16931–16940.

(69) Li, X.; Banis, M.; Lushington, A.; Yang, X.; Sun, Q.; Zhao, Y.; Liu, C.; Li, Q.; Wang, B.; Xiao, W.; Wang, C.; Li, M.; Liang, J.; Li, R.; Hu, Y.; Goncharova, L.; Zhang, H.; Sham, T. K.; Sun, X. A High-Energy Sulfur Cathode in Carbonate Electrolyte by Eliminating Polysulfides via Solid-Phase Lithium-Sulfur Transformation. *Nat. Commun.* **2018**, *9* (1), 1–10.

(70) Fanous, J.; Wegner, M.; Grimminger, J.; Andresen, Ä.; Buchmeiser, M. R. Structure-Related Electrochemistry of Sulfur-Poly(Acrylonitrile) Composite Cathode Materials for Rechargeable Lithium Batteries. *Chem. Mater.* **2011**, *23* (22), 5024–5028.

(71) Wang, X.; Qian, Y.; Wang, L.; Yang, H.; Li, H.; Zhao, Y.; Liu, T. Sulfurized Polyacrylonitrile Cathodes with High Compatibility in Both Ether and Carbonate Electrolytes for Ultrastable Lithium–Sulfur Batteries. *Adv. Funct. Mater.* **2019**, *29* (39), 1–12.

(72) Wang, W.; Cao, Z.; Elia, G. A.; Wu, Y.; Wahyudi, W.; Abou-Hamad, E.; Emwas, A. H.; Cavallo, L.; Li, L. J.; Ming, J. Recognizing the Mechanism of Sulfurized Polyacrylonitrile Cathode Materials for Li-S Batteries and beyond in Al-S Batteries. *ACS Energy Lett.* **2018**, *3* (12), 2899–2907.

(73) Wei, S.; Ma, L.; Hendrickson, K. E.; Tu, Z.; Archer, L. A. Metal-Sulfur Battery Cathodes Based on PAN-Sulfur Composites. *J. Am. Chem. Soc.* **2015**, *137* (37), 12143–12152.

(74) Gorlin, Y.; Siebel, A.; Piana, M.; Huthwelker, T.; Jha, H.; Monsch, G.; Kraus, F.; Gasteiger, H. A.; Tromp, M. Operando Characterization of Intermediates Produced in a Lithium-Sulfur Battery. *J. Electrochem. Soc.* **2015**, *162* (7), A1146–A1155.

(75) Li, W.; Yao, H.; Yan, K.; Zheng, G.; Liang, Z.; Chiang, Y. M.; Cui, Y. The Synergetic Effect of Lithium Polysulfide and Lithium Nitrate to Prevent Lithium Dendrite Growth. *Nat. Commun.* **2015**, *6* (May).

(76) Farges, F.; Keppler, H.; A-M Flank; Lagarde, P. Sulfur K-Edge XANES Study of S Sorbed onto Volcanic Ashes. *J. Phys. Conf. Ser.* **2009**, *190*, 8–12.

(77) Ye, Y.; Kawase, A.; Song, M. K.; Feng, B.; Liu, Y. S.; Marcus, M. A.; Feng, J.; Cairns, E. J.; Guo, J.; Zhu H, J. X-Ray Absorption Spectroscopy Characterization of a Li/S Cell. *Nanomaterials* **2016**, *6* (1), 1–10.

(78) Dominko, R.; Patel, M. U. M.; Lapornik, V.; Vizintin, A.; Koželj, M.; N. Tušar, N.; Arčon, I.; Stievano, L.; Aquilanti, G. Analytical Detection of Polysulfides in the Presence of Adsorption Additives by Operando X-Ray Absorption Spectroscopy. *J. Phys. Chem. C* **2015**, *119* (33), 19001–19010.

(79) Niu, C.; Pan, H.; Xu, W.; Xiao, J.; Zhang, J. G.; Luo, L.; Wang, C.; Mei, D.; Meng, J.; Wang, X.; Liu, Z.; Mai, L.; Liu, J. Self-Smoothing Anode for Achieving High-Energy Lithium Metal Batteries under Realistic Conditions. *Nat. Nanotechnol.* **2019**, *14* (6), 594–601.

(80) Liu, H.; Wang, X.; Zhou, H.; Lim, H. D.; Xing, X.; Yan, Q.; Meng, Y. S.; Liu, P. Structure and Solution Dynamics of Lithium Methyl Carbonate as a Protective Layer for Lithium Metal. *ACS Appl. Energy Mater.* **2018**, *1* (5), 1864–1869.

(81) Liu, H.; Yue, X.; Xing, X.; Yan, Q.; Huang, J.; Petrova, V. A Scalable 3D Lithium Metal Anode. *Energy Storage Mater.* **2018**, *16* (September), 505–511.

(82) Chen, X.; Peng, L.; Wang, L.; Yang, J.; Hao, Z.; Xiang, J.; Yuan, K.; Huang, Y.; Shan, B.; Yuan, L.; Xie, J. Ether-Compatible Sulfurized Polyacrylonitrile Cathode with Excellent Performance Enabled by Fast Kinetics via Selenium Doping. *Nat. Commun.* **2019**, *10* (1), 1–9.

(83) Shen, Y.; Zhang, J.; Pu, Y.; Wang, H.; Wang, B.; Qian, J.; Cao, Y.; Zhong, F.; Ai, X.; Yang, H. Effective Chemical Prelithiation Strategy for Building a Silicon/Sulfur Li-Ion Battery. *ACS Energy Lett.* **2019**, *4* (7), 1717–1724.

(84) Liu, Y.; Haridas, A. K.; Cho, K. K.; Lee, Y.; Ahn, J. H. Highly Ordered Mesoporous Sulfurized Polyacrylonitrile Cathode Material for High-Rate Lithium Sulfur Batteries. *J. Phys. Chem. C* **2017**, *121* (47), 26172–26179.

(85) Yang, H.; Chen, J.; Yang, J.; Nuli, Y.; Wang, J. Dense and High Loading Sulfurized Pyrolyzed Poly (Acrylonitrile)(S@pPAN) Cathode for Rechargeable Lithium Batteries. *Energy Storage Mater.* **2020**, *31*, 187–194.

(86) Li, Y.; Zeng, Q.; Gentle, I. R.; Wang, D. W. Carboxymethyl Cellulose Binders Enable High-Rate Capability of Sulfurized Polyacrylonitrile Cathodes for Li-S Batteries. *J. Mater. Chem. A* **2017**, *5* (11), 5460–5465.

(87) Wu, Z.; Bak, S.; Shadike, Z.; Yu, S.; Hu, E.; Xing, X.; Du, Y.; Yang, X.; Liu, H.; Liu, P. Understanding the Roles of the Electrode / Electrolyte Interface for Enabling Stable Li ‖ Sulfurized Polyacrylonitrile Batteries. *ACS Appl. Mater. Interfaces* **2021**, *13* (27), 31733–31740.

(88) Ryou, M. H.; Kim, J.; Lee, I.; Kim, S.; Jeong, Y. K.; Hong, S.; Ryu, J. H.; Kim, T. S.; Park,

J. K.; Lee, H.; Choi, J. W. Mussel-Inspired Adhesive Binders for High-Performance Silicon Nanoparticle Anodes in Lithium-Ion Batteries. *Adv. Mater.* **2013**, *25* (11), 1571–1576.

(89) Abraham, K. M. How Comparable Are Sodium-Ion Batteries to Lithium-Ion Counterparts? *ACS Energy Lett.* **2020**, *5* (11), 3544–3547.

(90) He, M.; Yuan, L. X.; Zhang, W. X.; Hu, X. L.; Huang, Y. H. Enhanced Cyclability for Sulfur Cathode Achieved by a Water-Soluble Binder. *J. Phys. Chem. C* **2011**, *115* (31), 15703–15709.

(91) Liu, B.; Zhang, J. G.; Xu, W. Advancing Lithium Metal Batteries. *Joule* **2018**, *2* (5), 833–845.

(92) Holoubek, J.; Liu, H.; Wu, Z.; Yin, Y.; Xing, X.; Cai, G.; Yu, S.; Zhou, H.; Pascal, T. A.; Chen, Z.; Liu, P. Tailoring Electrolyte Solvation for Li Metal Batteries Cycled at Ultra-Low Temperature. *Nat. Energy* **2021**, *6* (3), 303–313.

(93) Yu, Z.; Rudnicki, P. E.; Zhang, Z.; Huang, Z.; Celik, H.; Oyakhire, S. T.; Chen, Y.; Kong, X.; Kim, S. C.; Xiao, X.; Wang, H.; Zheng, Y.; Kamat, G. A.; Kim, M. S.; Bent, S. F.; Qin, J.; Cui, Y.; Bao, Z. Rational Solvent Molecule Tuning for High-Performance Lithium Metal Battery Electrolytes. *Nat. Energy* **2022**, *7* (JanuarY).

(94) Louli, A. J.; Eldesoky, A.; Weber, R.; Genovese, M.; Coon, M.; deGooyer, J.; Deng, Z.; White, R. T.; Lee, J.; Rodgers, T.; Petibon, R.; Hy, S.; Cheng, S. J. H.; Dahn, J. R. Diagnosing and Correcting Anode-Free Cell Failure via Electrolyte and Morphological Analysis. *Nat. Energy* **2020**, *5* (9), 693–702.

(95) Chen, X.; Zhao, B.; Yan, C.; Zhang, Q. Review on Li Deposition in Working Batteries : From Nucleation to Early Growth. **2021**, *2004128*, 1–23.

(96) Fang, C.; Li, J.; Zhang, M.; Zhang, Y.; Yang, F.; Lee, J. Z.; Lee, M. H.; Alvarado, J.; Schroeder, M. A.; Yang, Y.; Lu, B.; Williams, N.; Ceja, M.; Yang, L.; Cai, M.; Gu, J.; Xu, K.; Wang, X.; Meng, Y. S. Quantifying Inactive Lithium in Lithium Metal Batteries. *Nature* **2019**, *572* (7770), 511–515.

(97) Hobold, G. M.; Lopez, J.; Guo, R.; Minafra, N.; Banerjee, A.; Shirley Meng, Y.; Shao-Horn, Y.; Gallant, B. M. Moving beyond 99.9% Coulombic Efficiency for Lithium Anodes in Liquid Electrolytes. *Nat. Energy* **2021**, *6* (10), 951–960.

(98) Kim, M. S.; Zhang, Z.; Rudnicki, P. E.; Yu, Z.; Wang, J.; Wang, H.; Oyakhire, S. T.; Chen, Y.; Kim, S. C.; Zhang, W.; Boyle, D. T.; Kong, X.; Xu, R.; Huang, Z.; Huang, W.; Bent, S. F.; Wang, L.-W.; Qin, J.; Bao, Z.; Cui, Y. Suspension Electrolyte with Modified Li+ Solvation Environment for Lithium Metal Batteries. *Nat. Mater.* **2022**.

(99) Zhou, H.; Yu, S.; Liu, H.; Liu, P. Protective Coatings for Lithium Metal Anodes: Recent Progress and Future Perspectives. *J. Power Sources* **2020**, *450* (November 2019), 227632.

(100) Li, Q.; Zhu, S.; Lu, Y. 3D Porous Cu Current Collector/Li-Metal Composite Anode for

Stable Lithium-Metal Batteries. *Adv. Funct. Mater.* **2017**, *27* (18).

(101) Liu, H.; Yue, X.; Xing, X.; Yan, Q.; Huang, J.; Petrova, V.; Zhou, H.; Liu, P. A Scalable 3D Lithium Metal Anode. *Energy Storage Mater.* **2019**, *16* (September 2018), 505–511.

(102) Cui, S.; Zhai, P.; Yang, W.; Wei, Y.; Xiao, J.; Deng, L.; Gong, Y. Large-Scale Modification of Commercial Copper Foil with Lithiophilic Metal Layer for Li Metal Battery. *Small* **2020**, *16* (5), 1–9.

(103) Thirumalraj, B.; Hagos, T. T.; Huang, C. J.; Teshager, M. A.; Cheng, J. H.; Su, W. N.; Hwang, B. J. Nucleation and Growth Mechanism of Lithium Metal Electroplating. *J. Am. Chem. Soc.* **2019**, *141* (46), 18612–18623.

(104) Pei, A.; Zheng, G.; Shi, F.; Li, Y.; Cui, Y. Nanoscale Nucleation and Growth of Electrodeposited Lithium Metal. *Nano Lett.* **2017**, *17* (2), 1132–1139.

(105) Shi, F.; Pei, A.; Vailionis, A.; Xie, J.; Liu, B.; Zhao, J.; Gong, Y.; Cui, Y. Strong Texturing of Lithium Metal in Batteries. *Proc. Natl. Acad. Sci. U. S. A.* **2017**, *114* (46), 12138–12143.

(106) Li, Y.; Li, Y.; Pei, A.; Yan, K.; Sun, Y.; Wu, C. L.; Joubert, L. M.; Chin, R.; Koh, A. L.; Yu, Y.; Perrino, J.; Butz, B.; Chu, S.; Cui, Y. Atomic Structure of Sensitive Battery Materials and Interfaces Revealed by Cryo–Electron Microscopy. *Science (80-.).* **2017**, *358* (6362), 506–510.

(107) Zhao, Q.; Deng, Y.; Utomo, N. W.; Zheng, J.; Biswal, P.; Yin, J.; Archer, L. A. On the Crystallography and Reversibility of Lithium Electrodeposits at Ultrahigh Capacity. *Nat. Commun.* **2021**, *12* (1), 1–10.

(108) Huang, Z.; Zhou, G.; Lv, W.; Deng, Y.; Zhang, Y.; Zhang, C.; Kang, F.; Yang, Q. H. Seeding Lithium Seeds towards Uniform Lithium Deposition for Stable Lithium Metal Anodes. *Nano Energy* **2019**, *61* (February), 47–53.

(109) Liu, Y.; Lin, D.; Li, Y.; Chen, G.; Pei, A.; Nix, O.; Li, Y.; Cui, Y. Solubility-Mediated Sustained Release Enabling Nitrate Additive in Carbonate Electrolytes for Stable Lithium Metal Anode. *Nat. Commun.* **2018**, *9* (1), 1–10.

(110) Coaty, C.; Zhou, H.; Liu, H.; Liu, P. A Scalable Synthesis Pathway to Nanoporous Metal Structures. *ACS Nano* **2018**, *12* (1), 432–440.

(111) Zhang, X.-Q.; Chen, X.; Xu, R.; Cheng, X.-B.; Peng, H.-J.; Zhang, R.; Huang, J.-Q.; Zhang, Q. Columnar Lithium Metal Anodes. *Angew. Chemie* **2017**, *129* (45), 14395–14399.

(112) Qian, J.; Xu, W.; Bhattacharya, P.; Engelhard, M.; Henderson, W. A.; Zhang, Y.; Zhang, J. G. Dendrite-Free Li Deposition Using Trace-Amounts of Water as an Electrolyte Additive. *Nano Energy* **2015**, *15*, 135–144.

(113) Chen, S.; Zheng, J.; Yu, L.; Ren, X.; Engelhard, M. H.; Niu, C.; Lee, H.; Xu, W.; Xiao, J.; Liu, J.; Zhang, J. G. High-Efficiency Lithium Metal Batteries with Fire-Retardant

Electrolytes. *Joule* **2018**, *2* (8), 1548–1558.

(114) Ren, X.; Zou, L.; Cao, X.; Engelhard, M. H.; Liu, W.; Burton, S. D.; Lee, H.; Niu, C.; Matthews, B. E.; Zhu, Z.; Wang, C.; Arey, B. W.; Xiao, J.; Liu, J.; Zhang, J. G.; Xu, W. Enabling High-Voltage Lithium-Metal Batteries under Practical Conditions. *Joule* **2019**, *3* (7), 1662–1676.